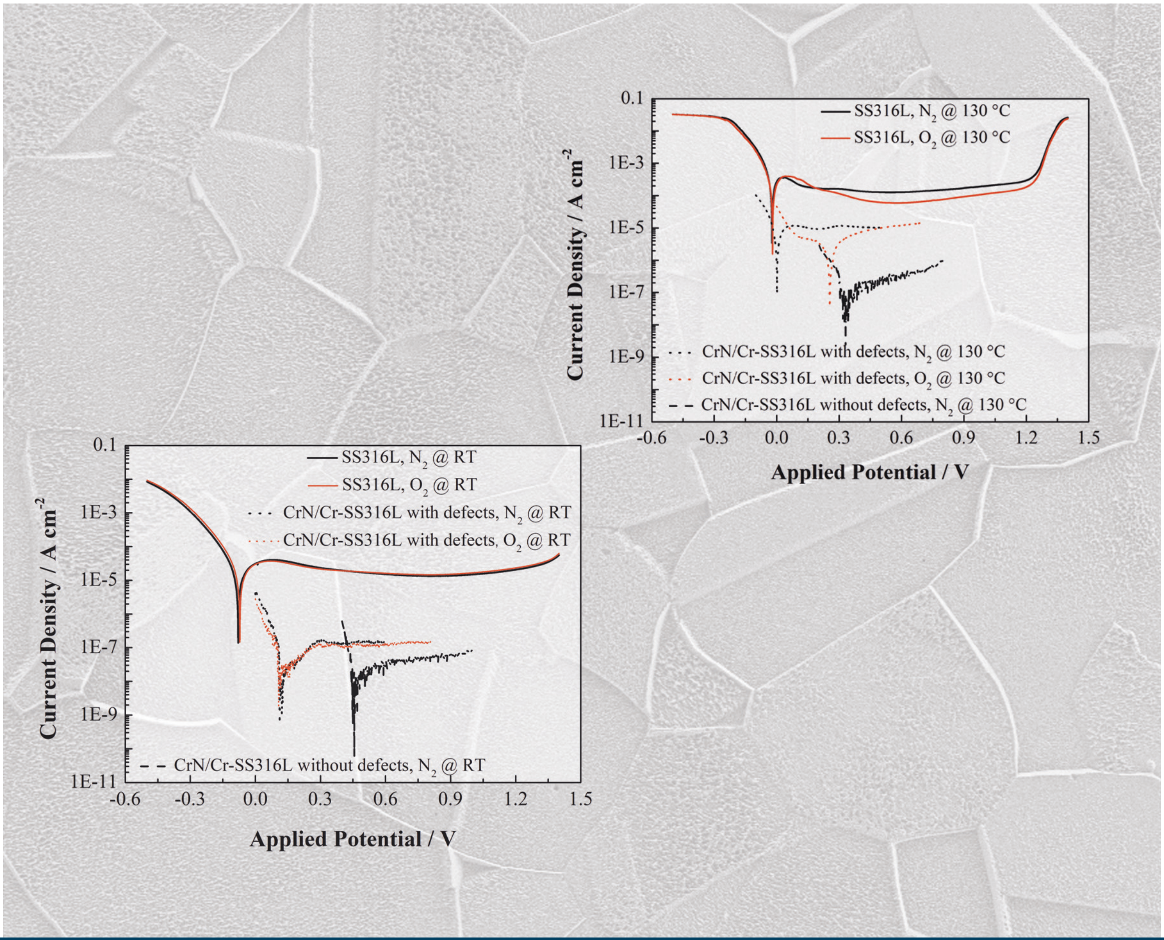

Coatings for Metallic Bipolar Plates in High-Temperature Polymer Electrolyte Fuel Cells

Ruiyu Li

Energie & Umwelt / Energy & Environment
Band / Volume 472
ISBN 978-3-95806-425-6

Mitglied der Helmholtz-Gemeinschaft

JÜLICH
Forschungszentrum

Schriften des Forschungszentrums Jülich
Reihe Energie & Umwelt / Energy & Environment Band / Volume 472

Forschungszentrum Jülich GmbH
Institut für Energie- und Klimaforschung
Elektrochemische Verfahrenstechnik (IEK-3)

Coatings for Metallic Bipolar Plates in High-Temperature Polymer Electrolyte Fuel Cells

Ruiyu Li

Schriften des Forschungszentrums Jülich
Reihe Energie & Umwelt / Energy & Environment Band / Volume 472

ISSN 1866-1793 ISBN 978-3-95806-425-6

Bibliografische Information der Deutschen Nationalbibliothek.
Die Deutsche Nationalbibliothek verzeichnet diese Publikation in der
Deutschen Nationalbibliografie; detaillierte Bibliografische Daten
sind im Internet über http://dnb.d-nb.de abrufbar.

Herausgeber und Vertrieb:
Forschungszentrum Jülich GmbH
Zentralbibliothek, Verlag
52425 Jülich
Tel.: +49 2461 61-5368
Fax: +49 2461 61-6103
zb-publikation@fz-juelich.de
www.fz-juelich.de/zb

Umschlaggestaltung: Grafische Medien, Forschungszentrum Jülich GmbH

Druck: Grafische Medien, Forschungszentrum Jülich GmbH

Schriften des Forschungszentrums Jülich
Reihe Energie & Umwelt / Energy & Environment, Band / Volume 472

D 82 (Diss. RWTH Aachen University, 2019)

ISSN 1866-1793
ISBN 978-3-95806-425-6

Abstract

At present, High-temperature polymer electrolyte fuel cells (HT-PEFCs) are usually constructed using graphite bipolar plates (BPPs). Although continuous efforts have been made to increase their properties and reduce their volume, weight, and cost, graphite BPPs are still far from the requirements of the U.S. Department of Energy (DOE). However, metallic BPPs produced from thin metal foils are promising candidates for reaching DOE targets. The high temperature (ca. 120 °C-180 °C) and the use of phosphoric acid as electrolyte within the HT-PEFC provide a significantly aggressive environment for the components of HT-PEFC, and especially in metallic BPPs.

In this thesis, stainless steel 316L (SS316L) is chosen as the substrate for the metallic BPPs, due to its reasonable degree of corrosion resistance and low cost. The corrosion properties of SS316L and the influence of gases on the corrosion behavior of SS316L in the simulated HT-PEFC environment were thoroughly examined.

It is extremely difficult for bare metallic materials to reach the acceptable level of corrosion rates of HT-PEFC. Therefore, a protective coating is mandatory for the application of metallic BPPs in HT-PEFC. Based on the initial results by which a type of Cr-rich layer formed in the simulated cathodic environment of HT-PEFC was found able to tolerate the aggressive environment of hot phosphoric acid under an O_2 purged atmosphere, a bilayer CrN/Cr coating was chosen as the coating research object for this work. This work investigated the corrosion behavior of bilayer CrN/Cr-coated SS316L BPPs in the simulated environment of HT-PEFC, and its self-healing ability when artificially induced defects appeared on its surface. Finally, the performances and durability of the CrN/Cr-coated SS316L BPPs were validated in a real HT-PEFC.

A series of experiments revealed that CrN/Cr-coated SS316L demonstrates superior performance in the HT-PEFC environment, even including a degree of self-healing ability when defects appeared on its surface in an O_2 purged atmosphere. Therefore, this work has demonstrated that bilayer CrN/Cr-coated SS316L is a promising candidate as a low-cost metallic BPP in HT-PEFCs.

Kurzfassung

Derzeit werden üblicherweise Graphit-Komposit Bipolarplatten für Hochtemperatur-Polymerelektrolyt-Brennstoffzellen (HT-PEFCs) verwendet. Trotz kontinuierlicher Forschung um sowohl Gewicht, Volumen als auch Kosten der Platten zu verringern, sind die Eigenschaften der graphitischen Bipolarplatten noch weit von den Zielvorgaben des US-amerikanischen Energieministeriums (DOE) entfernt. Alternative metallische Bipolarplatten aus dünnen Metallfolien sind vielversprechende Kandidaten, um die DOE-Ziele zu erreichen. Die hohe Betriebstemperatur (ca. 120°C - 180°C) der HT-PEFC und die Verwendung von Phosphorsäure als Elektrolyt resultieren jedoch in einer aggressive Umgebung für die Zell- und Stackkomponenten und hierbei insbesondere für die metallischen Bipolarplatten.

In der hier vorgestellten Arbeit wird Edelstahl 316L (SS316L) als Substrat für die metallischen Bipolarplatten verwendet, da es einen angemessenen Grad an Korrosionsbeständigkeit aufweist und kostengünstig ist. Die Korrosionseigenschaften von SS316L und der Einfluss von Gasen auf das Korrosionsverhalten von SS316L in einer simulierten HT-PEFC-Umgebung wurden eingehend untersucht.

Es zeigte sich, dass mit blanken metallischen Materialien keine akzeptablen Korrosionsraten zu erzielen sind. Daher ist bei der Anwendung von metallischen Bipolarplatten in HT-PEFC eine Schutzschicht zwingend erforderlich.

Die sich unter simulierten kathodischen HT-PEFC Bedingungen gebildete Chrom angereicherte Schicht zeigte sich tolerant gegenüber der aggressiven Umgebung in dem gewählten Betriebsfenster. Basierend auf diesen Ergebnissen wurde eine zweilagige CrN/Cr Beschichtung für die weiteren Arbeiten gewählt.

Das Korrosionsverhalten und die Selbstheilungsfähigkeit von Oberflächendefekten von CrN/Cr beschichteten SS316L Bipolarplatten unter simulierten HT-PEFC Bedingungen war ein Schwerpunkt der Arbeit. Darüber hinaus wurden CrN/Cr-beschichteten SS316L-Bipolarplatten in realen Zellen getestet und die Halbzellenmessungen validiert.

Die Experimente zeigten, dass CrN/Cr-beschichtetes SS316L in der HT-PEFC-Umgebung nicht nur eine hohe Korrosionsbeständigkeit aufweist, sondern auch eine partielle Selbstheilungsfähigkeit bei kathodischen HT-PEFC-Bedingungen. Es stellte sich heraus, dass eine zweilagig, mit CrN/Cr beschichtete SS316L als kostengünstige metallische Bipolarplatte für HT-PEFCs geeignet ist.

Contents

Chapter 1 Introduction and Goals of the Work

Due to environmental issues, there has been increased interest in finding alternative energy sources and the utilization methods with higher efficiency and greater environmentally sustainability [1]. Hydrogen is regarded as an ideal energy source, as it provides some crucial advantages, including free carbon emission; easy accessibility and renewable, high fuel efficiency [2-6]. The normal utilization method for hydrogen is in fuel cells. A fuel cell is an electrochemical device that can efficiently convert the chemical energy of fuels, including hydrogen, directly into electricity, without the limitations of the Carnot cycle. Fuel cell technology makes the hydrogen economy possible, which in turn can increase fuel efficiency, and decrease dependency on traditional fossil fuels. This combination of fuel cells and hydrogen is expected to have a positive effect on global climatic change [6, 7].

In terms of types of electrolyte and operating conditions, fuel cells are mainly divided into five categories: polymer electrolyte membrane fuel cells (PEFC), phosphoric acid fuel cells (PAFC), molten carbonate fuel cells (MCFC), solid-oxide fuel cells (SOFC), and alkaline fuel cells (AFC).

Among them, a typical PEFC normally operates at a temperature of less than 80 °C with perfluorosulfonic acid (Nafion) as its electrolyte membrane [8]. The PEFC has received much interest regarding its many application areas, and especially in the area of mobile power supply, due to its providing the possibility for fast start-ups and dynamic operations [7, 9]. Beginning in 2015, most of the major car manufacturers began introducing into the market commercial fuel cell cars which are using PEFC as major energy supplier; this, in turn, has ignited interest in the PEFC concept. Thus, due to their enthusiasm concern fuel cell cars, the world's major nations have begun to encourage the PEFC industry.

As mentioned previously, the low temperature (less than 100 °C) of a normal PEFC allows for rapid energization and easier operations, although the low initiation temperature and the necessity for hydrated hydration have introduced the problem of two-phase flow which necessitates a complex of fuel cell system and a special control strategy [10-14]. Conversely, the low PEFC temperature increases the sensitivity of catalysts within the fuel cells to the impurities associated with hydrogen, such as carbon monoxide (CO). Even a small number of CO molecules in ppm can poison the platinum (Pt) catalyst within the LT-PEFC by blocking its active sites [15, 16]. At present, hydrogen is still mainly produced by steam reformed from natural gas or other fossil fuels, such as propane, gasoline, diesel, methanol, or ethanol [17-19]. Steaming reforming of fossil fuels produces low purity hydrogen with a high concentration of carbonaceous species, such as CO [19]. Therefore, the use of hydrogen derived from steam reforming requires additional steps to dramatically reduce the CO content to an acceptable level which in turn will cause a large amount of additional energy usage, bolstering the complexity of the system.

As an alternative technology, the high-temperature polymer electrolyte membrane fuel cell (HT-PEFC) comes into play, operating within a range of 120-180 ºC and currently employing phosphoric acid-doped polybenzimidazole (PBI) membranes as its electrolyte. HT-PEFC technology combines both the benefits of both normal PEFC and classical PAFC but leaves their deficiencies intact [20]. HT-PEFC exhibits several more advantages, as follows, than a normal PEFC:

- Due to its higher operation temperature, its CO tolerance is raised by as much as 3%-5% in the HT-PEFC as opposed to ppm level in normal PEFCs [21], which make it possible to use low-cost hydrogen generated from steam reforming.
- The absence of both liquid water in its stack and the requirement for a humidifier for its operation, which in turn negates the need for a water management system, increments the system's simplicity [22].
- Easier heat management and the employment of produced heat.

As one of the key components in an HT-PEFC, bipolar plates (BPPs) account for a large fraction of the total weight, volume and cost of the stack [23]. The employment in the HT-PEFC of a phosphoric acid-doped PBI membrane and its high temperature introduce an extremely harsh environment for its components. Therefore, at present, BPPs are made from graphitic composite materials; the use of metallic BPPs has only recently been discussed [8, 24, 25]. Metals are regarded as good candidates for BPPs since they can provide some crucial advantages, including increased ductility, high electronic conductivity and the possibility for low-cost mass production through stamping or hydroforming [25]. The integration of metallic BPPs is also the key to enhancing the volumetric and gravimetric power density of fuel cells due to the more compact design they enable [8, 23].

Even though there are significant research focuses on metallic BPPs in normal PEFCs [23, 26, 27], research on the application of metallic BPPs to HT-PEFCs is limited. At present, the fundamental understanding on metallic BPPs corrosion and suitable coating materials in the harsh environment of the HT-PEFC remains unclear, and these inadequacies have become the greatest obstacle in the application of metallic BPPs to HT-PEFCs [8, 28, 29]. Therefore, the present work focuses on the fundamental research concerning the electrochemical corrosion of bare metallic materials and suitable coating materials in simulated HT-PEFC environments and finally validates their performance in a real HT-PEFC.

1.1 The electrochemical corrosion of metallic materials in the simulated HT-PEFC environment

Due to the demand for the miniaturization of energy devices, increasing attention has been paid to the use of metal in preference to graphite as the candidate material of BPPs in PEFCs, including HT-PEFCs. An understanding of the corrosion of metallic materials within the HT-PEFC environment is vital for the creation of further corrosion control strategies and might narrow the search for suitable coatings. Within an HT-PEFC, four main factors influence corrosion: electrolytes (concentrated phosphoric acid), temperature (in the range of 120 ºC – 180 ºC), gas (hydrogen in the anode; oxygen or air in the cathode), and the potential of the working conditions (ca. 0.65 V at the cathode; ca. 0.05 V at the anode). Our previous colleague, Vitali Weissbecker, has investigated different metallic materials internal to a simulated HT-PEFC environment, but only one subject to nitrogen purging [30]. Since the introduced gases will influence to some extent the composition and structure of the passive films formed on the surface of metallic materials, it would be interesting to investigate the influence of gases on the corrosion behavior of metallic materials in the simulated HT-PEFC environment. Moreover, an analysis of the passive layer's composition will help to find suitable coatings since the passive layers can tolerate the harsh internal environments of simulated HT-PEFCs.

1.2 An electrochemical corrosion study of suitable coatings in the simulated HT-PEFC environment

Due to the unacceptably high corrosion current densities caused by the harsh corrosion environment within the HT-PEFCs and the intense passive layer formed (which is responsible for the high interfacial contact resistance (ICR) between BPPs and the gas diffusion layer (GDL), the directly application of metallic BPPs in HT-PEFCs appears impossible to date [8, 25, 31, 32]. To overcome the problem concerning the corrosion of bare metallic BPPs and further decreases in the contact resistance between metallic BPPs and the GDL, but still retain the benefits of employing metals, one possible solution could be that of applying conducting and inert coatings to the metallic BPPs [29]. From the research on bare metallic materials within simulated HT-PEFC environments, a passive, Cr-rich, layer formed in simulation's cathodic environments was able to tolerate the harsh environment of hot phosphoric acid under an oxygen purged atmosphere [8]. Based on this, the bilayer CrN/Cr coating fabricated by a magnetron sputtering method with an inner Cr layer and an outmost CrN layer was expected to display good performance in the environment of an HT-PEFC and was subsequently evaluated in a simulated HT-PEFC environment.

1.3 The electrochemical corrosion behavior of suitable coatings with artificially created defects in simulated HT-PEFC environments

The coatings prepared by PVD inevitably reveal inherent defects, particularly on the level of large-scale productions, which include micropores and pinholes [33, 34]. Also, for transport applications, the vibration environment further induces cracks in the coatings. For coating without self-healing ability, the electrolyte passes through the damaged sites, directly contacting the substrate, resulting in localized corrosion. The application of a metal component can induce a self-healing ability to films: The oxidation of the metallic component will heal flaws in the films [35]. The inner soft Cr layer in the bilayer CrN/Cr coating mainly has two functions: one is to improve adhesion between the CrN layer and the substrate, and the other proposed for the metallic components in the coating displayed a self-healing effect when defects appeared on the surface of the coating. Therefore, this portion of the project investigates the artificially created defects of CrN/Cr coatings on corrosion behaviors in simulated HT-PEFC environments and verifies the coating’s self-healing ability in response to defect appearance on the coating surface. Since oxygen will help to form a type of Cr-rich layer of high stability in hot phosphoric acid, it is also important to investigate the effects of oxygen on the corrosion of CrN/Cr coatings with artificially induced defects.

1.4 The Performance and durability of HT-PEFC employing different types of bipolar plates

Based on our previous results [29], the bilayer CrN/Cr coating demonstrates excellent performance in the HT-PEFC environment. Since the real HT-PEFC environment is not identical to that of the simulated HT-PEFC environment, it is necessary to investigate in situ investigate the performance and durability of CrN/Cr coated metallic BPPs in real HT-PEFC conditions as compared with graphite and bare metallic BPPs.

1.5 Outline

- Chapter 2 presents the corrosion theory and the commencement of the metallic BPP research

- Chapter 3 provides detailed information on experimental operations and specimens
- Chapter 4 describe the corrosion and electrical properties of SS316L stainless steel in a simulated HT-PEFC environment
- Chapter 5 presents an electrochemical corrosion study on bilayer CrN/Cr coating in a simulated HT-PEFC environment
- Chapter 6 investigates the effects of oxygen on the corrosion behavior of CrN/Cr coating with artificially created defects in a simulated cathodic environment of HT-PEFC
- Chapter 7 reports the performance and durability of HT-PEFCs employing different BPPs
- Chapter 8 gives a comprehensive discussion of all the results
- Chapter 9 is the conclusion

Chapter 2 Theory and Literature Overview

By using metallic BPPs rather than graphite BPPs, the volumetric and gravimetric power density of HT-PEFC will be dramatically enhanced by more than 50% [30]. At present, the main obstacle for the use of metallic BPPs in HT-PEFCs is the potential for the corrosion of metallic materials in the harsh environment of the HT-PEFC. Therefore, the present work mainly focuses on two areas: one is the corrosion phenomena and mechanism of the metallic BPPs in both simulated and real HT-PEFC environments; the other is the research on coating materials, particularly when applied to HT-PEFCs. Section 2.1 describes the functional principles and the theoretical background of the HT-PEFC. Furthermore, Section 2.1 considers the cost/volume/weight distributions of the individual cell components. In Section 2.2, the corrosion processes and mechanisms at the metal/electrolyte interface are described, including thermodynamics and kinetics. The influence and mechanisms of metallic BPP corrosion on the performance of the fuel cells is described in Section 2.3. In Section 2.4, an overview of the literature on the corrosion of bare metallic and coating materials in the HT-PEFC environment and with phosphoric acid is presented. Chapter 2 closes with a summary in Section 2.5.

2.1 A general overview of the HT-PEFC

A fuel cell is an electrochemical cell that can directly convert a fuel's chemical energy into electricity through an electrochemical reaction rather than via combustion: the hydrogen fuel undergoes a redox reaction with oxygen or another oxidizing agent [36]. HT-PEFCs operate in the range of 120 °C-180 °C and currently employ phosphoric-acid-doped polybenzimidazole membranes as their electrolytes [37]. The basic structure of an HT-PEFC is presented in Figure 2.1. As shown in Figure 2.1, an HT-PEFC is mainly constructed from inside to outside from a phosphoric-acid-doped membrane, catalyst layers (CLs), GDLs and BPPs. The basic reactions in the HT-PEFC while it operates are a hydrogen oxidation reaction (HOR) (Equation 2-1) at the anode side, and an oxygen reduction reaction (ORR) (Equation 2-2) at the cathode side. The overall reaction is outlined in Equation 2-3.

$$H_2 \leftrightarrow 2H^+ + 2e^- \qquad \text{2-1}$$

$$\frac{1}{2}O_2 + 2H^+ + 2e^- \leftrightarrow H_2O(g) \qquad \text{2-2}$$

$$H_2 + \frac{1}{2}O_2 \leftrightarrow H_2O(g) \qquad 2\text{-}3$$

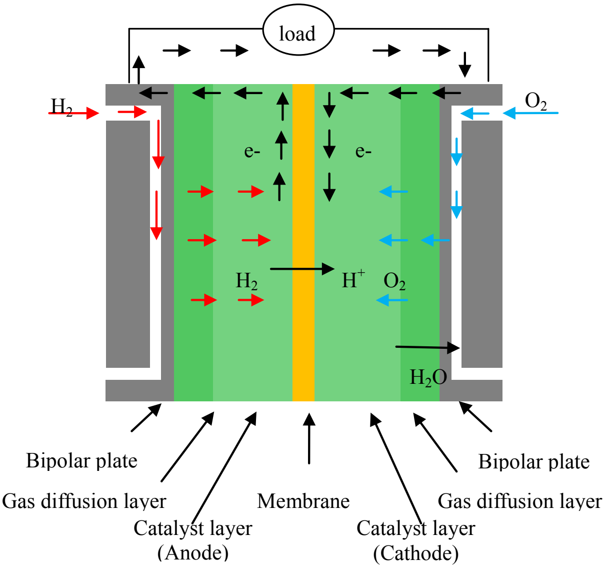

Figure 2.1. *A diagram of an HT-PEFC.*

(1) A Phosphoric acid doped membrane

The functions of the membrane offer a transportation pathway from the anode to the cathode and prevent the gases from passing through the MEA. In the form of membranes or films, PBI has been explored for liquid and gas separation applications at high temperatures and in harsh environments due to its durability and relatively low cost [38-42]. In the complex system of phosphoric acid, the protons can be easily transferred between protons and different phosphorous acid species by the dynamic breakage and formation of the hydrogen bonds [43]. Other important features of phosphoric or phosphonic acids are their excellent thermal stability and low vapor pressure at elevated temperatures. Phosphoric acid doped PBI membranes have been successfully developed and systematically characterized with good performance (proton conductivity, mechanical strength, thermal stability, and other features) for HT-PEFCs [44-49]. The polymerization process of PBI is shown in Figure 2.2.

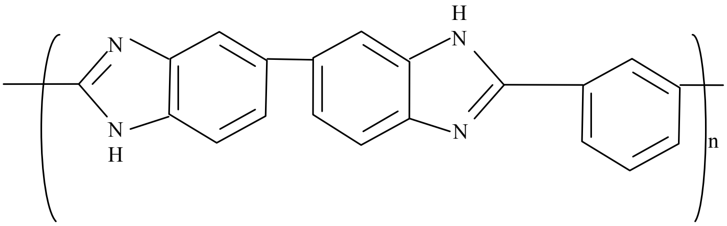

Figure 2.2. Chemical structure of poly(2,2'-m-(phenylene)-5,5'-bibenzimidazole.

(2) CL

The catalyst is a crucial component of all fuel cell types since, without catalysts, both the anode and cathode reaction would not proceed at sufficiently high rates [50]. Catalysts in HT-PEFCs usually consist of high surface area carbon supported Pt nanoparticles which are combined with a high-temperature stable polymer binder such as PTFE to form the CL within a membrane electrode assembly (MEA). Unlike in LT-PEFCs, where a proton exchange ionomer is used as a binder, the binder in HT-PEFCs does not provide a proton conducting pathway between the catalyst and membrane. Phosphoric acid within the CL, therefore, enables proton transport to and from the catalyst [50].

(3) GDL [51]

The GDL is porous and normally composed of carbon fibers. The main function of the GDL is homogeneous substance transport between the BPPs and CL, including for reactant gases, water production and electrons.

(4) BPP

The main functions of BPPs in the HT-PEFC stack are conducting electrical currents and heat, distributing coolants within the cooling flow field, separating the gases of adjacent cells and supplying and homogeneously distributing reactant gases within the flow field, transporting the water produced out of the cell in the flow field and provide mechanical stability for the stack [52, 53]. The MEA is always considered the dominating part of the stack regarding cost and performance; however, the BPPs have been underestimated regarding both their technical requirements and their contribution to the cost [51]. Also, the sizes and dimensions, weight, thermal and electrical properties of the stack are to a great extent determined by BPP technology [50]. In general, there are mainly two different types of BPPs technologies: one depends on graphite, and the other on metal. The former can be of pure graphite or a graphite composite material containing a polymer binder. The graphite-based materials have some advantages for the application of BPPs, such as their excellent electrical and thermal conductivity and good corrosion resistance. However, the graphite BPPs are quite thick (ca. 2 mm), while, the metal plates can be formed at a very low thickness (i.e., 0.1 mm) due to their excellent ductility without crack formation. The metals also offer excellent electrical and thermal conductivity. Additionally, the nonporous structure of the metal plates makes it possible to use ultrathin BPPs considering the strict requirement of their gas tightness. However, metal plates are prone to corrosion under the aggressive environment of the fuel cell, especially HT-PEFC which employs a phosphoric-acid-doped PBI membrane as its electrolyte. Until now, the corrosion problems of the metal plates in the HT-PEFC appear to remain unsolved. Therefore, graphite-based materials are the preferred ones to date [50]. Due to the advantages of metallic BPPs for miniaturization and low cost of the HT-PEFC stack, it would be of great technical and economic interest to solve the problem of corrosion in the metallic BPPs within HT-PEFCs, and this topic concerning their corrosion will be the focus of this thesis. Figure 2.3 displays the graphite and metallic BPPs from IEK-3.

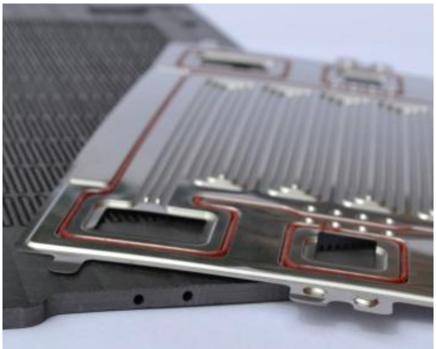

Figure 2.3. *A photograph of graphite and metal bipolar plates.*

2.2 Electrochemical corrosion

Corrosion is a common destructive phenomenon involving the deterioration of materials by electrochemical reactions between materials and substances in their environment. For example, due to the materials' natural tendency to convert to a more chemically-stable state, metals prefer to form into metal oxide, hydroxide, or sulfide. In fact, the corrosion process and its underlying thermodynamic and kinetic factors differ for different environments and materials [54]. The importance of corrosion research mainly arises in terms of two features: the economic and safety. From the economic aspect, there is greatly essential that material losses caused by corrosion to be reduced since this process results in the wasting of limited sources of materials, and particularly of metal resources, energy and water. Also, due to the deterioration of materials caused by corrosion during their use, the sudden failure of devices or equipment might result in serious safety issues. Therefore, the goals of a corrosion scientist are mainly two-fold: one focus is to predict the rate of corrosion with high accuracy; the other is to reduce corrosion rates to an acceptable level. The ultimate goal of this work is to reduce the corrosion rates of metallic BPPs in the HT-PEFC conditions to the acceptable range required by DOE [55]. The following gives the related fundamentals of thermodynamics and kinetics of corrosion.

2.2.1 The electrochemical reactions during corrosion

In a normal situation, corrosion occurs not by the direct chemical reactions between a material and its environment, but through a combination of coupled electrochemical half-cell reactions. Therefore, corrosion is an electrochemical process.

The corrosion of metals often involves coupled oxidative and reductive reactions, as shown in Equations 2-4 and 2-5, respectively. Taking the corrosion of zinc in acids as an example, as shown in Figure 2.4, the oxidation of the zinc atom is as follows:

$$Zn \rightarrow Zn^{2+} + 2e^- \qquad 2\text{-}4$$

The coupled reduction reaction is the hydrogen evolution reaction:

$$2H^+ + 2e^- \rightarrow H_2 \qquad 2\text{-}5$$

Therefore, the complete corrosion reaction for zinc in acid is:

$$Zn + 2H^+ \rightarrow Zn^{2+} + H_2 \qquad 2\text{-}6$$

The above case gives an example of a metal corroded in an acidic solution in the absence of dissolved oxygen. Conversely, in the case of neutral or basic solutions, the reduction reaction of the hydrogen evolution changes:

$$2H_2O + 2e^- \rightarrow H_2(g) + 2OH^- \qquad 2\text{-}7$$

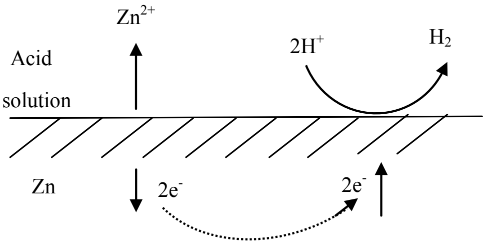

Figure 2.4. *Coupled electrochemical reactions in a normal zinc corrosion reaction within an acidic solution.*

When an aqueous solution contains dissolved oxygen, the oxygen reduction reaction (ORR) can exist as additional reduction reaction, Equation 2-8 is the dominant ORR in acidic solutions, and Equation 2-9 is the dominant one in neutral or basic solutions [54]:

$$O_2 + 4H^+ + 4e^- \rightarrow 2H_2O \qquad 2\text{-}8$$

$$O_2 + 2H_2O + 4e^- \rightarrow 4OH^- \qquad 2\text{-}9$$

2.2.2 The mixed potential theory

When an electrode is immersed in an aqueous environment, it will naturally acquire a potential, called the corrosion potential, which is shown as open circuit voltage (OCV). At OCV state, based on the principle of charge conservation, the overall current of the electrochemical system is zero. Therefore, the sum of the currents from the oxidation reactions must equal the sum of the currents from the reduction reactions at the corrosion potential of a freely immersed electrode, and the corrosion potential on a freely-immersed electrode is usually far from the reversible potentials for any of the reactions occurring on the surface [54].

$$\sum I_a + \sum I_c = 0 \qquad 2\text{-}10$$

The corrosion potential is a mixed potential of the anodic and cathodic reactions of the electrochemical system. The rate of the anodic and cathodic reactions determines the corrosion potential. Figure 2.5 gives a schematic Evans diagram which demonstrates the formation of the corrosion potential. Strictly speaking, each chemical reaction is a type of reversible reaction which contains anodic and cathodic branches. Therefore, there will be a reversible potential for each of the two partial reactions of the electrochemical system. In Figure 2.5, E^{rev}_{M/M^+} and E^{rev}_{H/H^+} represent the reversible potentials for the metal, M's, dissolution and hydrogen evolution reactions, respectively; $i_{o,M/M^+}$ and $i_{0,H/H^+}$ represents the exchange current densities for metal dissolution and hydrogen evolution, respectively, on M. Figure 2.5 shows that the anodic line for the metal dissolution intersects at one point the cathodic line for the hydrogen evolution. At this intersection point, the oxidation current densities equal the reduction current densities. Therefore, the potential of this intersection point is the corrosion potential. Even though the current densities of the anodic and cathodic reactions at the corrosion potential are equal, the current densities of the anodic reactions at the corrosion potential are normally regarded as the corrosion current densities.

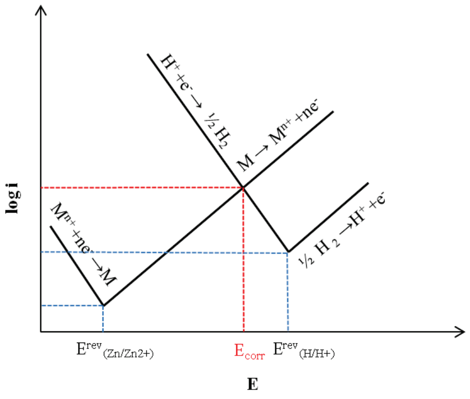

Figure 2.5. *A schematic Evans diagram for the corrosion of Metal M by an acid, showing the application of the mixed potential theory.*

2.2.3 Inhibition

Various methods exist to protect materials from corrosion. Among them, the corrosion inhibitor is one of the best and most useful ones in the industry [56]. Corrosion inhibitors are chemical substances that are added to the corrosive environment at a low concentration, but can effectively reduce the corrosion rate of the exposed subjects. There are mainly three types of inhibitors defined from their inhibition effect on the corrosion process: anodic, cathodic and a mixed inhibitor. Figure 2.6 provides schematic examples of the types of inhibition and their effects on the polarization curves. As mentioned, the role of corrosion of the anodic inhibitor is mainly to reduce the rate of the anodic portion of the corrosion reaction; this will also increase the corrosion potential of the subject. In contrast, the cathodic inhibitor mainly reduces the rate of the cathodic portion of corrosion and shows a decrease in the corrosion potential on the polarization curve. The mixed inhibitor concurrently reduces the rates of both the anodic and cathodic components, such that there is almost no change on the corrosion potential.

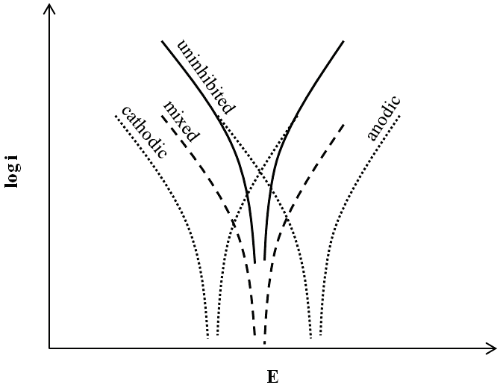

Figure 2.6. *A schematic representation of the effects of anodic, cathodic and mixed inhibition.*

2.2.4 Passivity

When a metal is in a passivity state, its corrosion rate will be dramatically reduced by orders compared with that under free conditions. The protective effects of passivity mainly arise from the thin oxide or oxyhydroxide layer formed on its surface that passivates the electrochemical reactivity of the metal [54].

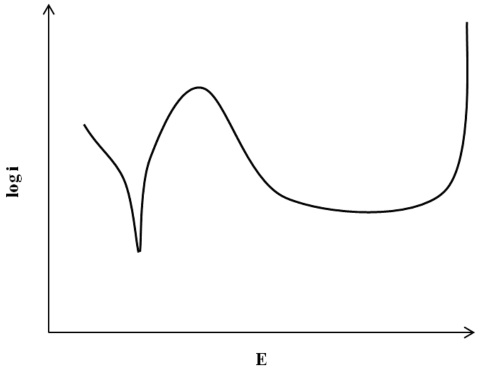

Figure 2.7. *A schematic polarization curve for passive samples.*

A schematic polarization curve for passive materials is shown in Figure 2.7. It represents the common polarization curve for a passive metal, which contains an active, passive and transpassive region with an obvious active-passive transition. In the active region, the corrosion current increases exponentially with the increase of the potential. When the potential reaches the point of active-passive transition, the current density trend reverses and can decrease by many orders of magnitude, with the current density in the passive regions often being relatively independent of the potential [54]. When the potential continues to increase, the passive film formed in the passive region may break down and high currents reappear, a process known as transpassivity.

2.2.5 Uniform vs. localized corrosion

As mentioned above, corrosion is a type of electrochemical reaction composed of coupled reduction reaction and oxidation reactions. The sites for the oxidation reactions are called anodes, and those for the reduction reactions are cathodes [54]. If the corrosion anodes and cathodes are fixed separately at one location, localized corrosion will occur. Alternatively, if the cathodes and anodes of corrosion move randomly across the sample's entire surface, this will result in uniform corrosion. Uniform corrosion and three forms of localized corrosion are illustrated schematically in Figure 2.8.

Uniform

Pitting Crevice Stress

Figure 2.8. *A schematic representation of uniform corrosion and three different forms of localized corrosion.*

2.3 The degradation of the bipolar plates

The BPP is a key component with multifunctions within the fuel cell stack, acting as a separator between the fuels, oxidant gases, and coolant; homogeneously distributing the reactant and product streams and collecting the current generated by the electrochemical reaction [57-59]. In order to fulfill its multiple functions, suitable materials should contain a series of properties, e.g., high corrosion resistance and electrical conductivity, low gas permeability and thermal resistance and low costs for mass production. Therefore, it is extremely difficult to find well fitting materials for the BPPs in a fuel cell. At presently, the most commonly used material for BPPs is graphite or graphite composites. Graphite based materials can offer almost all the properties needed for BPPs, but there are two main drawbacks: one is the relatively high gas permeability of graphite-based materials which results in their high thickness, while the other is that the manufacturing cost for graphite-based BPPs is still too great for mass production. As an alternative candidate, metallic BPPs can avoid the drawbacks of graphite-based materials, while metallic materials have a serious corrosion problem in the aggressive environment of the fuel cell. Therefore, metallic materials covered with conductive but inert coatings are regarded as the promising candidates as the ultimate material selected for BPPs.

2.3.1 The degradation mechanism in metallic bipolar plates and its influence on the fuel cells

The literature references referring to the metallic BPPs' degradation mechanisms and their influence on the performance of normal PEFC by using various in situ and ex situ methods are widely shared [58, 60-66]. There are mainly two reasons for the degradation of normal PEFCs constructed with metallic BPPs: one is the increase in the contact resistance between the BPP and GDL, attributed to the non-conductive passive layer formed on the surface of metallic materials; another is that the metal ions leaching from the metallic BPPs have a seriously poisoning effect on the membrane and catalyst.

In the case of HT-PEFCs, activities addressing the effects of the corrosion of metallic BPPs on the degradation mechanisms of HT-PEFCs are very limited. Hartnig *et al.* reported how BPP degradation affects the performance of HT-PEFCs [67]. They propose that the main reason for the different degradation rates of HT-PEFCs with unlike types of BPPs mainly arises from the diverse adsorption abilities of BPPs on phosphoric acid. They conclude that their single cell with gold-coated metallic BPPs and surface sealed graphite BPPs showed lower degradation rates, which attributed to the lesser degree of phosphoric acid loss from the MEA as compared with the reference measurements for normal graphite BPPs. Alnegren *et al.* have successfully demonstrated the use of bare metallic BPPs in HT-PEFCs and observed a voltage drop of 17 mV at a current density of 200 mA cm^{-2} following 900 h of cell operation, which indicates promise for the application of metallic BPPs in HT-PEFCs [24]. Janßen *et al.* have developed and demonstrated the feasibility of a long-term run (4700 h) HT-PEFC stack with gold-coated metallic BPPs [68]. Chen *et al*. have developed an HT-PEFC with stamped 304 stainless steel BPPs that could approach the performance of HT-PEFCs with graphite BPPs [69]. Alegre *et al*. have assessed the durability of low-cost Al BPPs for HT-PEFCs, and discovered that their Al-based plates provide better initial performance in comparison to the cells with graphite plates [70]. All of these publications demonstrate the possibilities of metallic BPPs in the application of HT-PEFCs, but they fail to demonstrate the specific effects of the corrosion of metallic BPPs on the degradation mechanisms of HT-PEFCs. Due to a different type of electrolyte and the higher temperatures used in HT-PEFCs as compared with normal PEFCs, the effects of the corrosion of metallic BPPs on the degradation mechanism in HT-PEFCs, and the poisonous effect of metal ions on the catalyst and membrane in HT-PEFCs, might vary from occurrences with normal LT-PEFCs. Additionally, in contrast to normal PEFCs, HT-PEFCs using concentrated phosphoric acid as the ionic liquid for proton conductivity, influence of metal ions on the proton conductivity of concentrated phosphoric acid at high temperatures remains unclear. It would be of great interest and importance to clarify these questions before the large-scale application of metallic BPPs in HT-PEFCs.

2.3.2 The materials composing bipolar plates

Research on the materials composing BPPs in the application of normal PEFCs utilizing various in situ and ex situ methods is widely shared [36, 68, 71-74]. Graphite is the conventional material used in the BPPs in normal PEFCs, due to its several excellent properties including high corrosion resistance, and high electrical conductivity. However, the high gas permeability and the poor vibration resistance of graphite materials make it unsuitable for mobile applications whereby a more compact fuel cell system with high vibration resistance is needed. As well, graphite BPPs are manufactured by machine, which is very time consuming and expensive, making it unsuitable for mass production. Graphite-based composites are also employed to improve the drawbacks of pure graphite, which include high gas permeability, poor vibration resistance and the high cost of manufacturing [75-78]. Additional, graphite-based composites make it possible to produce BPPs at relatively low cost using a compression molding method [79, 80]. Still, the cost for the BPPs fabricated by graphite composites is still greater than the DOE requirements and their volume and weight are still too expensive for mobile applications. Metals are regarded as a promising candidate for BPP materials in fuel cells considering their easier manufacturability and lower weight and volume as compared with graphite-based BPPs [81, 82]. Noble metals (i.e., Au, Pt, Nb, Ta) provide excellent corrosion resistance in the environment of the fuel cell, and are available for thin plate manufacturing due to their good ductility [83, 84]. But the extremely high costs of these raw materials make it impossible for them to be employed as base materials for BPPs. The commercially available and lightweight metallic materials and their alloys, such as Al and Ti have received considerable attention due to their decreased mass, good electrical conductivity and excellent mechanical properties [85-89], and the costs of Ti or Al is still too great for the requirements of DOE. Stainless steels are considered the most promising metal materials for the application of BPPs due to their wide range of alloy choices, reasonable corrosion resistance in an aggressive environment and low cost [81, 90, 91]. The common problem of bare metallic materials in a fuel cell is their susceptibility to corrosion. As mentioned in Section 2.3.1, the corrosion of bare metallic materials influences the performance of fuel cells in mainly two ways: one is the increase in contact resistance between the BPP and the GDL due to the formation of nonconductive passive layer on the surfaces of metals; while the other is that metal ions' potential for leaching from bare metals, which can poison the membrane and catalysts. As a result, it is less possible to directly apply for the bare metallic BPPs in PEFCs, especially HT-PEFCs which have harsher environments than normal ones. Weissbecker *et al.* tested the suitability of different stainless steels and alloys in the application of HT-PEFCs, and concluded that all metallic materials they tested revealed extremely high corrosion rates in hot phosphoric acid, such that bare commercial metallic BPPs would not be possible for the long-term application of HT-PEFCs [25, 28]. In order to minimize the corrosion problem and contact resistance but retain the benefits of metals, one possible solution would be that of utilizing conducting and inert coatings to protect bare metallic BPPs from corrosion in the aggressive environment of the fuel cell.

2.3.3 Coatings for metallic bipolar plates

The metallic materials, especially stainless steels, are promising candidates for BPPs in PEFCs. The main problem which prohibits their application in this way, including in HT-PEFCs, is their susceptibility to corrosion in the aggressive environment of the PEFC. The coatings on the surface of metallic BPPs are used to improve corrosion resistance and further decrease contact resistance. Therefore, the selection of coating materials for metallic BPPs should follow several guidelines, including good electrical conductivity but inertness in an acid environment, good substrate adhesion ability and a similar thermal expansion coefficient, easier deposition and low cost. Literature references referring to a coating for a normal PEFC, which operate at a temperature of about 80 ºC with Nafion as the proton-conductive membrane and normally use a low concentration of sulfuric acid as their simulated environment, are widely shared [23, 92-97].

There are two major types of coatings in the application of normal PEFC, namely, carbon-based and metal-based coatings. The carbon-based coatings mainly include different types of carbon (graphene, graphite and carbon nanotube) coatings and conductive organic coatings and their composites [98-101]. Alternately, the metal-based coatings are mainly composed of noble metals and conductive metallic ceramics (i.e., metal nitrides and metal carbides) [27, 84, 102, 103]. Unlike the conventional metallic ceramics, which are brittle, MAX phases, a series of unique new carbides and nitrides combine the high corrosion resistance of conventional conductive metallic ceramics with the excellent extensibility of metallic materials [104-106]. The excellent extensibility of the MAX phases results in high-quality vibrational resistance in mobility applications. Therefore, the MAX phases are a promising candidate for the coating of metallic BPPs for mobility applications, such as in cars and planes.

However, in the case of HT-PEFCs, activities addressing the coating of metallic BPPs are relatively limited. Weissbecker *et al.* reported boron-doped diamond coatings on niobium as being suitable for use as BPPs in fuel cell applications [107]. The boron-doped diamond coating used in this research was fabricated at around 2000 ºC, and the use of thick niobium substrates was found unsuitable for the real world application of metallic BPPs in fuel cells, regardless of the economic and technical factors. Kouril *et al.* published the low corrosion rates of tantalum coatings in phosphoric acid at 150 ºC, but it has been concluded that tantalum's behavior under even minor cathodic polarizations deems it unsuitable for fuel cell applications, as this induces the evolution of hydrogen and the formation of hydrides, which in turn leads to the material's embrittlement [32]. The free corrosion potential of tantalum reported in this research is ~0.6 V against a saturated Ag/AgCl electrode (SSCE) in phosphoric acid at 150 ºC, which means it would be ~0.822 V against a normal hydrogen electrode (NHE). This indicates that the tantalum is unsuitable for the applications in HT-PEFCs, as the potentials for both the anodic and cathodic sides of the HT-PEFC are lower than 0.8 V against NHE under most working conditions [108]. Wang *et al.* have shown the superior corrosion resistance of multilayer TaN/Ta coating with six layers of intersecting tantalum and tantalum nitride at 85 wt.% H_3PO_4, fabricated by the magnetron sputtering method [33]. The use of Ta as the intersecting and adhesive layer carries the risk of a sudden breakdown when cracks appear on the outer TaN layer, based on the publication by Kouril *et al.* The publication suggests that even a minor cathodic polarization will case the Ta layer to break in hot phosphoric acid. Also, the noble metal, Ta's, costliness also decreases its desirability. Ekberg *et al.* tested the MAX phase in the simulated environment of HT-PEFCs, and discovered that the MAX phase is intolerant to the aggressive environment of HT-PEFCs [109]. Currently, no coating type has been published which is suitable for the application of metallic BPPs in HT-PEFCs considering both the technical and economic factors. One of the goals of this work is to find a suitable coating alternative.

Chapter 3 The Experiment Methods

This chapter discusses the information on the specimen and experimental methods used in this study which focuses on the corrosion of bare and coated metallic BPPs of HT-PEFCs. Firstly, Section 3.1 shows the required devices and specimens used in the fundamental electrochemical study on the corrosion of metallic BPPs in the simulated HT-PEFC environment. Subsequently, Section 3.2 describes the devices and test rigs used for durability tests on single cells and also includes the test procedure. Finally, Section 3.3 describes the information on the devices and parameters of the material characterization methods employed in this study.

3.1 Electrochemical corrosion cells

In order to characterize the corrosion mechanism on bare and coated metallic materials of low cost and high accuracy within the HT-PEFC, a specially designed electrochemical corrosion cell which could simulate the HT-PEFC environment is needed. The requirements of the measurement cell mainly include the following three features:

- The materials used in this cell can be tolerated at temperatures greater than 100 ºC
- The defined surface area of the working electrode (WE)
- No inaccuracies of measurement due to exposed edges

Based on this requirement, a special three-electrode corrosion cell was designed at the IEK-3 (Forschungszentrum Juelich), as shown in Figure 3.1.

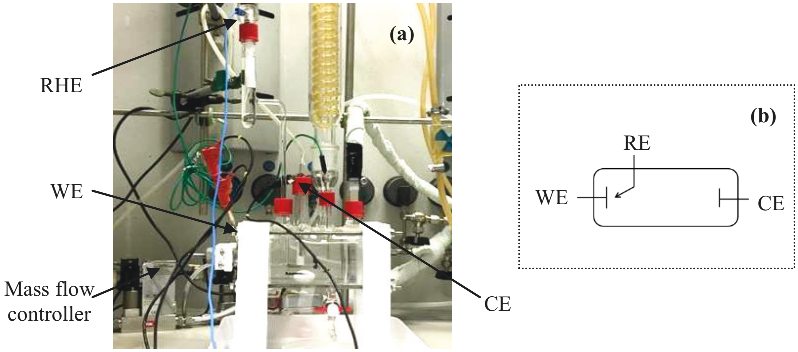

Figure 3.1. *The Setup of the specially designed three-electrode cell [29].*

3.1.1 Basic information on the corrosion cell

Detailed information on the corrosion cell was explained by our previous colleague, Vitali

Weissbecker (the first person to use this corrosion cell), in his publications [25, 28]. Briefly, the sample used as a working electrode (WE) is pressed with a circular stamp against the left exterior PTFE wall and sealed off by a Viton gasket. The PTFE wall is exchangeable, which results in different effective areas of the WE being exposed to the electrolyte based on different measurement purposes (see Figure 3.2). For most bare metallic samples and all coated samples, the exposed area of the tested sample is 2.54 cm^2 (see Figure 3.3(a)). When investigating with high accuracy the influence of the passive layer on the interfacial contact resistance between metallic BPPs and GDL and eliminate the influence of edge, a real metallic BPP with a flow channel was used. The exposed area of the PTFE wall for the real metallic BPPs with flow channels was 13.84 cm^2. As the reference electrode (RE), a reversible hydrogen electrode, RHE (HydroFlex, Gaskatel GmbH), was employed, while a platinum mesh served as the counter electrode (CE). In order to avoid a temperature-dependent potential shift in the RE during the high-temperature electrochemical measurements, the RHE was arranged outside of the cell at room temperature (RT), as shown in Figure 3.1. A Haber-Luggin capillary with a distance of 2 mm extends from the WE and is connected to the RE. The small distance between the Haber-Luggin capillary and WE will minimize the influence of distance on the potential of the WE measured. The tip of the Haber-Luggin capillary is filled with a porous frit in order to slow the leakage of electrolytes from the RE container while retaining ionic contact. Because the measurement temperature will be higher than 100 ºC, serious water evaporation is expected to occur, resulting in changes in the concentration of the electrolytes (85 wt. % H_3PO_4). In order to avoid a concentration change at high temperatures, a reflux condenser was installed, and a magnetic stirrer was used during all measurements.

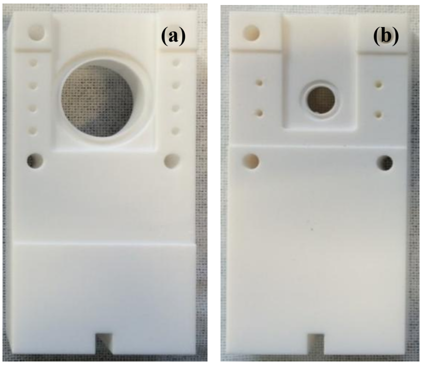

Figure 3.2. *Left exterior PTFE wall as a sample holder with a different effective area. (a) PTFE wall with an effective area of 13.84 cm^2. (b) PTFE wall with an effective area of 2.54 cm^2 [8].*

Since, in a normal situation, the electrolyte used for the doping treatment of the PBI membrane was 85 wt. % H_3PO_4, the 85 wt. % H_3PO_4 was selected as an electrolyte for all corrosion measurements in simulated HT-PEFC environments. For the separated RE, the 85 wt.% H_3PO_4 was also employed as the electrolyte to eliminate the influence in potential diffusion (E_{diff}) [25]. Phosphoric acid was purchased from VWR Chemicals (AnalaR NRMAPUR) and used without further purification. SS316L metal sheets with a thickness of 0.1 mm were provided by borit Leichtbau-Technik GmbH, and the thin metallic BPPs with flow fields were provided by Graebener Maschinentechnik GmbH. The main chemical composition of the SS316L specimens is shown in Table 3.1. The CrN/Cr coatings were deposited on the surface of a 0.1 mm thick SS316L substrate by a reactive magnetron sputtering method created by Teer Coating Ltd, and the main chemical composition of the CrN/Cr coating is detailed in Table 3.1.

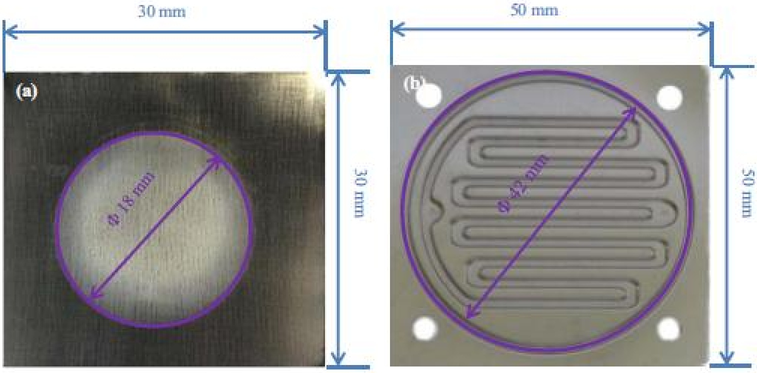

Figure 3.3. *Metallic specimens for electrochemical tests: (a) bare SS316L sheet with a thickness of 0.1 mm. (b) metallic bipolar plate with flow channel fabricated by SS316L, with a thickness of 0.1 mm [8].*

Table 3.1. *The composition of SS316L; CrN/Cr coating from EDX measurements (wt.%).*

Material	**Composition (wt.%)**
SS316L	Fe68Cr17Ni10Mo2Si0.5C2.5
CrN/Cr	Cr83.1N16.1Fe0.75

3.1.2 Sample preparation and cleaning

All samples of bare and coated SS316L specimens without flow channels were cut into 30 mm× 30 mm sizes for the electrochemical tests. The bare SS316L specimens were polished with No. 600, 800 and 1200 SiC abrasive paper, then cleaned with 2-propanol and distilled water in an ultrasonic cleaner followed by a drying operation with a high-pressure airflow [8]. There are two types of CrN/Cr-coated specimens, one with and the other without artificially induced defects. The coating deposition parameters for these two types of CrN/Cr-coated specimens were the same. The only difference between them was the treatment of the substrate before the coating deposition. For the CrN/Cr-coated specimens with artificially induced defects, the substrate was dry polished by hand with No. 800 SiC abrasive paper hand to form deep grooves on the surface of the substrate which in turn would result in subsequent defects in the coating. The substrate of the CrN/Cr-coated SS316L specimen without artificially created defects was not polished prior to its coating deposition. In order to protect the initial surface of the CrN/Cr-coated specimens, polishing was likewise not performed before the corrosion tests, but cleaning was still performed (the surface was cleaned with 2-propanol and distilled water in an ultrasonic cleaner followed by a drying operation with high-pressure air flow).

Following surface cleaning, the sample was pressed onto the corrosion cell as WE and then 190 ml of 85 wt.% H_3PO_4 was poured into the glass cell. After three electrodes of the cell were connected to the Autolab potentiostat PGSTAT302N (Metrohm), the cell was purged with specific gas (nitrogen, hydrogen or oxygen) for 30 min at a flow rate of 50 ml min^{-1}. Subsequently, an additional electrochemical cleaning operation was performed on the bare SS316L samples to thoroughly remove the oxidant layer formed in the ambient environment. The electrochemical cleaning operation was performed via voltammetry in the potential window at between -0.5 V and 1.4 V for ten cycles, with a scan rate of 100 mV s^{-1} and finishing with a potentiostat holding at -0.5 V for 10 s. The coated specimens and metallic BPP with the flow channel were not subject to electrochemical cleaning operation since this would probably have caused damage to the coating and the channel's corner before the corrosion tests. To guarantee a homogeneous distribution of the electrolyte and pure gas atmosphere concentrations, the bulk electrolyte in the corrosion cell was continuously stirred during all measurements via a magnetic stirrer and purging at a gas flow rate of 20 ml min^{-1}.

3.1.3 The linear polarization method

Linear polarization method is regarded as the easiest way to directly measure corrosion; it includes determining the free corrosion potential (E_{corr}) and free corrosion current density (i_{corr}). The free corrosion potential, E_{corr}, is a mixed potential in which the anodic oxidation current, i.e., the free corrosion current density, i_{corr}, must equal the sum of the cathodic reduction current density (here, the proton reduction and, in the case of O_2 purging, the oxygen reduction as well)

[110]. For reactions that are essentially activation-controlled (i.e., charge transfer controlled reactions or mass transfer controlled reactions occurring at a rate much lower than the limiting rate), which normal occurs when the applied potential is notably different from the E_{corr}, the relationship of the net current as a function of the potential written in Frankel [54] as follows:

$$i_{net} = i_{corr} \exp\left[\frac{2.3(E-E_{corr})}{b_a}\right] - i_0 \exp\left[\frac{2.3(E-E_{corr})}{b_c}\right] \qquad \text{3-1}$$

Where b_a and b_c are the anodic and cathodic Tafel slopes, respectively. Using the linear polarization method, one can initially obtain the linear polarization curve of the system. Then, one extrapolates the anodic and cathodic regions to the crossover point, where the anodic and cathodic reaction rates (i.e., currents) are equivalent. At this crossover point, the current density is the i_{corr}, and the corresponding potential is E_{corr}, as shown in Figure 3.4 [111]. The linear polarization measurement employed in this work was conducted in the anodic direction from -0.5 V to 1.4 V with a scan rate of 5 mV s^{-1} for the bare metallic specimens. The lower starting potential of -0.5 V was selected because the anodic potential is able to reduce oxidant layer formed at the ambient atmosphere and minimize the influence of this oxidant layer on the corrosion properties of the specimens. For the coated samples, the linear polarization measurements were also performed in the anodic direction, while the potential range was only from – 300 mV vs. the open circuit voltage (OCV) which was to + 300 mV vs. OCV. Since the electrochemical behavior of the coating was the focus of the corrosion research on the coated specimens, this narrow potential range was normally chosen in order to protect the coating from damage by applying lower or higher potentials which would subsequently alter the corrosion behavior of the coated specimens.

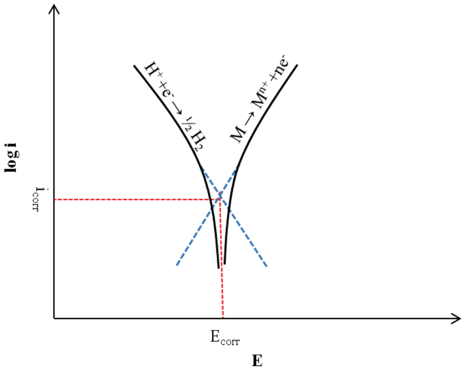

Figure 3.4. *The schematically measured polarization curve for metal M in an acid, showing E_{corr} and Tafel extrapolations for the determination of i_{corr}.*

3.1.4 The free corrosion potential monitor

With time, following electrochemical cleaning, further corrosion would be expected to take place on the surfaces of the specimens investigated. For further corrosion occurrences, however, conventional standard conditions cannot be assured for the following reasons: the activity of the participating ionic species varies strongly over time and is attributed to ongoing metal dissolution or the formation of passive layers; also, these films possessing unlike characteristics to those of the bare metal lead to a kinetic barrier against metal dissolution. The OCV monitoring, as the real-time E_{corr}, might reflect the differences in the passive layers of metals within the same electrolytic environment [8, 28].

Immediately following the electrochemical cleaning operation, the E_{corr} versus the time and temperature were monitored in order to investigate the process of dynamic passive layer formation. The E_{corr} was first monitored at RT, followed by a slow increase of the temperature at a rate of 1 ºC min^{-1} to 130 ºC, and then maintaining it at this level for another two hours. A higher temperature than 130 °C was not performed in this study after assessing the limitations of the equipment and the temperature requirements for simulating the HT-PEFC environment: first of all, the normal operating temperature of an HT-PEFC is in the range of 120 ºC-180ºC, and, as a result, the corrosion's operation temperature should fall within this range in order to simulate the corrosive environment of the HT-PEFC; on the other hand, raising the temperature to greater than 130 ºC would cause the electrolytes to vibrate markedly due to the water's high evaporation rate. The reflux condenser's inability to handle this high evaporation would eventually alter the electrolyte concentration, causing a measurement inaccuracy [30]. Following the potentiostatic tests (see Section 3.1.5), the E_{corr} versus time calculation was also immediately monitored until it became sufficiently constant for investigating the stability of the passive layer or the degradation of the coating which had occurred during the potentiostatic stage.

3.1.5 Potentiostatic tests

An operating hydrogen/air HT-PEFC has a potential range of 0-0.2 V vs. the RHE at the anode compartment and a potential range of 0.4-1.0 V vs. the RHE at the cathode [8, 108]. Under typical operating conditions, the potential of the cell is around 0.6 V, which results in roughly 0.65 V versus the RHE at the cathode electrode and around 0.05 V versus the RHE at the anode electrode. In a normal situation, the potentials in a real fuel cell deviate from the E_{corr} of the metallic BPPs in the specific environment. Therefore, corrosion studies with specifically applied potentials are fundamental and vital to the development of BPPs in fuel cells. In order to investigate the corrosion behavior of specimens within simulated cathodic and anodic environments, respectively, of HT-PEFCs, potentiostatic tests with simulated potentials were performed for 4 h at 130 ºC. The applied potentials used in the potentiostatic tests were based on the values in the real HT-PEFC of 0.65 V versus the RHE for the simulated cathodic side and 0.05 V versus the RHE for the simulated anode.

3.1.6 Electrochemical impedance spectroscopy

Electrochemical Impedance Spectroscopy (EIS), also known as AC impedance techniques, is a powerful in situ technique for the characterization of electrochemical systems, and is considered suitable for the study of electrochemical phenomena within fuel cells and the metal/solution interface, oxide films and surface treatments, and the corrosion behavior of coatings on metals. By using a single EIS measurement through a broad range of frequencies, it is possible to obtain the governing physical and chemical phenomena within electrochemical systems at a given situation [112]. Like all other impedance methods, the fundamental approach of the EIS consists of superimposing a small amplitude AC signal (current or voltage) on the electrochemical system of interest, and measuring the related response from the system (voltage or current) [110].

For example, a low amplitude sinewave ($E(\omega) = \Delta E \cdot \sin(\omega\ t)$) with a particular frequency, ω, is superimposed on the DC polarization voltage, E_0. As a result, a current sinewave response will occur, superimposed on the DC ($i(\omega) = \Delta i \cdot \sin(\omega\ t + \varphi)$) [112]. The sinewave phase for the current response is shifted concerning the applied amplitude sinewave. Using Ohm’s law (Equation 3.2), the impedance of the system can then be calculated, as:

$$Z(\omega) = \frac{E(\omega)}{i(\omega)} \qquad 3\text{-}2$$

Z(ω) is the impedance of the system investigated. From a mathematical point of view, Z(ω) is a complex quantity composed of a magnitude and a phase shift. Since the magnitude and phase shift of the impedance of the system depends on the frequency of the applied signal, one can acquire the impedance as a function of the frequency by varying the frequency of the applied signal [112]. Typically, in practice, a frequency range of 100 kHz – 0.01 Hz is used, and the amplitude of the signal used is 10 mV. For an analysis of the impedance data, an equivalent circuit model is employed, which applies to every element has its own physical or chemical meaning within the electrochemistry system. What follows is a commonly equivalent circuit in the corrosion region of the metal within an acidic electrolyte.

When you immerse a metal into a solution, a metal/solution interface will form, as shown in Figure 3.5. As shown in Figure 3.5, for a freely corroding surface, an electrical double layer (edl) will be formed at the metal/solution interface due to the automatic arrangement of the charged species [110]. Based on this understanding, a simple equivalent circuit is proposed to simulate the metal/solution interface, as detailed in Figure 3.5. The equivalent circuit contains three elements, each of which has assigned to it its own physical or chemical significance within the specific system: double-layer capacitance, C_{dl}; polarization resistance, R_p and solution resistance, R_s [110]. In most cases, due to the complexity of the corrosion process, it is necessary to add more elements with specific physical or chemical meanings into this simple equivalent circuit, which depending on the specific corrosion system under investigation.

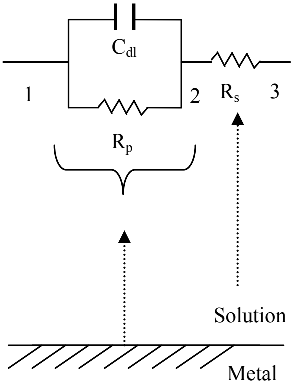

Figure 3.5. *An equivalent electric circuit for an electrical double layer.*

For the implementation of the EIS measurement, a stable state is required for the investigated system. Therefore, in this work, a pre-stationary stage was employed by applying the specific potential for half an hour prior to performing the impedance measurement. Once the pre-stationary stage was finished, the EIS was taken to a range of between 100 kHz and 10 mHz with a voltage amplitude 10 mV for the free corrosion potential conditions and 30 mV for the potentials deviating from the free corrosion potential.

3.2 Single Cell Test

After the corrosion mechanism research on bare and coated metallic materials within a simulated HT-PEFC environment, single cell tests with different types of BPPs (graphite, bare metallic and coated metallic) was conducted, while maintaining the constancy of all other factors.

The main aspects that might affect the performance of an HT-PEFC included the fabrication process and the MEA materials, the material and design of the flow field on the BPP, the backpressure of the gases and the temperature and stoichiometry of gases, among other factors [113-115]. By keeping all other elements constant, and only changing the material of the BPP, it was possible to investigate the influence of the plate's materials on the performance of the HT-PEFC. Additionally, the durability of the different single cells with BPPs of diverse materials was compared by running the cells for 1000 h. All single cells were tested in an automated test rig available at the Forschungszentrum Juelich with a Baltic Module, as shown in Figure 3.6.

Figure 3.6. *The diagram of the test rig.*

3.2.1 Basic information on the test rig and single cells

The test rig was mainly composed of five devices: a data acquisition system, an electronic load, mass flow controllers, LabVIEW software and the Baltic module. The process and instrumental diagram of the test rig are shown in Figure 3.7.

The single cell used for this thesis is the Baltic quickCONNECTfixture (qCf). By using qCf, all varieties of fuel cell internal components including the BPP could easily be monitored [116]. The flow field from Home-design & Made could easily be exchanged. Figure 3.8 illustrated the assembled and disassembled 3D model. The Baltic module is mainly composed of two parts: (i) the support frame pressure unit (SFPU) is connected to the test rig with the function of supporting and sealing the cell fixture using a pneumatic actuator to apply specific pressure to it; (ii) the cell fixture (cf) is the test cell where the samples of interest (such as the BPPs in this work) are placed.

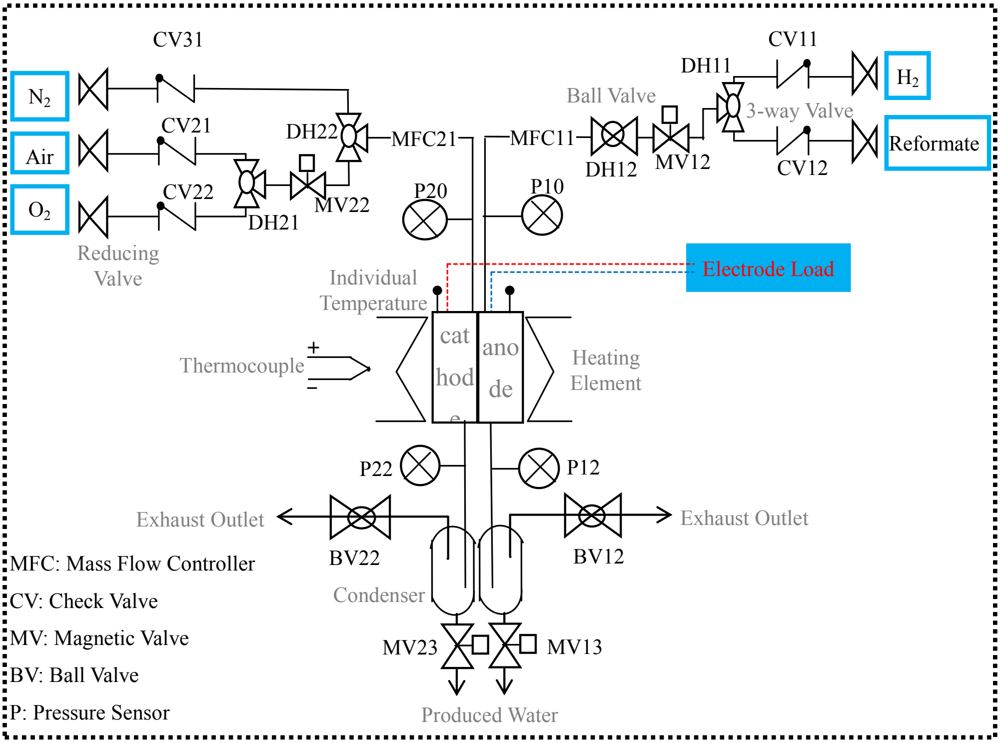

***Figure 3.7.** A diagrammatic sketch of the test rig.*

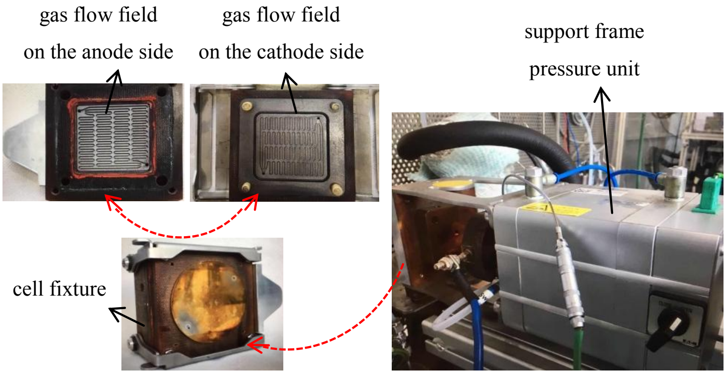

***Figure 3.8.** The baltic module disassembled and assembled.*

3.2.2 The materials and sample preparation

In this work, three different types of BPPs were examined. After considering the special structure of the Baltic module, adapted BPPs with an active area of 25 cm^2 and serpentine flow field design was developed at Forschungszentrum Juelich to fit into the Baltic module, as shown in Figure 3.9. All the tested BPPs exhibited the same flow field design, but by using different materials. Each type of BPP was described in the follows:

- Graphite BPP: This type of BPP from Eisenhuth was made from PPS material (graphite and polyphenylenesulfide). The PPS material was the standard material used in our lab for the graphite BPP. This type of BPP was manufactured by machining method. It was cleaned with water and isopropanol and dried with compressed air before being assembled into the Baltic module.
- Bare metallic BPP: This type of BPP was made from 316L stainless steel (SS316L) and had the same composition as that of the SS316L material described in Section 3.1, and illustrated in Table 3.1. This type of BPP is also manufactured by machining method. It was cleaned with water and isopropanol and dried with compressed air prior to being assembled into the Baltic module.
- CrN/Cr coated metallic BPP: This bare metallic BPP with SS316L was likewise fabricated by machining method; it was initially cleaned and degreased with water and isopropanol. The sample was then coated with CrN/Cr by Teer Coating, Ltd.

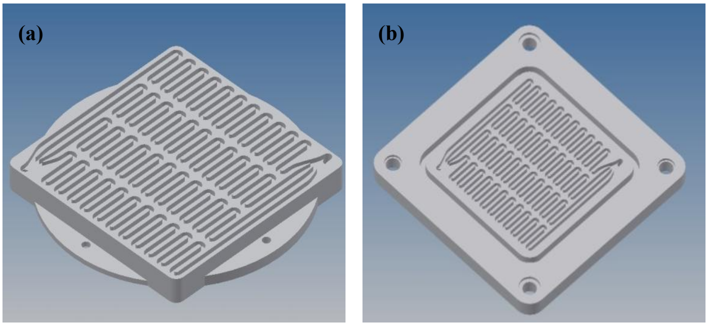

Figure 3.9. *An illustration of the bipolar plate. (a) anode side. (b) cathode side.*

3.2.3 Electrochemical characterizations

Identical PBI-based Dapozol® membrane-electrode assemblies (MEAs) from Danish Power Systems (DapoSy) have been employed for all the measurements. The diagram of the test procedure and electrochemical characterizations is shown in Figure 3.10. After assembling the cell and fixing it into the test rig, the MEAs were initially run for break-in purpose. First, the cells were fed at the anode and cathode electrodes, respectively, with dry hydrogen and air under atmospheric pressure and at room temperature (RT); then, the cells were heated to 160 ºC, followed by having the current increased up to 200 mA cm^{-2}, at increments of 50 mA cm^{-2}. Afterward, the cells were operated on a constant current density of 200 mA cm^{-2} for 70 h for break-in purposes. The flow rate during the break-in procedure was kept constant with a stoichiometry of $\lambda_{H2/air} = 2/2.5$ at 200 mA cm^{-2}.

At the end of the break-in procedure, the polarization curve (UI curve) was performed. During the polarization curve operation, the current density was increased from 0 to 1.1 A cm^{-2}, with an increment of 50 mA cm^{-2}. Each value of the current density was held for 2 min. The flow rate was set to a stoichiometry of $\lambda_{H2/air} = 2/2.5$. In the case of the current densities lower than 200 mA cm^{-2}, the flow rate was maintained at values identical to the one at 200 mA cm^{-2} [114].

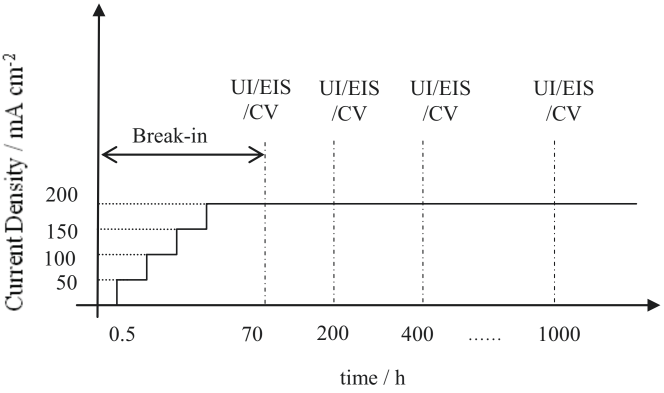

Figure 3.10. *A diagram of the test procedure and the electrochemical characterizations.*

To quantify in situ the resistances of the HT-PEFC, EIS measurements were also performed at the end point of the break-in procedure with an IM 6 unit of Zahner Elektrik. All tests were carried out in a “hybrid” mode; the cells were operated on a constant current density of 200 mA cm^{-2}, while using a voltage amplitude of 10 mV. The frequency chosen was in the range of 100 kHz – 50 mHz. The obtained impedance data were simulated by the transmission line equivalent circuit shown in Figure 3.11 [118].

- Ohmic resistance (R_Ω): R_Ω is the combined ohmic resistance of several components of the cell assembly. The main contribution to this value is the membrane resistance of a fuel cell. Therefore, R_Ω is often referred to as membrane resistance.
- Proton resistance (R_p): R_p is the protonic resistance in the CLs. R_p is mainly influenced by

the interface and structure of MEA which independent of the BPPs' material.

- Charge transfer resistance R_{ct}: R_{ct} represents the charge transfer resistance of the oxygen reduction reaction (ORR).

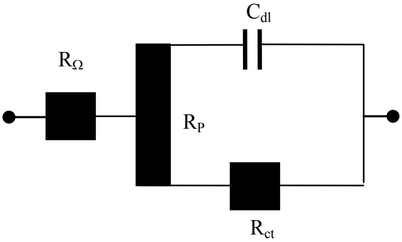

Figure 3.11. *Equivalent circuit for HT-PEFC.*

3.2.4 Durability test

A durability experiment up to 1000 h was performed on all single cell tests under a constant load of 200 mA cm^{-2}. At the end of their lives, the polarization curves and EIS measurements were performed again.

3.3 Material characterization

In order to characterize changes in morphology within the simulated HT-PEFC environment and under real HT-PEFC conditions, the corrosion products, the degradation of the coating materials and the leaching of the metal ions within the electrolyte and MEA, an extensive Post Mortem Analysis (PMA) was performed before and after the corrosion tests.

3.3.1 Scanning Electron Microscopy (SEM) and Energy-Dispersive X-ray Spectroscopy (EDX)

Scanning Electron Microscopy (SEM) uses a type of electron microscope able to produce high-resolution images of material's surface topographies by scanning their surfaces with a focused beam of electrons. Energy-dispersive X-ray Spectroscopy (EDX) is an analytical technique mainly used for elemental analysis. In this project, the morphologies of specimens and the elements of the corrosion products and coatings were investigated at high magnification using an SEM/EDX combination system from Zeiss Gemini Ultra Plus.

3.3.2 Inductively Coupled Plasma -- Optical Emission Spectrometry (ICP-OES)

Inductively coupled plasma – optical emission spectrometry (ICP-OES) is a type of emission spectroscopy used in the detection of trace elements. As known from its name, ICP-OES uses inductively coupled plasma to excite atoms or ions to a higher energy level so that, when they return to their original ground states, will emit electromagnetic radiation with wavelengths characteristic of their particular element. In this work, for an analysis of the elements leaching from metallic materials into the electrolyte (phosphoric acid) within the simulated HT-PEFC environment, the phosphoric acid was collected following the corrosion tests and then analyzed using ICP-OES. To analyze the metal ions dissolved into the MEA from the metallic BPP in a real HT-PEFC, all the MEA samples following the 1000 h durability tests were put into 200 ml aqua regia (3:1 HCl/HNO_3) at 70 ºC for 1 h for leaching. The solutions were then diluted in pure water and analyzed by ICP-OES.

3.3.3 X-ray Photoelectron Spectroscopy

The X-ray Photoelectron Spectroscopy (XPS) is a surface-sensitive quantitative spectroscopic technique. It is normally used to measure the elemental composition of the superficial layers of materials (a few atomic layers) and even the chemical states of the elements. As seen from its name, XPS uses x-rays to irradiate the investigated material, and attains information on the superficial elements by analyzing the electrons that escape from the top of the material. In this work, XPS analysis was used to investigate the element distribution of the corrosion products on the surfaces of the metallic specimens. It was carried out on a Phi 5000 Versa Probe Π (ULVAC-PHI, Inc., USA) with a monochromatic Al Kα radiation X-ray source (1.486 keV). The base pressure during all the experiments was in the rage of 10^{-8} mbar, with the depth profiles obtained through sputtering the samples with 1 keV argon ions. To estimate the sputtering rate, a Si specimen with a thin SiO_2 layer was sputtered all the way through, yielding a rate of about 8.5 Å min^{-1}.

3.3.4 Interfacial contact resistance (ICR)

Electrical resistance consumes electricity and transforms it into heat. Therefore, the ICR between a BPP and the GDL requires comprehension as it is critical for the output power of a fuel cell. The method used for the ICR measurement was developed by Wang *et al.* [119]. In our setup, two pieces of GDL (type H2315) (Freudenberg Inc.) were sandwiched between the specimen and two gold-coated copper plates, as illustrated in Figure 3.12. A constant current of

1.0 A through the BPPs/GDL system was provided by a power source via the two copper plates. By measuring the relationship of the voltage drop between the two gold-coated copper plates and the compression force, one could ascertain the total resistance dependency on the compaction force [119]. Thus, the total resistance measured above is the sum of four interfacial parts: two GDL/gold coated copper plate interfaces and two GDL/specimen interfaces. A calibration of the ICR between the GDL and the gold-coated copper plate should be performed using only one GDL which was sandwiched between the two gold-coated copper plates. After this correction, halving the result would provide the ICR value of the BPP/GDL interface [119].

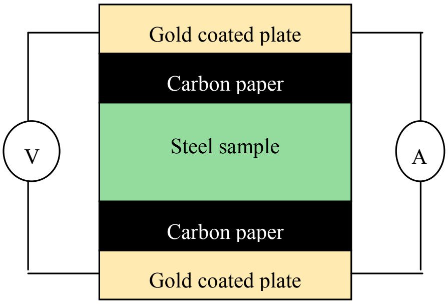

Figure 3.12. *Setup for the interfacial contact resistance measurements.*

Chapter 4 The Electrochemical Corrosion of Metallic Material in Phosphoric Acid

The corrosion and the passive mechanism of the bare metallic BPP within the phosphoric acid is still a critical question for an investigation into the possibility of using metallic BPPs within HT-PEFCs and maybe aid in seeking a suitable anti-corrosion coating for this application, while the answers are still unclear to date; this particularly applies to the specific anodic and cathodic environments of HT-PEFCs with different gases purged atmospheres. It is important to understand the corrosion behavior, properties and composition of the passive layer of the bare metallic BPP within the simulated environment of the HT-PEFC (85 wt. % H_3PO_4). A 316L stainless steel (SS316L) sheet with a thickness of 0.1 mm is the object most extensively investigated for an understanding of metallic BPPs in low-temperature polymer electrolyte fuel cells (LT-PEFCs), mainly for two reasons: its reasonable anti-corrosion capabilities in a corrosive environment, and the low cost for its mass production. The SS316L material also demonstrates reasonable corrosion resistance among different types of metallic materials when in hot phosphoric acid with an N_2 atmosphere in a simulated HT-PEFC environment [25]. As a result, SS316L sheets with a thickness of 0.1 mm were chosen as this chapter’s research subject and as the substrate material for the coated specimens in this thesis. This chapter investigates the corrosion and electrical properties of SS316L in the simulated environment of HT-PEFC. By purging different gases (nitrogen, hydrogen, and oxygen) into the electrolyte, the influence of the gases on the electrochemical behavior and composition of the passive layer of the SS316L material formed in the simulated HT-PEFC environment was also studied. This work was published [8].

4.1 Potentiodynamic tests

Since corrosion studies, depending on the applied potential, are fundamental to the research on metallic BPPs for fuel cells, the potentiodynamic polarization curves of the SS316L in a simulated HT-PEFC environment at RT and 130 °C from -0.5 V – 1.4 V vs. RHE were recorded with a scan rate of 5 mV s^{-1}, as demonstrated in the Tafel plots in Figure 4.1. By purging different gases (nitrogen, hydrogen, and oxygen) into the electrolyte, the influence of these gases on the corrosion behavior of SS316L in phosphoric acid was also investigated. As explained in Chapter 3, anodic polarization beginning at a low value of -0.5 V is used to remove the passive layer formed before the test. By applying the Tafel theory and linear polarization method as explained in Chapter 3, the corrosion parameters for the SS316L material in all environments were obtained, as given in Table 4.1.

The free corrosion potential, E_{corr}, is a mixed potential in which the anodic oxidation current, i.e., the oxidation and release of metal ions from the metallic electrode, must equal the sum of the cathodic reduction currents (here, proton reduction and, in the case of O_2 purging, it also includes oxygen reduction) [110]. From Figure 4.1 and Table 4.1, the free corrosion potentials (E_{corr}) for SS316L in 85 wt.% H_3PO_4 were ca. -75 mV at RT, which shifted to ca. -20 mV at 130 °C, independent of the purge gas. This indicates that the additional oxygen reduction reaction in the case of the O_2 purging had no influence on the E_{corr} of SS316L, with its clean surface in 85 wt.% H_3PO_4 at RT and at an elevated temperature. The free corrosion current densities (i_{corr}) of SS316L in 85 wt.% H_3PO_4 are ca. 20 μA cm^{-2} at RT, independent of the gas environment. When the temperature was heated to 130 °C, i_{corr} of SS316L increased to about 140 μA cm^{-2} in the oxygen- and nitrogen purged environments. From these results, one conclusion is that the oxygen also had no influence on the i_{corr} of SS316L with its clean surface in 85 wt.% H_3PO_4 at RT and elevated temperature. This behavior might be explained as being that the oxygen reduction as a possible additional cathodic reaction could be neglected due to the very low solubility of O_2 in concentrated phosphoric acid of ca. $1.7 \cdot 10^{-4}$ M as compared with $1.3 \cdot 10^{-3}$ M in water [25, 120, 121]. Remarkably, in the case of the hydrogen purged environment at 130 °C, the i_{corr} of SS316L in 85 wt. % H_3PO_4 is ca. 270 μA cm^{-2}. This is about two times higher than the corrosion current density of SS316L in the nitrogen- purged and oxygen purged environments. This indicates that the presence of hydrogen will dramatically increase the corrosion rate of SS316L at elevated temperatures in concentrated phosphoric acid. The DOE requirement for corrosion current densities of less than 1 μA cm^{-2} for metallic BPPs in fuel cells could not be reached in this research [23]. Therefore, SS316L should be coated in order to reduce corrosion to levels acceptable for application by an HT-PEFC.

From Figure 4.1, it could be seen that all curves can be divided into three regions, namely active, passive and trans-passive. In the range of potentials of from E_{corr} to 0.1 V, the SS316L is in the active region of corrosion for all cases. Afterward, passivity occurred at between ca. 0.1 and 1.2 V. Finally, transpassivity began at ca. 1.2 V. The anode potential of an operating HT-PEFC (~0.05 V) is located in the active region of the SS316L corrosion, while the cathode potential of an operation HT-PEFC (~0.65 V) is in the passive region of the SS316L corrosion, as shown in Figure 4.1 [108].

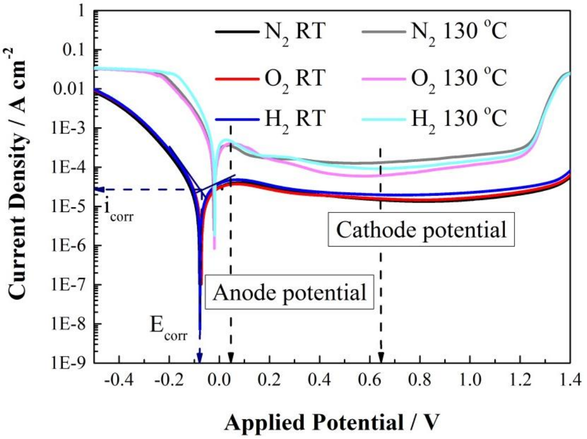

Figure 4.1. *Potentiodynamic polarization of SS316L in 85 wt.% H_3PO_4 at RT and 130 °C, bubbled with nitrogen, hydrogen or oxygen [8].*

Table 4.1. *Polarization parameters of SS316L in 85 wt.% H_3PO_4 at RT and 130 °C bubbled with N_2, H_2 or O_2 [8].*

Gases	**E_{corr} (mV) / RT**	**i_{corr} (μA cm^{-2})/ RT**	**E_{corr} (mV) / 130 °C**	**i_{corr} (μA cm^{-2})/ 130 °C**
H_2	−82.6	19.3	-20.7	270
O_2	−79.6	18.7	-21.7	155.3
N_2	-77.3	19.7	-21.3	158

4.2 The free corrosion potential of SS316L with a corroded surface

For further corrosion, the activity of participating ions varies strongly over time and is attributed to ongoing metal dissolution and the precipitation of passive layers. Furthermore, these passive layers with different properties from those of the bare metal surface which will lead to a kinetic barrier against metal dissolution [28]. Due to these reasons, the conventional standard conditions cannot be assured in the presence of a corroded surface. E_{corr}, as the resulting mixed potential, might reflect the different properties of the passive layer in the same electrolyte environment.

Figure 4.2 shows the progress of the E_{corr} vs. time for SS 316L in 85 wt.% H_3PO_4 with different gas purged environments, at RT and elevated temperature. Measurements were commenced at RT for 20 h directly after the electrochemical cleaning operation, as shown in Figure 4.2 (a). E_{corr} had initially risen relatively fast within the first 2.5 h, when further increases in E_{corr} become fairly slow in all cases. This passive procedure indicates a two-step corrosion mechanism and keeps to the agreement concerning the modeled bilayer passive film structure (a compact inner layer and outer porous layer) described by Clayton and Macdonald [122, 123].

In the N_2 and H_2 purged environments, E_{corr} revealed a similar trend at RT which rose from ca. -100 to ca. 300 mV during the first rapid-growth stage, followed by a slow increase in E_{corr} to about 400 mV during the second stage. Alternately, the O_2 purged environment displayed a lower value of E_{corr} at RT: during the first stage, E_{corr} increased from ca. -80 to 170 mV, slowly increasing up to ca. 250 mV in the subsequent stage. In contrast, the E_{corr} of SS316L in the O_2 purged environment was ca. 140 mV lower than that in the N_2 or H_2 purged environments during the first rapid-growth stage. The different increments of E_{corr} between the O_2 purged and N_2 or H_2 purged environments was only 8 mV during the second slow-growth stage. After removing the original passive layer formed in the ambient atmosphere by polishing and electrochemical cleaning operation, the metal surface formed a new type of passive layer of a different metallurgical composition and structure based on the corrosion environment [124]. This inferred that the existence of oxygen changed the structure and composition of the passive layer, especially the compact inner layer of oxide, formed within the 85 wt.% H_3PO_4.

After remaining at RT in phosphoric acid for 20 h, the corrosion cell was continuously heated up to 130 °C at a heating rate of 1 °C min^{-1}, subsequently held at 130 °C until the potential restabilized. The process of the E_{corr} during the heating process and elevated temperature (130 °C) is shown in Figure 4.2(b). This heating operation was able to investigate the effects of temperature on the dynamic depletion of the passive layer formed at RT. The rectangles in the temperature curve show the measured temperature with a standard deviation of 5 ºC [25]. From Figure 4.2(b), it is shown that the decline in E_{corr} begins at around 40 °C and the trend of decrease accelerates with rising temperature. Remarkably, in the O_2 purged environment, it shows three potential plateaus at 110 mV, 23 mV and finally at -12 mV during the heating process. Conversely, in the N_2 and H_2 purged environments, the E_{corr} drops from about 400 mV directly to ca. 17 mV. The different behaviors of E_{corr} of SS316L in 85 wt.% H_3PO_4 during the heating process indicate the higher stability of the passive layer in the O_2 purged environment against the harsh environment of concentrated phosphoric acid as compared to the other two environments without the presence of O_2.

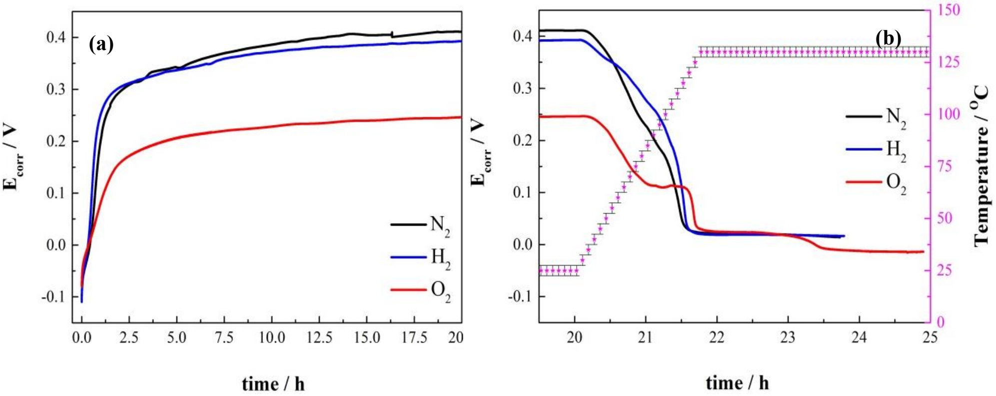

Figure 4.2. *The progress of E_{corr} measured in 85 wt.% H_3PO_4 for 20 h at RT (a) and elevated temperature (b) (against RHE in 85 wt.% H_3PO_4 at RT), bubbled with N_2, H_2 or O_2 [8].*

4.3 Potentiostatic Tests

An operating hydrogen/air HT-PEFC has a potential range of within 0 – 0.2 V vs. the RHE at the anodic side and a potential range of within 0.4 – 1.0 V vs. the RHE at the cathodic side [108]. In a normal situation, the HT-PEFC will run under a potential of around 0.6 V, which will give a reasonable power output. Under this typical operation condition, the electrode potential is about 0.65 V vs. the RHE at the cathodic side and 0.05 V at the anodic side. In order to understand the corrosion behavior of the SS316L at simulated anode and cathode electrodes of HT-PEFC under operating conditions, potentiostatic tests were conducted. Figure 4.3 shows the relationship of the current density versus time under specific potentials during the potentiostatic tests.

Figure 4.3 illustrates that all curves began with a rapid current density decrease at the outset of the potentiostatic tests and then gradually stabilized at a different level. For the simulated anodic environment of HT-PEFC (0.05 V vs. RHE bubbled with N_2 or H_2), the current density stabilized at ca. 60 μA cm^{-2}. Alternately, for the simulated cathodic environment of HT-PEFC (0.65 V vs. RHE bubbled with N_2 or O_2), the current density finally stabilized at around 6 μA cm^{-2}, which is 10 times lower than that of the simulated anodic environment. From Figure 4.1 and Section 4.1, it could be concluded that 0.05 V was located on the edge of the active region of corrosion and 0.65 V lay within the passive region. This is the reason that the specimens revealed 10 times higher corrosion rates in the simulated anodic conditions of an operating HT-PEFC as compared with those under simulated cathodic conditions.

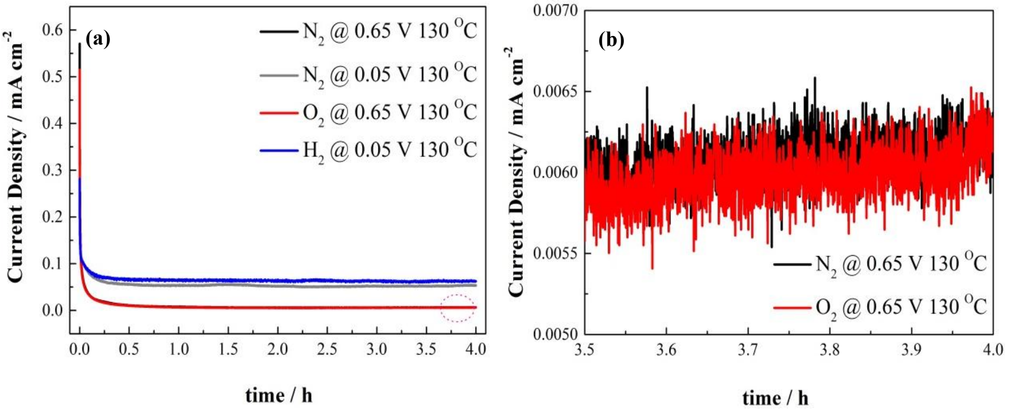

Figure 4.3. *Potentiostatic curves for the SS316L at the simulated anodic environment of HT-PEFC (0.05 V vs. the RHE, bubbled with N_2 and H_2) and simulated cathodic environment of HT-PEFC (0.65 V vs. the RHE, bubbled with N_2 and O_2) in 85 wt.% H_3PO_4 at 130 °C (a) an enlarged depiction of the circular portion (b) [8].*

Since E_{corr}, as the resulting mixed potential, could reflect the properties of the passive layer, it was deemed meaningful to monitor the potential decay of the specimens immediately following the potentiostatic tests, as shown in Figure 4.4. Since the 0.05 V was located close to the edge of the active region, almost no passive layer was expected to form on the surface of the metal. As a result, when the applied potential was removed, it was predicted that the surface of the metal would quickly return to its original state before the potentiostatic tests. From Figure 4.4, it could be seen that, for the simulated anode environment, the E_{corr} indeed rapidly decreased to ca. -20 mV within the first 5 min, and then stabilized at this value (the same range of E_{corr} before the potentiostatic test) after 4 h of potentiostatic polarization. Remarkably, for the simulated cathode environment, the E_{corr} of the SS316L showed a different decay trend after the potentiostatic tests at 0.65 V for 4h as compared with that of the simulated anode environment. For the N_2 purged environment, the E_{corr} slowly decreased from around 400 to -20 mV over a longer period than 1 h following potentiostatic polarization at 0.65 V for 4 h. Alternately, for the O_2 purged environment, the E_{corr} remained stable at ca. 0.45 V after the potentiostatic test at 0.65 V. Since the potential of 0.65 V was located in the passive region of corrosion for SS316L in hot phosphoric acid, the passive layer should have formed on the surface of the specimen following polarization for 4 h at this potential. The slow decay of E_{corr} in the N_2 purged environment indicated the slow depletion of the passive layer in hot phosphoric acid, so that the passive layer formed within the simulated cathode environment of HT-PEFC with the N_2 purged environment could not tolerate the harsh environment of hot phosphoric acid. By contrast, the E_{corr} stability of the specimen in the simulated cathode environment of an HT-PEFC with an O_2 purged atmosphere demonstrates the high stability of the passive layer within this environment and the passive layer's ability to survive in the harsh, corrosive environment of hot phosphoric acid.

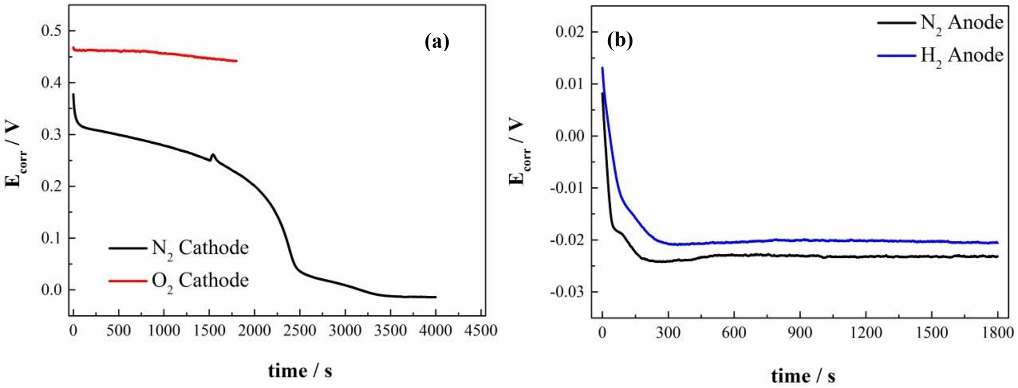

Figure 4.4. *Potential decay of SS316L following potentiostatic tests in the 85 wt.%* H_3PO_4*: (a) specimen following the potentiostatic operation at 0.65 V, bubbled with* N_2 *or* O_2*; (b) specimen following the potentiostatic operation at 0.05 V, bubbled with* N_2 *or* H_2 *[8].*

There are two explanations for the higher stability of the passive layer in the simulated HT-PEFC environment with an O_2 atmosphere: one is that the composition of the passive layer formed in the simulated cathodic environment of the HT-PEFC with an O_2 purged atmosphere differs from the one formed in the N_2 purged atmosphere; the other is that the presence of the O_2 had the effect of blocking the elements of the passive layer. Through an analysis of the elements of the passive layer formed in the simulated cathodic environment of the HT-PEFC by XPS (as shown in Figure 4.8), the element compositions of the passive layer formed in the O_2- and N_2 purged atmosphere were similar. Therefore, the second explanation that the O_2 blocked the elements of the passive layer from dissolving in the hot phosphoric acid, possibly causing the higher stability of the passive layer in the simulated HT-PEFC environment with an O_2 purged atmosphere.

4.4 SEMs of specimens after potentiostatic tests

Figure 4.5 shows the surface morphology of SS316L before and after potentiostatic tests assessed by SEM. Figure 4.5 (a) shows the original specimen without corrosion test. By comparison, after corrosion by potentiostatic tests at 0.65 V for 4 h, the corrosion product appeared on the surface of the specimen, as shown in Figure 4.5 (b) and (c). The morphologies of the corrosion products in the N_2 and O_2 purged environments are different from each other. It is assumed that the mottled surface of the specimen corroded under the N_2 purged environment is mainly due to the break-down of the passive layer, which results in a higher difference in conductivity between the passive layer and substrate. The surface of the specimen following corrosion under an O_2 purged environment shows a good color balance, indicating that the homogeneous coverage of the passive layer on the surface of the substrate surface is due to the higher stability of the passive layer in the simulated HT-PEFCs with an O_2 purged atmospheres.

As explained before, the potential of the anodic electrode of an HT-PEFC (0.05 V) is located in the active region of corrosion which will not form a passive layer on its surface. As a result, the specimen corroded under the simulated anodic side of the HT-PEFC with both the N_2 and H_2 purged environments still showing clean surfaces, as displayed in Figure 4.5 (d) and (e).

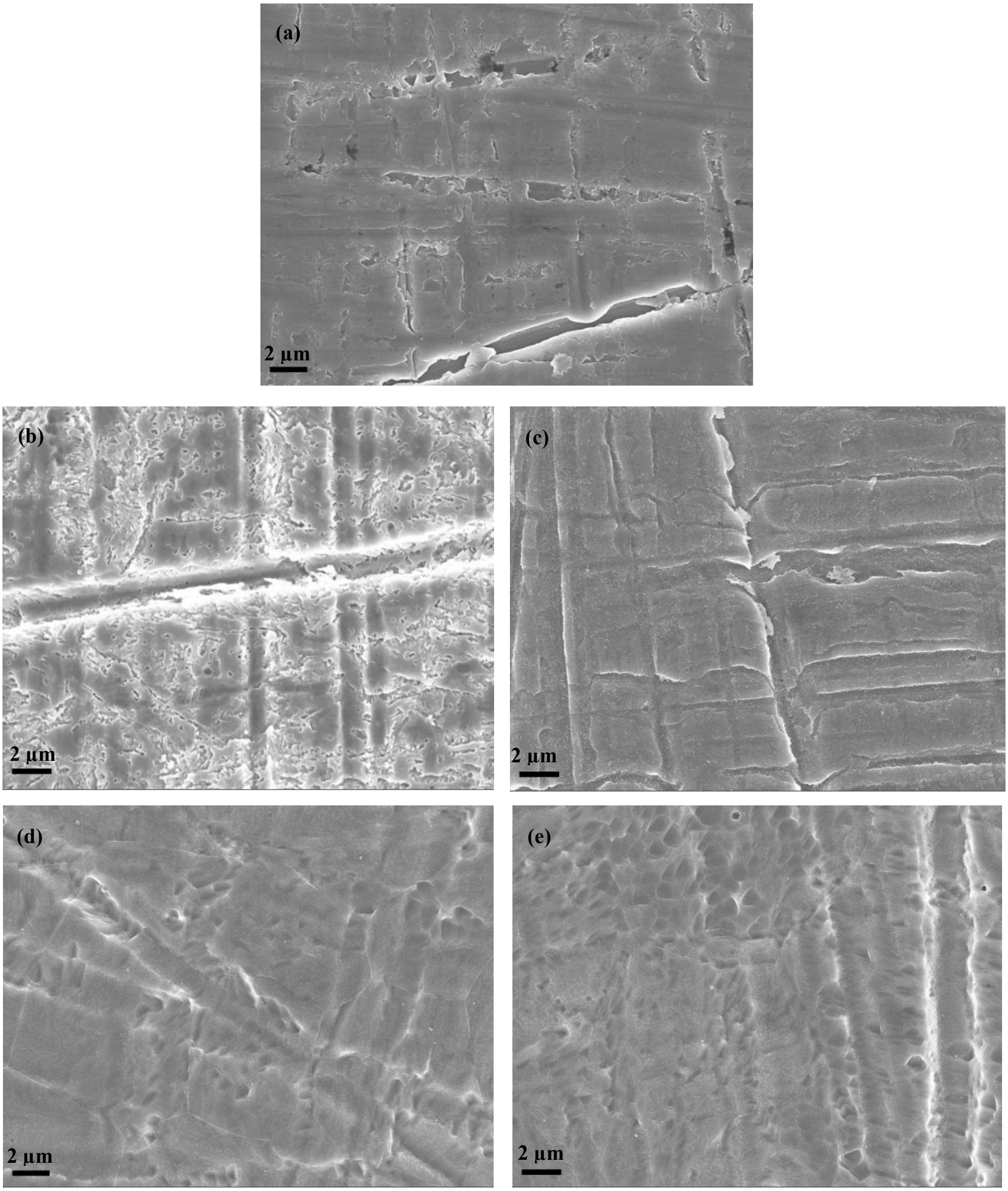

Figure 4.5. *SEM of SS316L, following potentiostatic corrosion in 85 wt.% H_3PO_4, at 130 °C: (a) a fresh sample without corrosion; (b) a sample after potentiostatic corrosion at 0.65 V, bubbled with N_2; (c) a sample after potentiostatic corrosion at 0.65 V, bubbled with O_2; (d) a sample after potentiostatic corrosion at 0.05 V, bubbled with H_2; (e) a sample after potentiostatic corrosion at 0.05 V, bubbled with N_2 [8].*

4.5 ICP-OES measurements

One of the degradation mechanisms of a fuel cell with the metallic BPPs is its leaching metal ions from the metallic BPP into the MEA; this will poison the catalyst and membrane by blocking the active area, which will, in turn, decrease the performance of the fuel cell [125]. Thus, it is important to characterize the type and amount of metal ions released into the solution from the metallic BPP due to corrosion. In order to provide a more precise estimation of the ions being leached from a real metallic BPP, this measurement was conducted using a real metallic BPP with flow channels, as shown in Figure 3.3 (b). After the potentiostatic tests at 130 ºC for 4 h in 85 wt.% H_3PO_4, with different potentials and gas environments, the solutions were collected, and the nature of the dissolved metal ions in the solutions was determined by ICP-OES. The results are shown in Figure 4.6.

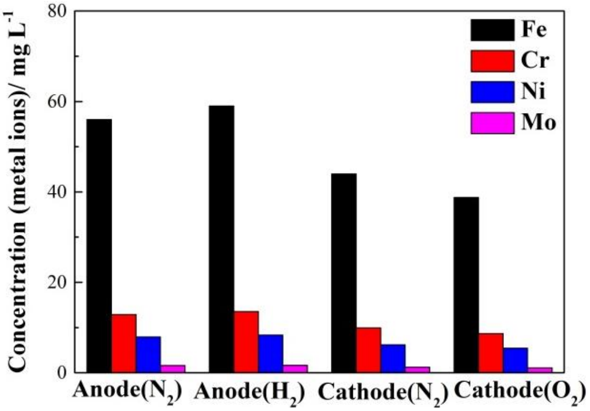

Figure 4.6. *The content of various metal ions leaching from the metallic bipolar plate with flow channels following the potentiostatic test conducted for 4 h at 130 °C, measured by ICP-OES [8].*

Figure 4.6 shows that the metal ions concentration in the simulated anode environment was higher than that in the cathode one. This behavior corresponds to the previous conclusion that corrosion rates of SS316L in a simulated anode environment are higher than those at the simulated cathode environment. And the sample corroded at the simulated anodic side of HT-PEFC with the H_2 purged environment shows the highest concentration of metal ions, which also corresponds with the corrosion rates shown in Figure 4.3. The corrosion rates of the specimens at the simulated cathode side of HT-PEFC with the N_2 and O_2 purged environments are the same, as shown in Figure 4.3. But from Figure 4.6, the concentration of metal ions within the electrolyte following the potentiostatic tests at the simulated cathodic side of the HT-PEFC with the N_2 and O_2 purged environments reveals different values. This can be explained by the higher stability of the passive layer at the simulated cathodic side of the HT-PEFC with the O_2

purged environment as compared with that with the N_2 purged environment. An interval exists between the end of the potentiostatic test and removal of the electrolyte at an elevated temperature which causes the metal ions in the passive layer to dissolve into the electrolyte in the N_2 purged environment, while almost no metal ions leach from the passive layer formed in the O_2 purged environment.

4.6 Interfacial contact resistance

Besides the poisoning effect of metal ions on catalysts and membrane, the increased interfacial contact resistance (ICR) of the metallic BPP following corrosion is also the main reason for the degradation of metallic BPP fuel cells via the apparent decrease in the overall power output. In order to investigate the influence on the ICR of the passive layers formed in different environments, the ICR measurements of the metallic BPPs with flow channels before and after the 4 h potentiostatic tests were conducted using the method mentioned in Chapter 3; the results are shown in Figure 4.7. One side of the metallic BPP with flow channels was corroded in the simulated anodic side (0.05 V and bubbled with N_2 or H_2) or the simulated cathodic side's environment (0.65 V bubbled with N_2 or O_2) using 85 wt.% H_3PO_4 at 130 ºC; the total contact resistance of the two interfaces (GDLs with both sides of the specimen) is shown in Figure 4.7.

From Figure 4.7, it can be seen that the values of ICR gradually decrease in all cases with increases in the compact force, due to the ICR being dominated by the effective contact area between the specimen and GDL, which increments with increasing compact force [126-128].

For the simulated anodic environment of the HT-PEFC, the specimens display a relatively lower ICR value than the original following 4 h of potentiostatic polarization at 0.05 V with both N_2 and H_2 purged environments. This is due to the active corrosion behavior of SS316L at 0.05 V in hot phosphoric acid regardless of the nature of the purged gases; the corrosion removes the oxide layer formed under an ambient atmosphere from the surface of the original. However, after corrosion with a simulated cathode environment of HT-PEFC, the ICR values of the specimen became higher than those of the original across all of the compact force range. This can be attributed to the formation of passive layers caused by the passive corrosion at 0.65 V. It is interesting to note the ICR values of the specimen following corrosion under a simulated cathodic environment exhibits different behaviors with different gases. The specimen corroded in the O_2 purged environment gives a lower ICR value as compared with that in the N_2 purged environment one. As shown in Section 4.4, the surface of the corroded specimen in the simulated cathodic environment of HT-PEFC with its N_2 purged atmosphere is less homogeneous, which implies a less effective contact area between the specimen and GDL and leads to a relatively higher ICR value.

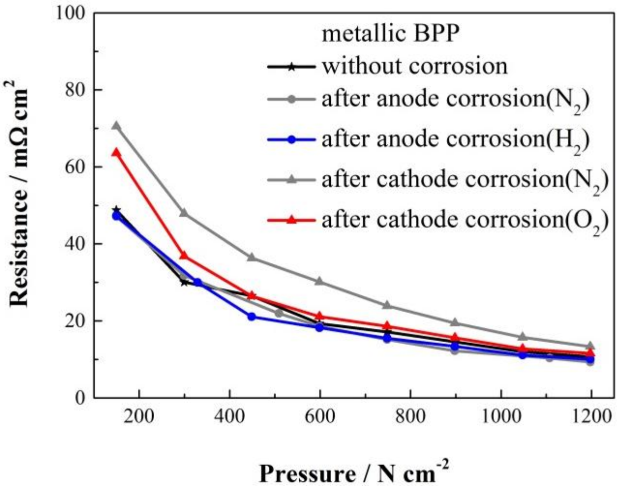

Figure 4.7. Interfacial contact resistances for a metallic bipolar plate with flow channel before and after corrosion tests and a gas diffusion layer under different compaction forces [8].

4.7 The XPS depth profile

From the previous portions of this chapter, it is seen that the passive layer formed inside the simulated cathode environment of an HT-PEFC with an N_2 and O_2 purged environment demonstrates unlike electrochemical behaviors and stability in hot phosphoric acid. In order to clarify the reason for these phenomena and find some indications in the search for suitable coating materials, it would be interesting and helpful to analyze the composition of the passive layers formed under different HT-PEFC environments.

In a normal situation, the thicknesses of the passive layers due to corrosion are mostly in the range of nanometers, deeming it necessary to employ a method of characterization which detects depth in nanometers. Since X-ray Photoelectron Spectroscopy (XPS) is a very surface-sensitive quantitative spectroscopic technique that can measure the elemental composition of the top few atomic layers of material (less than one nanometer), the XPS depth profiles of specimens before and after corrosion tests under different conditions were conducted, as shown in Figure 4.8. As explained in Chapter 3, a Si specimen with a thin SiO_2 layer of a 100 nm thickness was used as a reference material to estimate the sputtering rate, which was in turn used to calculate the thickness of the passive layer. Due to the high degree of roughness of the specimens and the different properties between the SiO_2 and passive layers, the thickness estimation from the XPS analysis could only be used as a qualitative value.

Figure 4.8 (a) shows the XPS depth file of the passive layer on a fresh SS316L specimen. From this result, it can be concluded that the passive layer formed in the ambient environment composed of an iron-rich outer layer and a Cr-rich inner layer, and Ni, Mo do not seem to participate in the air-formed oxide layer [129-131]. By using the half-height of O-oxide as the thickness measurement for the surface film, the layer requires around 2.6 min to sputter off the air-formed oxide layer on the surface of a fresh SS316L sample. After adopting the sputtering rate of 8.5 Å min^{-1} mentioned in Chapter 3, the thickness of the air-formed oxide layer is about 2.2 nm.

For the simulated cathode side of the HT-PEFC, the specimens underwent potentiostatic polarization at 0.65 V for 4 h, were bubbled with N_2 or O_2 in 85 wt.% H_3PO_4 at 130 °C, and then analyzed by XPS for the depth profiles of the passive layers formed during the potentiostatic tests, as shown in Figure 4.8 (b) and (c). The depth files in Figure 4.8 (b) and (c) are similar to each other but show a different trend in metal element distribution as compared with the fresh one. This indicates the passive layer formed inside the simulated cathode environment of the HT-PEFC had a different chemical composition and structure compared with the one formed in the ambient environment. The Fe element was significantly depleted from the outside layer surface in the passive layers formed in the simulated cathode environment of the HT-PEFC, leaving the Cr element as the dominant metal element in the outer surface layer. The trend of the elements distributions in the passive layer formed in the simulated cathode environment of the HT-PEFC with the N_2 and O_2 purged atmospheres are similar. Therefore, the explanation that the existence of the O_2 could react with the dissolved Cr elements and reform as chromium oxide, leading to the blocking effect on the passive layer, might be correct. The passive layer formed at the simulated cathodic side of the HT-PEFC is 1.3 nm thick in the N_2 purged environment and 1.1 nm in thickness in the O_2 purged environment following 4 h of potentiostatic polarization at 0.65 V.

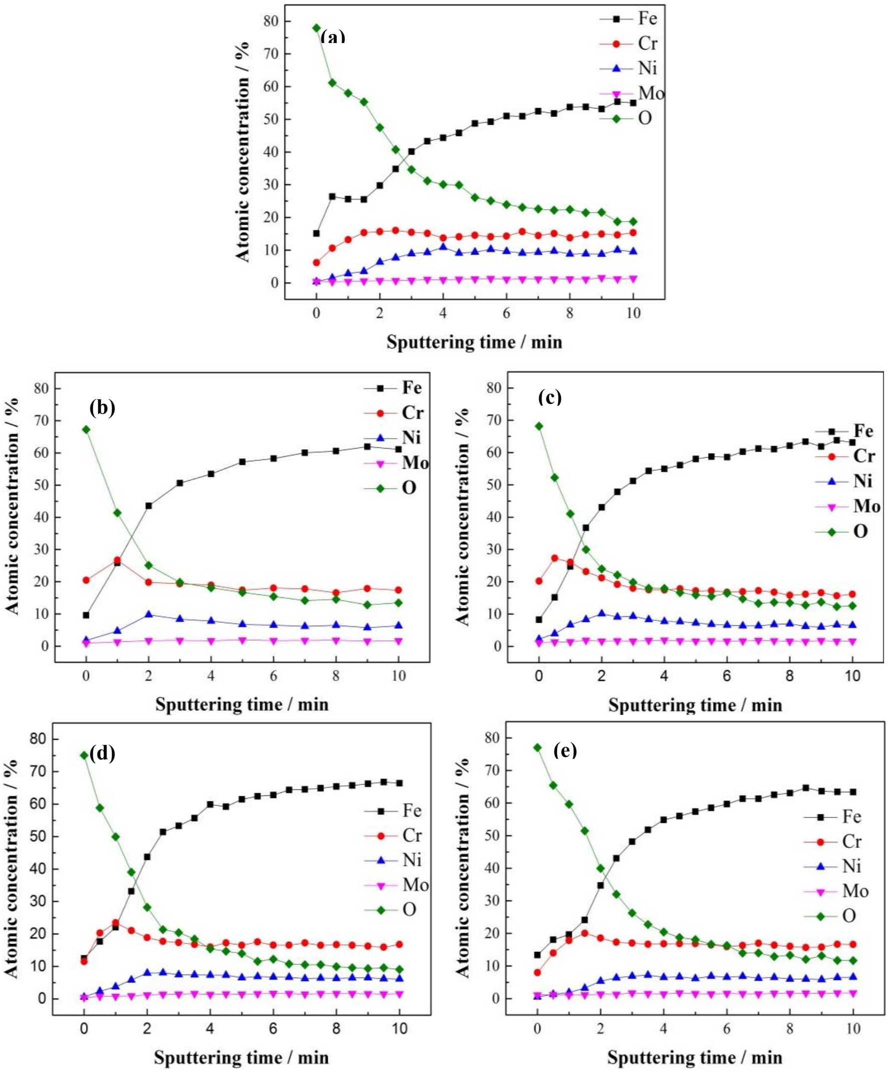

Figure 4.8. XPS depth profile of SS316L after potentiostatic corrosion in 85 wt.% H_3PO_4 at 130 °C: (a) fresh sample without corrosion; (b) sample after potentiostatic corrosion at 0.65 V, bubbled with N_2; (c) sample after potentiostatic corrosion at 0.65 V, bubbled with O_2; (d) sample after potentiostatic corrosion at 0.05 V, bubbled with H_2; (e) sample after potentiostatic corrosion at 0.05 V, bubbled with N_2 [8].

For the simulated anodic side of HT-PEFC, the specimens underwent potentiostatic polarization at 0.05 V for 4 h, were bubbled with H_2 or N_2 in 85 wt.% H_3PO_4 at 130 °C, and were then analyzed by XPS for the depth profiles of the specimen surfaces, as shown in Figure 4.8 (d) and (e). As discussed before, there was a charge of 0.05 V in the active region of corrosion; the region would not form a passive layer on the specimen surface during the potentiostatic tests.

However, a time interval occurred between removal of the applied potential and of the samples from the glass cell; the specimens would have been on free corrosion potential for several minutes, and a passive layer then formed under the free corrosion potential conditions in the 85 wt.% H_3PO_4 at 130 °C. Figure 4.8 shows that the distribution of the metal elements on the surface of the specimen following corrosion at the simulated anodic side of the HT-PEFC was similar to that of the fresh one, but had a higher Cr content. The passive layer so formed had an estimated thickness of 2.1 nm within the N_2 purged environment and 1.6 nm within the H_2 purged one.

4.8 Summary

The present chapter deals with the electrochemical corrosion behaviors of 316L stainless steel in the simulated HT-PEFC environment, and also investigates the influence of gases and electrode potentials on the corrosion. The following results were observed:

i. In a simulated HT-PEFC environment, the electrode potentials of HT-PEFC are the difference from the free corrosion potentials of SS316L. In a simulated cathodic environment, the electrode potential (0.65 V) is located in the passive region of corrosion for SS316L, while, for the simulated anodic environment, the electrode potential (0.05 V) is located in the active region of corrosion for SS316L. As a result, the corrosion current of the specimen in the simulated anodic side of the HT-PEFC is around 10 times higher than that at the simulated cathode.

ii. O_2, if present, can react with the dissolved Cr from the Cr-rich passive layer formed in the simulated cathodic environment of HT-PEFC. The reaction between the passive layer and O_2 gives a blocking effect on the elements of the passive layer, which results in the higher stability of the passive layer in a simulated HT-PEFC environment with an O_2 purged atmosphere.

iii. The passive layer formed inside the simulated cathodic environment of the HT-PEFC demonstrates good stability in hot phosphoric acid, especially with an O_2 purged atmosphere. The passive layer is a Cr-rich film, and has a thickness of nanometers.

These results give us some idea of the direction in which to look for a suitable coating to apply inside the HT-PEFC: it is suggested that the coating containing a high content of Cr might survive in the HT-PEFC. Therefore, the next chapter deals with the bilayer CrN/Cr coating in the simulated HT-PEFC environment, anticipating that this type of coating will perform well.

Chapter 5 An Electrochemical Corrosion Study of CrN/Cr Coated SS316L in Phosphoric Acid

From Chapter 4, it was established as not feasible to directly employ a bare metallic BPP for HT-PEFC applications due to the high corrosion rate of bare metallic materials within the HT-PEFC. To overcome this corrosion problem and further decrease the interfacial contact resistance while still retaining the benefits of using a metallic material, one possible solution considered involved in applying conduct and inert coating on metallic BPPs. The Cr-rich passive layer formed in the simulated cathodic environment of HT-PEFC shows high stability in hot phosphoric acid with an O_2 purged atmosphere. This provides a clue that a coating high in Cr might be suitable for the HT-PEFC applications. Due to this idea, a bilayer coating with an inner Cr and an outermost CrN layer fabricated by reactive magnetron sputtering was selected as the candidate for metallic BPPs coatings in HT-PEFCs. The relatively soft Cr layer was designed as an interlayer to enhance the connectivity and bonding strength between the outermost CrN layer and the substrate, while the metallic ceramic, CrN, was designed as an outermost layer to improve the interfacial conductivity and corrosion resistance. It is anticipated that the bilayer CrN/Cr coating might show good anti-corrosion properties in HT-PEFCs. The electrochemical behavior, including corrosion resistance and stability, as well as the surface conductivity of the bilayer CrN/Cr coating (deposited on a 0.1 mm thick SS316L substrate) was tested and evaluated in the simulated HT-PEFC environment. This work was published [132].

5.1 Coating characterizations

The crystal structure of the bilayer CrN/Cr coating was verified by XRD, as shown in Figure 5.1. In Figure 5.1, both γ-austenite and δ-ferrite are observed in the SS316L substrate. The existence of δ-ferrite in the austenite SS316L might be attributed to insufficient time being available for the δ→γ transformation during the annealing process following the cold rolling. Comparing the two XRD patterns in Figure 5.1, it can be seen that there are still some SS316L peaks for the coated specimen, as the penetration depth of the X-rays is higher than the thickness of the bilayer CrN/Cr coating (ca. 2 μm). The XRD spectra of the CrN/Cr coating reveals that it contains CrN, Cr_2N, and Cr. From Figure 5.1, it can also be seen that, except for the diffraction peaks from the substrate, the broad diffraction peak located in the position of 64° of 2Θ is the strongest, which might be due to the overlap of the three diffraction peaks of (220) CrN, (211)

Cr_2N and (200) Cr.

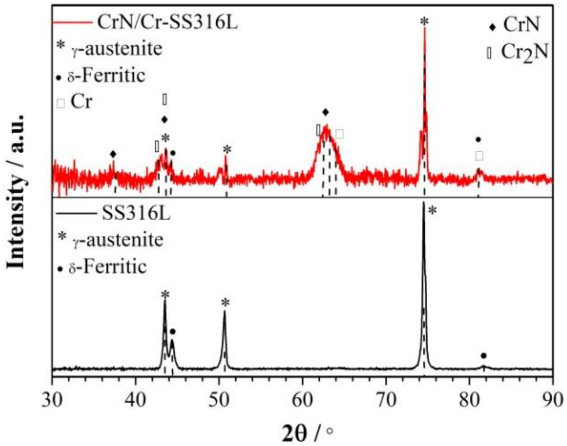

Figure 5.1. *XRD patterns on the bare SS316L and CrN/Cr coated SS316L [132].*

The surface and cross-sectional morphologies of the CrN/Cr coating on SS316L observed by SEM are shown in Figure 5.2. As can be seen from Figure 5.2(a), the surface of the CrN/Cr coating on the SS316L substrate is uniform, without any defects such as pinholes, and the CrN/Cr coating appears compact and dense. The CrN/Cr coating adheres well to the SS316L substrate with a thickness of ca. 2 μm, as is shown in Figure 5.2(b). Furthermore, the interface between the outer CrN and inner Cr layer can be observed.

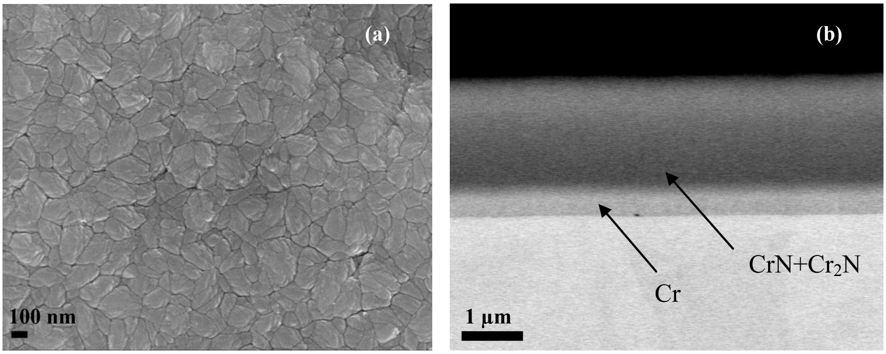

Figure 5.2. *SEM morphology of CrN/Cr coated SS316L: (a) surface, and (b) cross-section [132].*

5.2 Corrosion resistance and stability

Typically, the potentiodynamic polarization tests allow us to obtain the corrosion parameters of the subject, such as the corrosion potential and corrosion current density, in a specific environment. Figure 5.3 gives the potentiodynamic polarization curves as Tafel plots of the bare SS316L, and of the CrN/Cr coated SS316L specimens in a simulated HT-PEFC environment (85 wt. % H_3PO_4) at RT and 130 °C, respectively. The anodic polarization of the bare SS316L specimens begins at -0.5 V vs. RHE in order to eliminate the influence of the passive layer formed before the test. In contrast, the starting potentials for the CrN/Cr-coated SS316L specimens are much higher, i.e., at 0.1 V vs. OCV, in order to protect the coating from cathodic corrosion.

In contrast to the bare SS316L (as explained in Chapter 4), the E_{corr} of the CrN/Cr coated SS316L shifted markedly toward to a positive position, locating at 450 mV and 320 mV at RT and 130 °C, respectively. From a thermodynamic point of view, a higher E_{corr} indicates the possibility for better anti-corrosion properties [25, 33]. The i_{corr} of the CrN/Cr coated SS316L is only ca. 0.01 and 0.1 μA cm^2 at RT and 130 °C, respectively. Typically, the protection efficiency (P_i) of the coating is given by the following equation [133]:

$$P_i\ (\%) = 100 * (1-i_{corr}/i_{corr}^{0}) \qquad (5\text{-}1)$$

Here, i_{corr} and i_{corr}^0 represent the corrosion current densities of metallic BPPs in the simulated HT-PEFC environment with and without CrN/Cr coating, respectively. By calculating, the protection efficiency of the bilayer CrN/Cr coating approach 100 % under both RT and 130 °C, which indicates the superior corrosion resistance of the bilayer CrN/Cr coating in the simulated HT-PEFC environment.

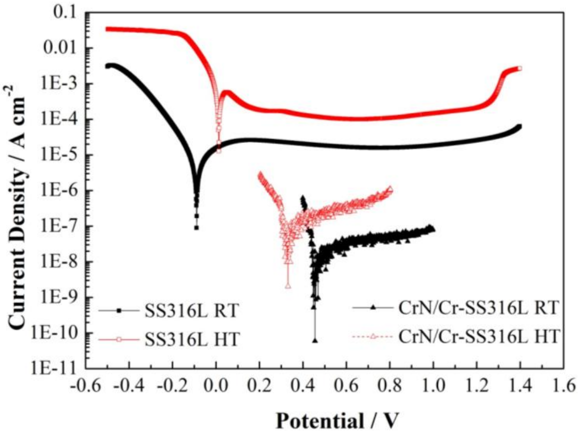

Figure 5.3. *Potentiodynamic polarization curves for bare and CrN/Cr coated SS316L, measured in 85 wt. %* H_3PO_4*, at RT and 130 °C [132].*

Table 5.1. *Corrosion parameters for bare and CrN/Cr coated SS316L, measured in simulated HT-PEFC environments [132].*

Samples	**E_{cor}(mV) / RT**	**I_{cor} (μA cm^{-2})/ RT**	**E_{corr}(mV) / 130°C**	**I_{cor} (μA cm^{-2})/ 130°C**
SS316L	-75	17.7	-20	141.9
CrN/Cr-SS316L	450	0.01	320	0.1

As explained in Chapter 3, the fuel cell's potential is about 0.6 V under typical operating conditions, which results in electrode potentials of roughly 0.65 V at the cathode side and 0.05 V at the anode side. In order to study the corrosion properties and stability of the CrN/Cr coating in the actual operating conditions of the HT-PEFC, the related potentiostatic tests were conducted for 4 h in an 85 wt.% H_3PO_4 solution at 130 °C, as shown in Figure 5.4. Figure 5.4(a) gives the potentiostatic polarization curves of bare and coated specimens in the simulated environment of an HT-PEFC, while Figure 5.4(b) gives the enlargement of the potentiostatic curves of coated specimens in both the cathodic and anodic environments of the HT-PEFC. Both cases in the simulated cathodic environment of HT-PFC show a very fast current density decay at the beginning due to the formation of a passive film, and its gradual stabilization at a relatively low level. For the case of the bare SS316L, the current density finally stabilizes at ca. 6 μA cm^2, which is about 6 times higher than the requirement for DOE (less than 1 μA cm^2). By contrast, the current density of the CrN/Cr coated SS316L is much lower and more stable through the entire test. The stable current density of the CrN/Cr-coated SS316L is less than 0.01 μA cm^2 in the simulated cathodic environment of HT-PEFC, a reduction of over 600 times in magnitude compared with that of the bare SS316L. The potentiostatic curves for the bare SS316L and CrN/Cr coated SS316L tested in the simulated anodic environment of HT-PEFC are also shown in Figure 5.4(a). In the cases of the simulated anodic environment of HT-PEFC, the potentiostatic curve of the bare SS316L also shows an initial trend of current density decay in the beginning, while it finally stabilizes at ca. 60 μA cm^2; it is about 10 times higher than that of the cathode side. In sharp contrast, for the case of the CrN/Cr-coated SS316L, a stable but negative current density (ca. -1.0 μA cm^2) is shown within the potentiostatic test in the simulated anodic HT-PEFC environment. Through the mixed potential theory [54], this negative current density means that the cathodic reaction (the reduction of H^+) predominates under the potential of the simulated anodic environment of an HT-PEFC, where the reactions involving the dissolution of the coating or substrate are significantly suppressed, which results in cathodic protection to the CrN/Cr coating.

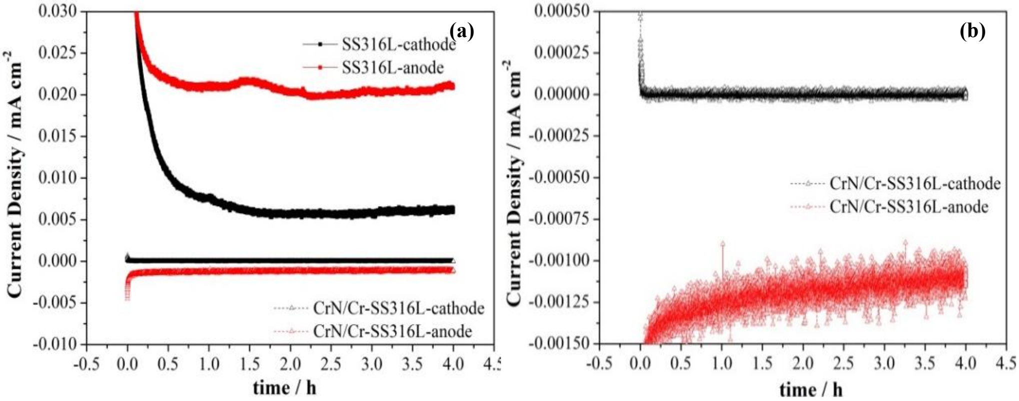

Figure 5.4. *Current density-time curves of bare and CrN/Cr coated SS316L tested in simulated HT-PEFC environments: (a) cathodic, and (b) anodic [132].*

The SEM morphology of the CrN/Cr-coated SS316L following the potentiostatic tests in the simulated cathodic and anodic HT-PEFC environments (as shown in Figure 5.5) shows almost no difference compared to the non-corroded one, which indicates the superior corrosion resistance and durability of the CrN/Cr coating on both the simulated anodic and cathodic sides of the HT-PEFC environments.

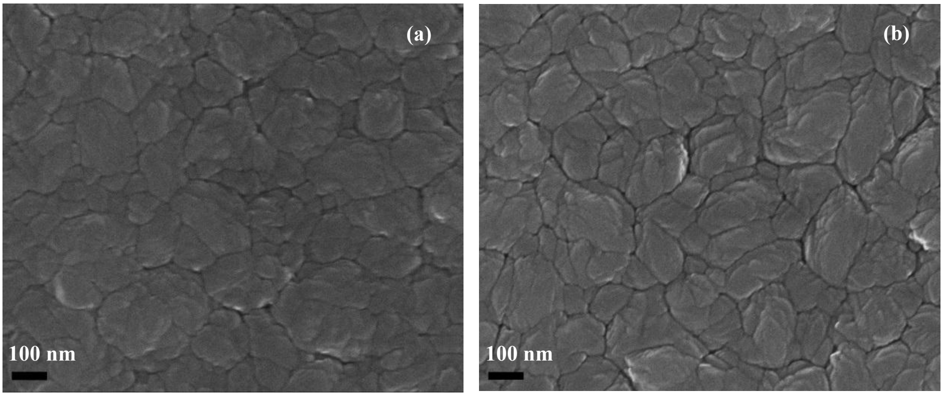

Figure 5.5. *The surface morphology of CrN/Cr coated SS316L following potentiostatic tests in the simulated anodic and cathodic environments of the HT-PEFC: (a) anodic, and (b) cathodic [132].*

5.3 Electrochemical impedance spectroscopy

By merely applying a small amplitude signal to the electrochemical system, the EIS can measure the depth mechanism of the electrochemical behavior of electrodes under certain conditions. The EIS spectra for the bare and CrN/Cr-coated SS316L specimens measured in 85 wt. % H_3PO_4 at 130 °C are shown in Figure 5.6. From the Nyquist plots (as shown in Figure 5.6(a)), it is observed that the bare SS316L possesses two depressed semicircles in the high- and low-frequency range, respectively. The Bode plot for the bare SS316L (as shown in Figure 5.6(b)) displays two peaks, indicating two-time constants. From our previous research (Chapter 4) on the bare SS316L in a simulated HT-PEFC environment, a passive layer is formed on the surface of the SS316L substrate in a simulated HT-PEFC environment that mainly contains Fe- and Cr-oxides [134]. In the aggressive corrosion environment of hot phosphoric acid, the passive layers might be (partially) destroyed, causing the electrolyte to pass through the destroyed area of the passive layer and be partially in direct contact with the substrate, resulting in a two-time constant being represented on the Bode plot. In contrast to the bare SS316L specimen, the Nyquist plot for the CrN/Cr coated SS316L shows only one depressed semicircle within the test frequency range. Also, log$|Z|$ changes linearly with log f in a large frequency range from 0.01 Hz to 1000 Hz, indicating a predominantly capacitive behavior [33]. This phenomenon suggests that the bilayer CrN/Cr coating must be electrochemically-isolated and have a large resistance and low capacitance.

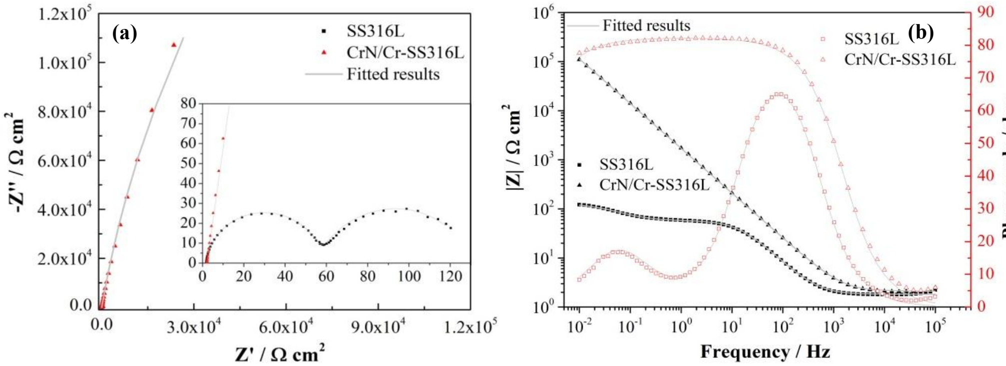

Figure 5.6. *EIS spectra for the bare and CrN/Cr coated SS316L specimens in 85 wt. % H_3PO_4 at 130 °C: (a) Nyquist plots, and (b) Bode plots [132].*

Based on the above discussion, the equivalent circuit for the bare SS316L specimen is R(C[R(CR)]) and includes two-time constants, while the equivalent circuit for the CrN/Cr-coated SS316L specimen is R(CR), as shown in Figure 5.7. R_s is the solution resistance between the working and reference electrodes. R_{pore} and C_{pore} are the resistance and capacitance of the coating or passive layer via defects, respectively [135]. R_{ct} is the charge transfer resistance, and C_{dl} the double layer capacitance of the substrate at the defects which provides information on the charge separation and polarity of the electrolyte/substrate interface [34, 135]. Usually, constant phase elements (CPEs) are used rather than pure capacitance are used to fit the spectra when the non-ideal capacitive response (depressed semicircle) of the double layer appears [33, 136].

The fitted results are listed in Table 5.2. The R_{ct} of the CrN/Cr coated SS316L is 1.1×10^6 Ω cm^2, i.e., more than four orders of magnitude higher than that of bare SS316L (73.8 Ω cm^2). The high R_{ct} of the CrN/Cr coating confirms the superior anti-corrosion properties of the CrN/Cr coatings in the simulated HT-PEFC environments and results in a much lower corrosion rate for the CrN/Cr-coated SS316L specimen as compared with that of the bare SS316L specimen.

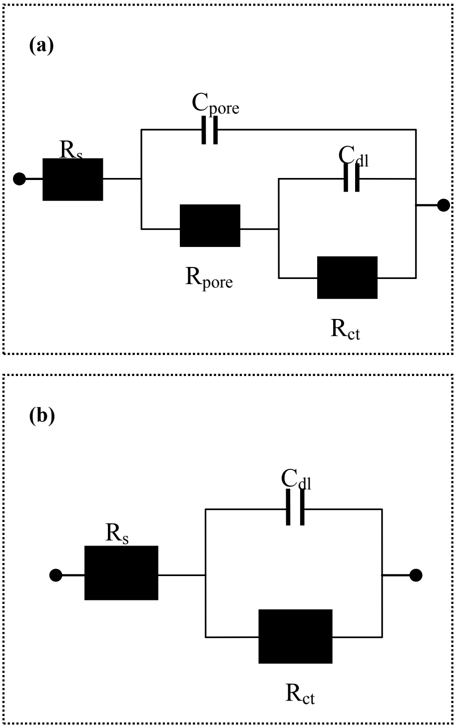

Figure 5.7. *Equivalent circuits for bare and CrN/Cr coated SS316L specimens: (a) SS316L (b) CrN/Cr coated SS316L [132].*

Table 5.2. *Fitted results for EIS spectra for the bare and CrN/Cr coated SS316L [132].*

samples	**Circuit Model**	**R_s (Ω cm^2)**	**C_{dl} ($Ω^{-1}$ cm^{-2} s^n)**	**R_c (Ω cm^2)**	**n_{dl} (-)**	**C_{pore}($Ω^{-1}$ cm^{-2} s^n)**	**n_{pore} (-)**	**R_{pore}(Ω cm^2)**
SS316L	Figure 8(a)	1.826	$4.616*10^{-2}$	73.076	0.808	$2.844*10^{-4}$	0.942	55.677
CrN/Cr-SS316L	Figure 8(b)	2.069	$1.088*10^{-4}$	$1.1*10^6$	0.914	/	/	/

5.4 Interfacial contact resistance

The interfacial contact resistance (ICR) between the BPPs and the GDLs is of significant importance for the lifetime and performance of a fuel cell. The ICR values, as a function of compaction force, for the CrN/Cr-coated SS316L samples before and after the potentiostatic tests are investigated, as shown in Figure 5.8, with bare SS316L as the reference.

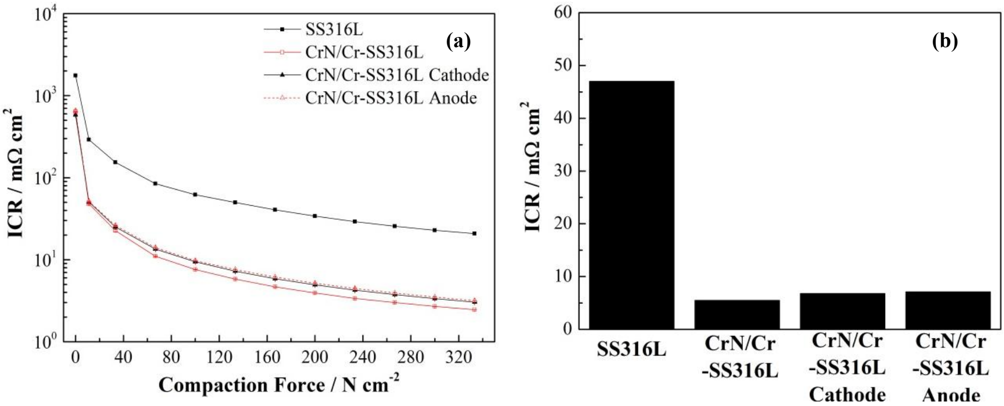

Figure 5.8. *ICR of CrN/Cr-coated SS316L samples before and after polarization tests in the simulated environment, as well as bare SS316L: (a) under different compaction pressures, and (b) under 140 N cm*$^{-2}$ *[132].*

It is observed that the ICR values are reduced with an increasing compaction force for all cases, which is due to the increase in the effective contact area as the clamping pressure increases [137]. The ICR values of the CrN/Cr-coated SS316L is almost one order of magnitude lower than that of the bare SS316L over the entire compressing force. Under the compaction force of 140 N cm^{-2}, which is the normal assembly force for fuel cell stacks (as shown in Figure 5.8(b)), the ICR values for the bare and CrN/Cr coated SS316L specimens are ca. 47 and 5.5 mΩ cm^2, respectively. The apparently lower ICR value for the CrN/Cr coated SS316L stems from the relatively higher electrical conductivity of the outer CrN layer, because transition metal nitrides such as CrN or TiN are metallic ceramics with good electrical conductivity [128, 138]. After the 4h potentiostatic tests under the simulated cathodic and anodic environments of the HT-PEFC, the ICRs of CrN/Cr coated specimens achieved show a slight increase (increased from ca. 5.5 to ca. 7 mΩ cm^2), while the final ICR values following the corrosion tests in the simulated HT-PEFC environment were still able to satisfy the requirements for DOE (i.e., less than 10 mΩ cm^2 under a force of 140 N cm^{-2}). Combining the SEM results before and after the corrosion tests and also the electrochemical performance of the CrN/Cr coating in a simulated HT-PEFC environment, it was concluded that the BPPs with the bilayer CrN/Cr coating provided excellent stability for HT-PEFC applications.

5.5 Summary

A bilayer CrN/Cr coating was successfully deposited on an SS316L substrate (0.1 mm-thick) using a reactive magnetron sputtering method with a thickness of ca. 2 μm. The materials are chosen including the substrate and coating, and the methods and equipment for the coating fabrication were all suitable for mass production. XRD analysis and SEM observation show that the bilayer CrN/Cr coating consists of CrN, Cr_2N and Cr phases with a dense, continuous and defect-free nanocrystal structure. The results for the electrochemical tests indicate that the bilayer CrN/Cr coating displays excellent corrosion resistance in the simulated HT-PEFC environments. The corrosion current densities for the bilayer CrN/Cr-coated SS316L specimens are ca. 0.01 μA cm^{-2} at RT and 0.1 μA cm^{-2} at 130 °C, respectively, in the simulated HT-PEFC environment. The current densities of the CrN/Cr-coated SS316L specimens are, respectively, ca. 0.01 μA cm^{-2} and -1.0 μA cm^{-2} on the cathodic and anodic sides of the HT-PEFC under normal working conditions. The ICR values of the bilayer CrN/Cr-coated SS316L specimens are less than 10 mΩ cm^2, both before or after the corrosion tests. The superb corrosion resistance and conductivity of the CrN/Cr-coated SS316L in the simulated HT-PEFC environment indicate that the low-cost metallic BPPs fabricated by a CrN/Cr-coated SS316L (0.1 mm thick) would be suitable for the application of HT-PEFCs.

Due to the severe dynamic vibration environments in the application of mobility, such as mobile cars and airplanes, the micro-defects on the ceramic coatings will be formed which have highly influence on the long-time running performance of coatings. Also, for the mass production of ceramic coatings by PVD methods, the defects (such as pinholes or cracks) on the surface are inevitable. Therefore, the resistance of coatings to these micro-defects is very important for the longtime application in fuel cells. The electrochemical behavior of CrN/Cr coatings with artificially created defects in a simulated cathodic HT-PEFC environment are investigated in the next chapter.

Chapter 6 The Influence of Oxygen on the Electrochemical Behaviour of CrN/Cr Coating with Artificially Induced Defects on SS316L in the Simulated Cathodic Environment of an HT-PEFC

Chapter 5 demonstrates that the bilayer CrN/Cr coating shows superior anti-corrosion performance in the simulated HT-PEFC environment. It is likewise found that, in the application of fuel cells during mobility, the vibrational environment might cause some cracks on the surface of the ceramic coatings. It is not possible to eliminate the defects such as pinholes on the surfaces of coatings fabricated by PVD. The existence of defects will act as an electrolyte pathway directly contact with the substrate for coatings lacking self-healing ability. Therefore, localized corrosion is expected to occur at the damaged site. The oxidation of the metallic component within a film can seal the flaws in the film, such that a self-healing ability can be introduced into the film by adding a metallic component [35]. Therefore, except for the aim of increasing the connections between the CrN layer and the substrate, it is also expected that the inner Cr layer can offer some self-healing ability for the bilayer CrN/Cr coating when defects appeared on its surface.

Regarding these concepts, this chapter evaluates the performance of CrN/Cr coating with artificially induced defects in the simulated HT-PEFC environment. By purging different gases (i.e., N_2 and O_2) into the electrolyte, it was possible to investigate the influence of gases on the electrochemical behavior of CrN/Cr coatings with artificially created defects in the simulated HT-PEFC environment was also investigated. This work has already been previously published [29] [139].

6.1 Coating characterizations

In order to fabricate the CrN/Cr coated SS316L specimens with artificially induced defects, firstly, the SS316L substrates were firstly polished by hand with SiC paper to form deep grooves on the surface of the substrate, and then bilayer CrN/Cr coatings were deposited on the polished substrate. The surface morphology of the CrN/Cr coated SS316L (with its artificially polished surface) were revealed in Figure 6.1(a), from which it could be recognized that some scratches in the form of artificially produced defects resembled the polished grooves appearing on the surface of the CrN/Cr coating. The cross-section of the coated specimen is shown in Figure 6.1(b), illustrating the ruptures are crossing the entire height of the coating, and also some delamination also appeared between the coating and substrate. The artificially induced defects successfully formed on the coating were the result of the harsh, pre-polishing operation on the substrate prior to the coating deposition.

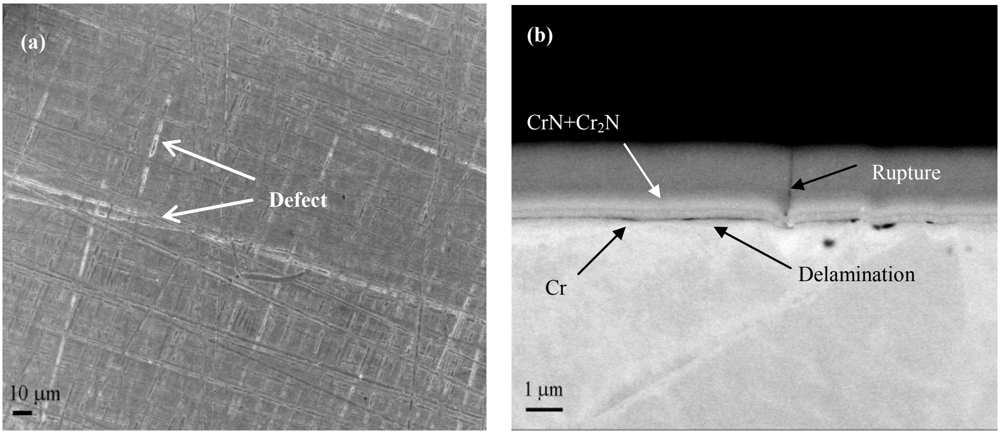

Figure 6.1. The SEM morphology of a CrN/Cr coated SS316L specimen with artificially created defects: (a) surface morphology, and (b) cross-section [139].

6.2 Potentiodynamic polarization tests

Potentiodynamic polarization curves were conducted to establish general corrosion parameters for the CrN/Cr coated SS316L specimens with artificially produced defects at RT and 130 ºC in 85 wt.% H_3PO_4, purged with different gases (N_2 and O_2), as shown in Figure 6.2. Chapter 4 shows that the oxygen can increase the stability of the passive layer formed in the simulated cathodic environment of the HT-PEFC, a Cr-rich film. Therefore, it was anticipated that the presence of oxygen would also alter the corrosion behavior of the CrN/Cr coating. After stabilizing the sample at RT for 30 min, potentiodynamic polarization curves were conducted. Following this, the cell was heated to 130 °C at a heating rate of 1 ºC min^{-1}. After remaining at 130 °C for 30 min, the potentiodynamic polarization curves of the specimens at 130 ºC were conducted once again. All potentiodynamic polarization tests of coated specimens in this chapter were conducted beginning in the anodic direction at -100 mV vs. OCV with a scan rate of 5 mV s^{-1}. The obtained corrosion parameters for the CrN/Cr coated SS316L in all environments with its artificially instigated defects are given in Table 6.1. The protection efficiency (P_i) of the coating was calculated using the following Equation 5-1 [133], and the protective efficiency (P_i) of the

CrN/Cr coating with artificially induced defects was calculated, as shown in Table 6.1.

Table 6.1. *The Corrosion properties of the bare and CrN/Cr-coated SS316L with artificially created defects determined from the polarization curves [139].*

Sample	Environment	E_{corr} (mV)	i_{corr} (µA cm^{-2})	Protective efficiency (%)
Bare SS316L	N_2 @ RT	-75	19	\
Bare SS316L	O_2 @ RT	-77	18	\
Coated SS316L	N_2 @ RT	126	0.03	~99.8
Coated SS316L	O_2 @ RT	121	0.03	~99.8
Bare SS316L	N_2 @ 130 °C	-21	157	\
Bare SS316L	O_2 @ 130 °C	-22	155	\
Coated SS316L	N_2 @ 130 °C	-3	7	~95
Coated SS316L	O_2 @ 130 °C	248	1	~99

From Figure 6.2(a), it could be seen that, at RT, the corrosion potentials of the CrN/Cr coated SS316L with artificially produced defects was ca. 120 mV in both the gases, which is lower than that of the CrN/Cr coated SS316L lacking in artificially created defects, as shown in Chapter 5. The corrosion current densities of the coated specimens with artificial defects are still ca. 0.03 µA cm^{-2} at RT, only being a slightly increase as the case in Chapter 5 without artificially induced defects. At RT, the corrosion environment for concentrated phosphoric acid was moderate, and even though the artificially created defects had decreased the E_{corr} of the coated specimens, indicating their lower anti-corrosion ability, the corrosion rates for the coated specimens with artificially induced defects only slightly changed.

At 130 °C, the corrosion potential of the CrN/Cr coated specimens with artificially induced defects in the N_2 atmosphere showed a shift in the negative direction as compared with that at RT, as shown in Figure 6.2(b). Conversely, the corrosion potential of the CrN/Cr coated specimen with artificially created defects in the O_2 atmosphere, showed a positive shift compared with that at RT. The corrosion current density of the coated specimens with artificially induced defects in the N_2 purged environment at 130 °C was ca. 7 µA cm^{-2}, even though it also demonstrated a degree of protective efficiency on the substrate, but the corrosion current density had increased 50 times compared with the one without defects. In contrast, the corrosion current density of the coated specimen in the O_2 purged environment was only ca. 1 µA cm^{-2}. These behaviors indicated that oxygen could enhance the anti-corrosion capability of the CrN/Cr coating with artificially induced defects in hot phosphoric acid. As mentioned in Chapter 4, the existence of O_2 could enhance the stability of a Cr-rich layer due to the reactions between O_2 and dissolved Cr.

Therefore, in the case of the coated specimens in this research, it is assumed that O_2 would react with the Cr released from the coating and form a highly stable passive layer at the damaged site of the coating, which could then resist further corrosion from the electrolyte. Conversely, in the N_2 atmosphere, the Cr elements at the damaged sites dissolved more slowly. As a result, localized corrosion occurred at the damaged site.

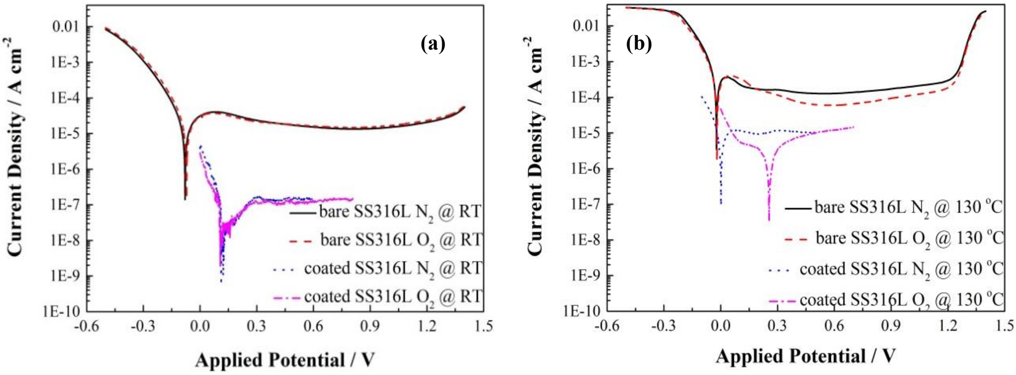

Figure 6.2. *Potentiodynamic polarization curves of the bare and coated specimens with artificially created defects in 85 wt.%* H_3PO_4 *at a scan rate of 5 mV* s^{-1}. *(a) RT. (b) 130 °C [139].*

6.3 The stability of the CrN/Cr coating with artificially induced defects in the simulated cathodic environment of the HT-PEFC

In order to evaluate the stability of the CrN/Cr coated SS316L specimens with artificially produced defects in the simulated cathodic side of the HT-PEFC; the operating conditions of 0.65 V vs. RHE were applied to the specimens with an N_2 or O_2 purged atmosphere for 4 h under 85 wt. % H_3PO_4, at 130 °C, followed by recording being made of the potential decay following the potentiostatic tests. The decay of the E_{corr} after the potentiostatic operation was able to reflect the stability of the passive layers formed at the damaged sites during the potentiostatic operation, and of the coating itself. The processes of the free corrosion potential changed after the potentiostatic tests were recorded and shown in Figure 6.3.

In the N_2 purged environment, the E_{corr} slowly decreased from ca. 0.45 V to ca. -20 mV over a relatively long period (more than 1 h) after removing the applied potential of 0.65 V. The firstly rapid decay of the E_{corr} was since the removal of the applied potential allowed the potential to move quickly to the specimen's free corrosion potential under that status. The slow decay of the free corrosion potential subsequently indicated the slow depletion of the passive layer formed during the potentiostatic test, and since the free corrosion potential at this stage remained located in the passive region of the SS316L corrosion, the exposure area of the coating returned to passivity, slowing the decay rate. When the free corrosion potential of the coated specimen reached around 0.15 V, the decay rate of the free corrosion potential again accelerated. This was mainly due to the fact that a potential of less than 0.15 V was located in the active region of the SS316L corrosion, which would not reform a passive layer again on the damaged site; this finally resulted in the more rapid decay of the free corrosion potential. Finally, in this case, the free corrosion potential of the coated specimen stabilized at ca. -20 mV. This phenomenon indicates that even though the exposure area of the substrate before the potentiostatic test could reach passivity again during the potentiostatic test in the simulated cathodic environment of HT-PEFC, the formed passive layer was unable to survive in the hot phosphoric acid and totally depleted within 2 h. In contrast, for the O_2 purged environment, the E_{corr} of the coated specimen after potentiostatic polarization tests remained stable at ca. 0.4 V over a very lengthy period (over 2 h) which indicated the very high stability of the coating with artificial defects in the simulated cathodic environment of an HT-PEFC with an O_2 purged atmosphere. This result showed good consistency with the result of Chapter 4's mention that a passive layer formed in the O_2 purged atmosphere can tolerate the harsh environment of hot phosphoric acid, which could decrease the chance and level of localized corrosion in the damaged sites.

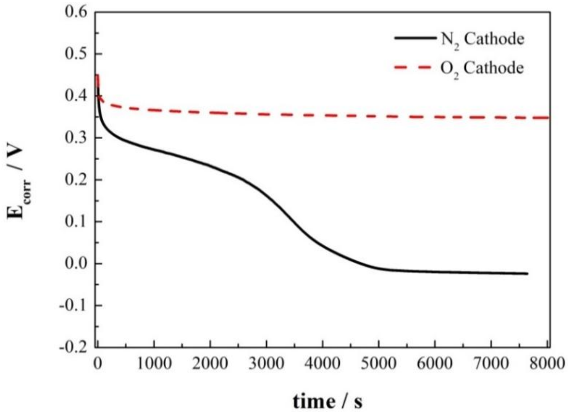

Figure 6.3. *The potential decay of the CrN/Cr coated SS316L with artificially produced defects after the potentiostatic tests in 85 wt.% H_3PO_4, following the potentiostatic operation at 0.65 V, and bubbled with N_2 or O_2 [29].*

After the potentiostatic tests and while waiting for the E_{corr} to restablize, the potentiodynamic polarization tests were conducted once again in order to evaluate the degree of degradation in the coating during these processes, as shown in Figure 6.4. The related corrosion parameters obtained from these potentiodynamic curves are shown in Table 6.2.

Table 6.2. *The corrosion properties of CrN/Cr-coated SS316L, determined from the polarization curve following the potentiostatic operation [139].*

Sample	**Environment**	**E_{corr} (mV)**	**i_{corr} (µA cm^{-2})**
Coated SS316L	N_2 Cathode	-29	86
Coated SS316L	O_2 Cathode	229	1

For the simulated cathodic environment of the HT-PEFC with an N_2 purged atmosphere, the corrosion current density of the CrN/Cr coated specimen with artificially instigated defects was ca. 86 µA cm^{-2} following the potentiostatic test and OCV recording operation, which is roughly 16 times higher than that before the potentiostatic test. This apparent increase in the corrosion current density indicates the harsh degradation of the CrN/Cr coating with artificially induced defects during these processes in the simulated cathodic environment of the HT-PEFC with the N_2 purged atmosphere. Conversely, for the simulated cathode environment of HT-PEFC with an O_2 purged atmosphere, the corrosion current density of the specimen remained at ca. 1 µA cm^{-2} following this corrosion operation, which is the same value as before. This behavior reflects the high stability of the CrN/Cr coating with artificial defects in the simulated cathodic side of the HT-PEFC with an O_2 purged atmosphere.

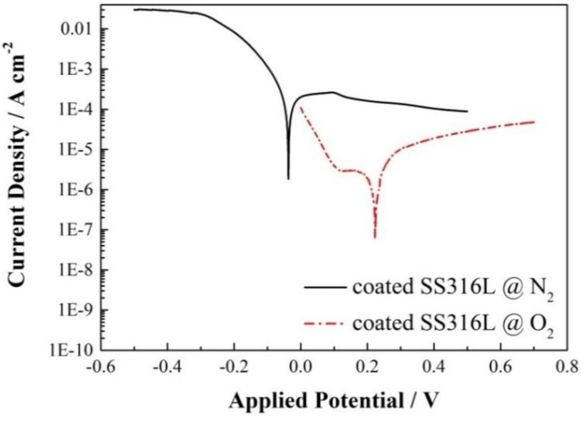

Figure 6.4. *Potentiodynamic polarization curves following potentiostatic operations of the CrN/Cr-coated SS316L with artificially induced defects, in 85 wt.% H_3PO_4 and at a scan rate of 5 mV s^{-1} at 130 °C [139].*

6.4 SEM after corrosion tests

After all the corrosion tests, the surface morphologies of the coated specimens were characterized by SEM, as shown in Figure 6.5.

Figure 6.5 (a) and (b) give the surface morphologies of the CrN/Cr coated SS316L specimens with artificially created defects following the corrosion tests in the simulated cathode environments of HT-PEFCs with N_2 and O_2 purged atmospheres, respectively. For the simulated cathode side of HT-PEFC with the N_2 atmosphere, the CrN/Cr coating had broken down following the corrosion tests. Conversely, for the simulated cathode environment of the HT-PEFC with an O_2 atmosphere, the CrN/Cr coating retained integrity after the corrosion tests. In order to clarify the mechanisms of the two different corrosion behaviors in the CrN/Cr coated SS316L specimens with artificially induced defects in the simulated cathodic environments of HT-PEFCs with N_2 or O_2 purged atmospheres, the EIS measurements were conducted under OCV conditions and at 0.65 V, and the results are shown and analyzed in the next section.

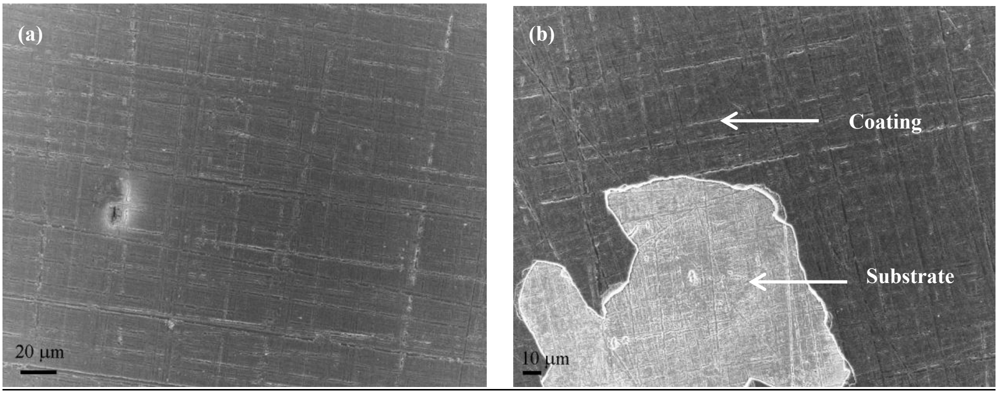

__Figure 6.5.__ Surface morphologies following the corrosion tests on the CrN/Cr coated SS316L with artificially produced defects in 85 wt.% H_3PO_4 purged with N_2 or O_2 at 130 °C. (a) after the corrosion test in the simulated cathode environment with an O_2 atmosphere. (b) after the corrosion test in the simulated cathode environment with an N_2 atmosphere [139].

6.5 Electrochemical impedance spectroscopy

EIS measurements were applied to clarify the mechanisms of the diverse behaviors of the CrN/Cr coated SS316L specimens with artificially induced defects in the simulated cathodic environments of HT-PEFCs with an N_2 and O_2 purged atmospheres. Figure 6.6 illustrates the EIS spectra of the CrN/Cr coated SS316L specimens with artificially created defects under OCV conditions (the change in OCV being less than 1 mV every 300 s) before and after corrosion tests in the simulated cathodic environments of HT-PEFCs with an N_2 or O_2 purged atmospheres and in the reference one of bare SS316L. From Figure 6.6, it could be observed that the Nyquist plots for the CrN/Cr coated SS316L specimen with artificial defects in the O_2 atmosphere and for the bare SS316L in both N_2 and O_2 atmospheres displayed two depressed semicircles in the high and low-frequency levels, respectively. Relative to the Nyquist plots, the Bode plots for these cases also showed two-time constants. According to the above analysis, an equivalent circuit, as shown in Figure 6.7(b), is established to fit the impedance spectra of these cases. This equivalent circuit consists of different electrical elements assembled to describe the electrochemical behaviors, where R_s represents the solution resistance which existed between the reference electrode and the working electrode. R_{pore} and C_{pore} are used to describe the electrochemical behavior of the coating or the passive layer via the defects; comparatively, the substrate polarization resistance and capacitance (R_{ct} and C_{dl}) depict the behavior of the substrate at the defect areas. Constant phase element (CPE) is used to replace the C_{dl} and C_{pore} to fit the spectra, owing to the non-ideal capacitive response of the double layer and coating (or passive layer).

In the case of the CrN/Cr coated SS316L with artificially induced defects in the N_2 purged atmosphere, the Nyquist plots also showed a Warburg diffusion tail in the low-frequency zone. The Warburg element implied a diffusion-controlled electrochemical system. As a result, a Warburg element was added into the equivalent circuit to fit it into the impedance spectra of the CrN/Cr coated SS316L with artificially induced defects in the simulated cathodic environment of the HT-PEFC with an N_2 purged atmosphere, as shown in Figure 6.7(a).

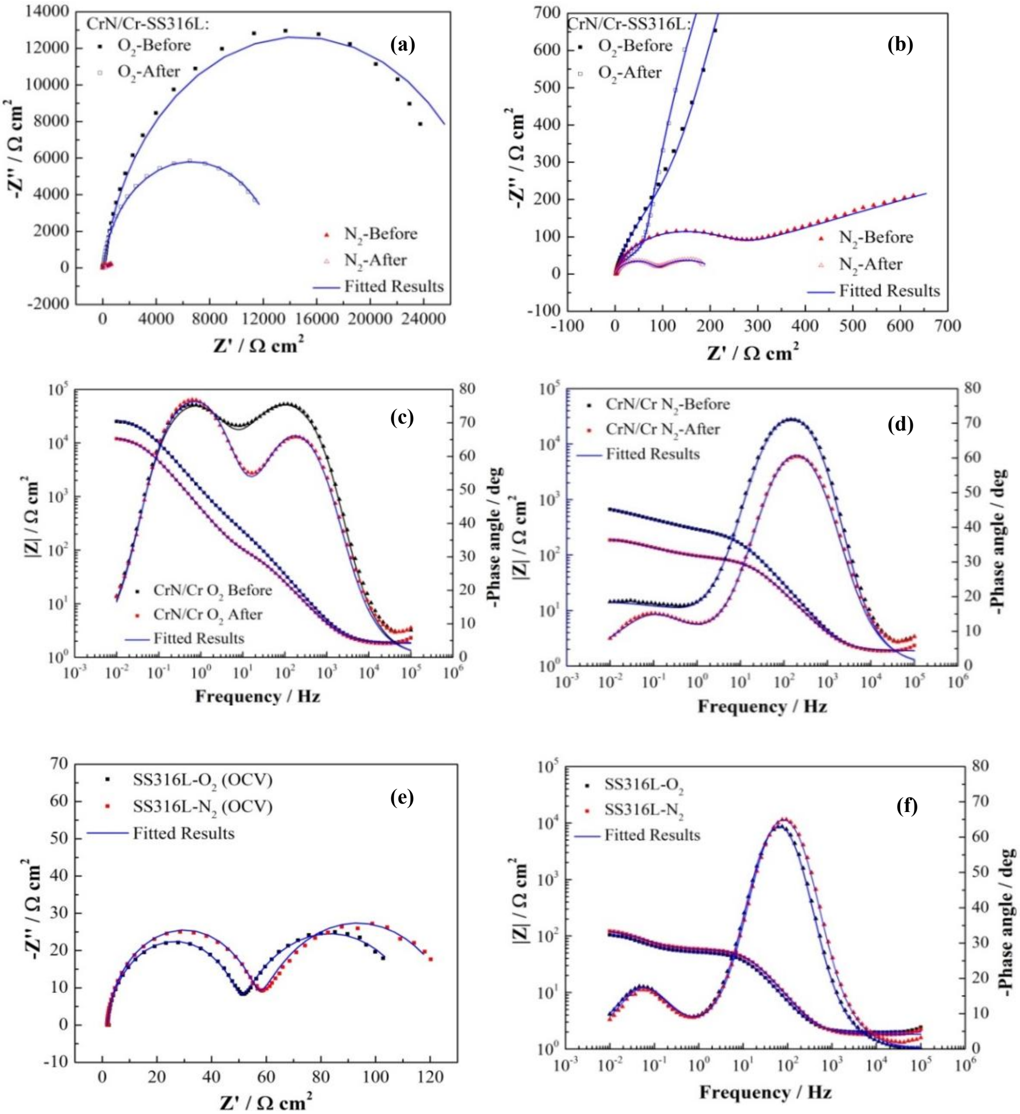

Figure 6.6. *The EIS spectra of the CrN/Cr coated SS316L with artificially instigated defects under OCV conditions in the 85 wt.% H_3PO_4, at 130 °C purged with N_2 and O_2 and combined with the bare SS316L sample: (a) Nyquist plots of the CrN/Cr coated SS316L specimens with artificial defects before and after the corrosion tests; (b) enlarged depiction of Nyquist plots in N_2 purged atmosphere; (c) Bode plots of the CrN/Cr coated SS316L specimens with artificial defects before and after the corrosion tests in the O_2 purged atmosphere; (d) Bode plots of the CrN/Cr coated SS316L specimens with artificially produced defects before and after the corrosion tests in the N_2 purged atmosphere; (e) Nyquist plots of the bare SS316L specimens in the N_2 and O_2 purged atmosphere; (f) Bode plots of the bare SS316L specimens in the N_2 and O_2 purged atmosphere [139].*

As explained in Chapter 5, when stainless steels are exposed to the corrosive acid electrolyte, a passive layer will form on the surface [33, 119]. The passive layer can be destroyed by a harsh corrosion environment which results in a discontinuous passive film where the electrolyte can pass through and contact the passive film/stainless steel interface directly [140]. Therefore, two-time constants appeared on the spectra of bare SS316L specimens in the simulated HT-PEFC environment with both N_2 and O_2 purged atmospheres. The EIS spectra of the bare SS316L specimens in the simulated HT-PEFC environment with both N_2 and O_2 purged atmosphere were similar, as shown in Figure 6.6 (e) and (f). This corresponds with other similar electrochemical behaviors of bare SS316L specimens in the simulated HT-PEFC environment with an N_2 and O_2 purged atmospheres, as shown in Chapter 4. But the resistance of the bare SS316L in the N_2 purged atmosphere is relatively higher than that in the O_2 purged atmosphere, which indicates the relatively higher protective effect of the passive layer formed in the N_2 atmosphere under OCV conditions than that of the O_2. This phenomenon corresponds with the results in Chapter 4, in which the OCV value for bare SS316L in 85 wt. % H_3PO_4 at 130 °C with an N2 purged atmosphere is higher than that of O_2.

For the case of the CrN/Cr coated SS316L specimen with artificial defects in the simulated HT-PEFC environment with the O_2 purged atmosphere, two-time constants appeared on its EIS spectra both before and after corrosion tests under OCV conditions, as shown in Figure 6.6 (a) and (c). The one appearing at high frequency represents the dielectric characteristics of the coating, while the one at low frequency corresponds to the substrate in the pores [34]. After comparing these results with those of the bare sample, the charge transfer resistance of the substrate at defects of the CrN/Cr coated SS316L specimen’s region of defect in the simulated HT-PEFC environment with an O_2 purged atmosphere are ca. 400 times higher, which indicates the passive layer in the damaged sites under OCV conditions demonstrates superior anti-corrosive properties. After the corrosion tests, the peak height of the coating decreased, which indicates that the response becomes less capacitive; the decreased capacitance might be due to the increasing defects on the coating surface [34]. However, the peak heights of the substrate show almost no change before and after corrosion tests. This phenomenon indicates that the property of the passive layer formed on the damaged sites show less change before and after the corrosion tests, even in cases whereby the damaged areas of the coating worsened following the corrosion tests. Following the corrosion tests, the charge transfer resistance of the substrate at the damaged sites of the CrN/Cr coating in the simulated HT-PEFC with an O_2 purged atmosphere is still ca. 200 times higher than that of the bare one.

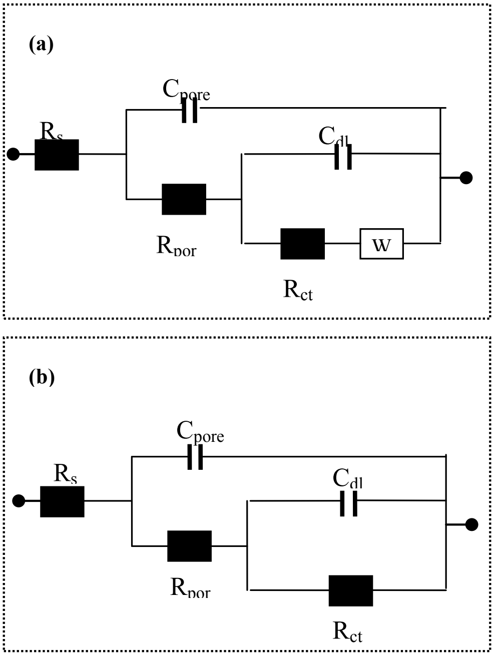

Figure 6.7. Equivalent circuits for the EIS spectra of the bare SS316L and CrN/Cr coated SS316L with artificially induced defects under OCV conditions: (a) Equivalent circuit for the CrN/Cr coated SS316L with artificial defects under OCV conditions with N_2 purged environment; (b) Equivalent circuit for other cases [139].

In contrast, completely different behaviors are seen in the case of the CrN/Cr coated SS316L specimen in the HT-PEFC environment with the N_2 purged atmosphere. At firstly, the emerging of diffusion-controlled electrochemical behavior might indicate the electrolyte passing through the damaged sites and traveling into the area beneath the coating. This behavior reflects the low anti-corrosion properties of the passive layer formed at the damaged site being unable to hinder the electrolyte's passage into the depth between the substrate and coating. The charge transfer resistance of the substrate at the defective sites of the CrN/Cr coated SS316L specimen in the simulated HT-PEFC environment with an N_2 purged atmosphere is mere ca. 3 times greater prior to the corrosion tests as compared with the bare one, and even decreased to ca. one-third that of the bare one following the corrosion tests. The decreased charge transfer resistance of the substrate for the CrN/Cr coated SS316L specimen with artificially induced defects in the simulated HT-PEFC environment with the N_2 purged atmosphere in contrast to the bare one might be due to the localized corrosion resulting in significant current flow through the defects. After combining these results with those in Chapter 3, it could be concluded that the Cr-rich layers formed in the hot phosphoric acid with an O_2 purged atmosphere have superior anti-corrosion ability able to tolerate the effects of hot phosphoric acid. This type of passive layer could give the CrN/Cr coating self-healing ability and hinder electrolyte passage through the damaged site to the substrate when the defects appeared on the surface of the CrN/Cr coating. In contrast, the passive layer formed in the N_2 purged atmosphere demonstrated weak stability in hot phosphoric acid.

Table 6.3. *Fitted results for the EIS spectra from Figure 6.6.*

samples	**R_s (Ω cm^2)**	**C_{dl} (Ω cm^{-2} s^{-n})**	**R_{ct} (Ω cm^2)**	**n_{dl}**	**C_{pore} (Ω cm^{-2} s^{-n})**	**n_{pore}**	**R_{pore} (Ω cm^2)**	**W(Ω s$^{-0.5}$ cm^{-2})**
CrN/Cr-SS316L (O_2 before)	1.874	$5.568*10^{-5}$	$2.861*10^4$	0.917	$8.401*10^{-5}$	0.903	673.862	/
CrN/Cr-SS316L (O_2 after)	1.811	$1.651*10^{-4}$	$1.310*10^4$	0.967	$1.389*10^{-4}$	0.870	143.56	/
CrN/Cr-SS316L (N_2 before)	1.881	$4.363*10^{-3}$	212.039	0.344	$9.787*10^{-5}$	0.903	212.877	0.928
CrN/Cr-SS316L (N_2 after)	1.868	$1.652*10^{-2}$	21.041	0.63	$1.915*10^{-4}$	0.848	86.3854	0.0921
SS316L(O_2)	2.013	$5.557*10^{-2}$	66.446	0.799	$3.5*10^{-4}$	0.946	48.666	/
SS316L(N_2)	1.778	$4.699*10^{-2}$	72.212	0.817	$2.934*10^{-4}$	0.936	56.109	/

6.6 Summary

The present chapter investigates the effects of oxygen on the corrosion behavior of CrN/Cr coated SS316L with artificially produced defects in the simulated cathodic environment of an HT-PEFC. The following results were observed:

i. The CrN/Cr coating with artificially created defects also showed similarly excellent protective efficiency (> 99.9%) with the bare SS316L specimen in the 85 wt. % H_3PO_4 at RT as compared with the CrN/Cr coating without artificially induced defects, regardless of gases (nitrogen and oxygen) purged into the electrolyte.

ii. At 130 °C, the CrN/Cr coated SS316L specimens with artificially created defects exhibited corrosion behaviors in simulated HT-PEFC environments with an N_2 and O_2 purged atmospheres. The CrN/Cr coating with artificially produced defects were able to retain integrity in the O_2 purged atmosphere following the corrosion tests, while the CrN/Cr coating with artificial defects in the N_2 purged atmosphere showed severe flaking following the corrosion tests.

iii. The presence of O_2 assisted the passive layer formed at the damaged sites of the CrN/Cr coating in an O_2 purged atmosphere to gain superior anti-corrosion properties and stability in hot phosphoric acid, which was able to hinder the electrolyte passage through the defects and directly to the substrate.

According to Chapter 5, the CrN/Cr coating exhibited very good performance in a simulated HT-PEFC environment. Chapter 6 shows that the CrN/Cr coating even possessed self-healing ability in the simulated environment of the HT-PEFC with the existence of oxygen when defects appeared on the surface. Therefore, the bilayer CrN/Cr coating might make it possible to use low-cost metallic BPPs in the HT-PEFC, even for mobile applications where vibration causes defects on the coatings. In order to validate our assumption and the performance of CrN/Cr coating in a real HT-PEFC, the performance and durability of HT-PEFCs with different types of BPPs (graphite, bare SS316L, and CrN/Cr coated SS316L BPPs) were compared. The results and discussion are detailed in Chapter 8.

Chapter 7 The Performance and Durability of HT-PEFCs with Different Types of Bipolar Plates

From Chapters 5 and 6, the corrosion behaviors of CrN/Cr coated SS316L with and without artificially induced defects in the simulated HT-PEFC environments were showed. One conclusion in Chapter 5 is that the bilayer CrN/Cr coating can impart superb corrosion resistance and high conductivity to the substrate; both properties are satisfying the requirements of DOE. Chapter 6 relates the corrosion behaviours of the CrN/Cr coating when defects appeared on its surface and found that the presence of oxygen in the electrolyte could give the CrN/Cr coating a self-healing ability in the simulated HT-PEFC environment and assist the CrN/Cr coating with many defects to gain good corrosion resistance in the simulated HT-PEFC environment. Hence, with such coating, it is possible to choose lower-cost BPP for many applications of HT-PEFCs, whether stationary or mobile.

All the experiments mentioned above were performed in the simulated HT-PEFC environment by using 85 wt.% H_3PO_4. In order to validate the performance of CrN/Cr coating in a real HT-PEFC environment, three single cells with different BPPs (graphite, bare SS316L, and CrN/Cr coated SS316L BPPs) were assembled. This chapter evaluates and compares the performance and durability of HT-PEFCs with different BPPs. A part of this work have been submitted for publication [141].

7.1 CrN/Cr coating in real bipolar plates

In order to eliminate the influence of mechanical deformation in thin metallic BPPs fabricated by stamping and focus on the corrosion of the metallic BPP within HT-PEFCs, metallic BPPs fabricated by machinery were employed in this research; they are detailed in Figure 3.9. CrN/Cr was coated on both sides of a bare SS316L metallic BPP by Teer Coating, Ltd., using a CFUBMSIP system. The surface morphologies of the bare and CrN/Cr coated SS316L BPPs are showed in Figure 7.1, and the corresponding material compositions measured by EDX are shown in

Table *7.1*. From Figure 7.1, it could be seen that the CrN/Cr coatings were successfully fabricated on the surface of the channel and land of bare SS316L BPPs, although some pinholes remained on the surface of the CrN/Cr coating, which are the common defects for the coatings fabricated by PVD, especially for mass production and substrates of complex structures.

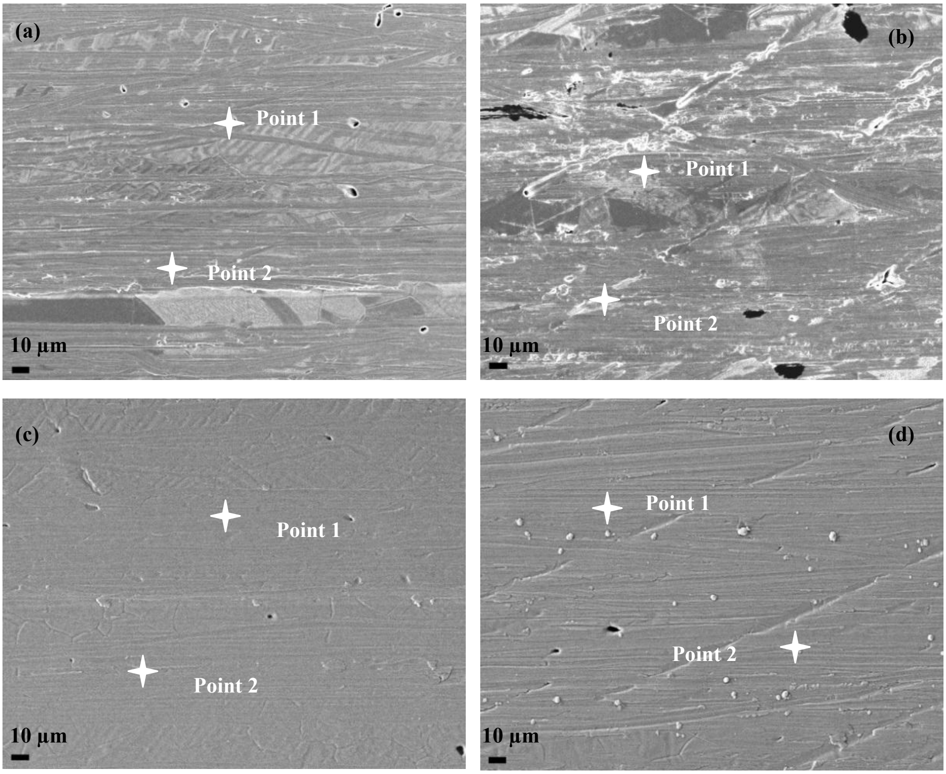

Figure 7.1. *SEM of bare and coated metallic bipolar plates: (a) channel of the bare SS316L bipolar plate. (b) land of the bare SS316L bipolar plate. (c) channel of the CrN/Cr coated SS316L bipolar plate. (d) land of the CrN/Cr coated SS316L bipolar plate.*

The EDX measurements show that the compositions of bare SS316L metallic BPPs and CrN/Cr coated one are nearly identical to those shown in Table 3.1. One remarkable phenomenon is the presence of oxygen element on the surface of the CrN/Cr coated SS316L metallic BPPs in the channel position. This phenomenon might be explained by the pre-cleaning operation with Ar prior to the deposition of the coating; it would be difficult for the effectively cleaning of the surface on the channel position due to the impeditive effect of the land, which finally resulted in the presence of an oxide layer beneath the coating. This behavior indicates that the design parameters of the channel and land are essential for the good coatings on the metallic BPP.

***Table 7.1**. EDX data (in wt.%) of bare and CrN/Cr coated SS316L bipolar plate before 1000 h durability test.*

Sample	Measure point	O	N	Si	Cr	Mn	Fe	Ni	Mo
SS316L	Channel& point 1	\	\	0.4	17.9	1.9	66.9	10.1	2.7
SS316L	Channel& point 2	\	\	0.6	18.2	1.6	67.3	9.8	2.4
SS316L	Land& point 1	\	\	0.3	17.8	1.5	68.7	9.2	2.4
SS316L	Land& point 2	\	\	0.2	18.1	2.0	67.4	9.8	2.5
Coated SS316L	Channel& point 1	3.4	12.7	\	81.6	0.4	2.0	\	\
Coated SS316L	Channel& point 2	3.0	11.9	\	82.0	0.6	2.1	0.4	\
Coated SS316L	Land& point 1	\	11.9	0.1	87.2	0.3	0.4	\	\
Coated SS316L	Land& point 2	\	11.3	0.1	87.8	0.3	0.6	\	\

7.2 Single-cell performance and durability

The three single cells with different types of BPPs were run under constant current loads of 200 mA cm^{-2} for 1000 h to evaluate the performance and durability of single cells with diverse BPPs. The polarization curves of the three single cells with varied different BPPs were carried out at BOL and EOL, as shown in Figure 7.2.

At the BOL, the single cell with graphite BPPs shows the best performance due to its having the lowest ICR value in all three types of BPPs (as shown in Figure 7.7). For the same reason (highest ICR value), the performance of a single cell with bare SS316L BPPs showed the worst performance among all these three cells.

After 1000 h of running under a galvanostatic operation at 0.2 A cm^{-2}, the single cell with CrN/Cr coated SS316L BPPs showed almost no degradation, which indicates the good performance of the CrN/Cr coating in a real HT-PEFC. However, the single cells with both graphite BPPs and bare SS316L BPPs showed degradation.

The corresponding relationship of the degradation rates on the current densities obtained from the polarization curves at BOL and EOL are shown in Figure 7.2(b). Depending on the current density, three types of degradation/activation effects can be distinguished on fuel cells: (i) at low current densities, the cell potential drops as a result of the activation polarization; (ii) at moderate current densities, the cell potential decreases linearly with the current due to ohmic losses; (iii) at high current densities, the cell potential drops as a result of mass transport losses [50]. Figure 7.2(b) shows that activation losses dominate at current densities lower than 0.15 A cm^{-2}, ohmic losses prevail in the current region from ca. 0.15 A cm^{-2} – 0.8 A cm^{-2}, while mass transport losses are significant at current densities higher than 0.8 A cm^{-2}.

From Figure 7.2(b), we could see that the single cells with graphite and bare SS316L BPPs revealed a linear increase in their degradation rate within the ohmic losses region, which indicates an apparent increase in ohmic resistance after 1000 h of durability tests. In contrast, the degradation rate of the single cell with CrN/Cr coated SS316L BPPs showed no increase in the region of ohmic losses, which indicated an absence of increase in the single cell's ohmic resistance. This indicates not only the good performance of the CrN/Cr coating in a real HT-PEFC, but also the superiority of coated metallic BPPs as compared to graphite ones for HT-PEFC applications. For the current densities within the activation losses, the degradation rates of the single cells with graphite and bare SS316L BPPs steeply increased with a decrease in current density. Conversely, the single cell with CrN/Cr coated SS316L BPPs demonstrated no increase but a decrease in the degradation rates in the activation losses region. For current densities higher than 0.8 A cm^{-2}, where mass transport losses dominate, the degradation rates for all three single cells showed a faster increase trend with an increase in current density. In order to ascertain the reason for the different degradation behaviors of the HT-PEFCs with different BPPs, EIS at BOL and EOL of the 1000 h durability tests were performed. The results and discussion are shown in the next section.

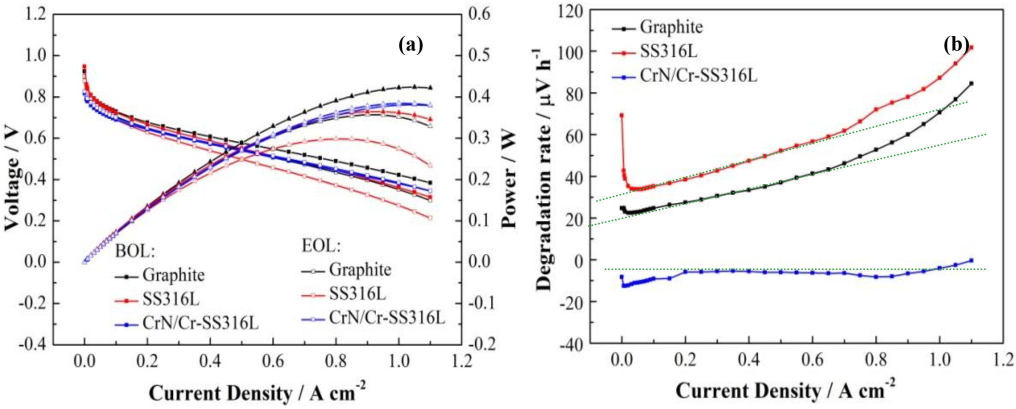

Figure 7.2. *Polarization curves of the HT-PEFCs at BOL and EOL (a) [141]; corresponding degradation rates (b).*

7.3 Electrochemical Impedance Spectroscopy

In order to distinguish and quantify various factors in polarization loss, EIS measurements were carried out at BOL and EOL under working conditions with a current density of 200 mA cm^{-2}. After using the equivalent circuit to simulate the EIS data (as shown in Figure 3.11), the ohmic resistance (R_Ω), protonic resistance (R_p), and charge transfer resistance (R_{ct}) could be extracted from the impedance spectra. Figure 7.3 details all resistances from single cells with different BPPs at BOL and EOL.

From Figure 7.3(a), it could be seen that the R_Ω of the single cell with graphite BPPs displays the lowest value within these three single cells and the single cell with bare SS316L BPPs gives the highest one at BOL. Since the MEAs used in this study are identical, the difference in the R_Ω of the HT-PEFCs with different BPPs arises from the different interfacial conductivity of the various types of BPPs, as shown in Figure 7.7. The results in Figure 7.3(a), Figure 7.2(a) and Figure 7.7(a) are consistent with each other. After running for 1000 h, the R_Ω of a single cell with graphite and bare SS316L BPPs increased. In contrast, the R_Ω of the single cell with CrN/Cr coated SS316L bipolar plates decreased after 1000 h of durability tests. The reason for the increase in R_Ω on the single cell with graphite BPPs mainly derives from the leaching of phosphoric acid from the membrane due to the high surface porosity of the graphite materials. This leaching increases the resistance of the membrane [67]. In the case of the HT-PEFC with the bare SS316L BPPs, the increase in R_Ω is greater than that of the graphite one. Due to the aggressive environment of the HT-PEFC, the surface of the bare SS316L was corroded during the durability test, as shown in Figure 7.4. The surface porosity would have increased following corrosion and, in turn, would also cause the phosphoric acid to leach from the membrane. Except for the absorption of phosphoric acid by the corroded metallic BPPs, the increase in ICR between bare SS316L BPPs and GDL (as shown in Figure 7.7) due to the corrosion phenomenon is another reason for the further increase of the R_Ω of HT-PEFC with bare SS316L BPPs. For the case of HT-PEFC with CrN/Cr coated SS316L BPPs, the surface of the BPPs is dense and compact, and the CrN/Cr coating has superior corrosion resistance in the aggressive environment of the HT-PEFC. Therefore, the leaching effect of phosphoric acid based on the porosity of BPPs would be dramatically weakened. Further, with the running of the HT-PEFC, the membrane would thin, caused by the dissolution of the membranes into phosphoric acid, resulting in a decrease in membrane resistance [142].

R_p represents the protonic resistance in the CL (mainly due to the cathode). The protonic resistance is mainly influenced by the interface and structure of the MEA [143, 144]. Figure 7.3(b) shows that the R_p of all three cells increased after 1000 h of durability tests. The increase in R_p after 1000 h of durability tests may result from the interfacial and structural changes in the MEA during the tests [145]. The mass transport in the MEA is also influenced by the interface and structure of the MEA; therefore, increases in mass transport losses in all three cells following durability tests (as shown in Figure 7.2 (b)) may also result from the interfacial and structural changes of aged MEA as compared with fresh version.

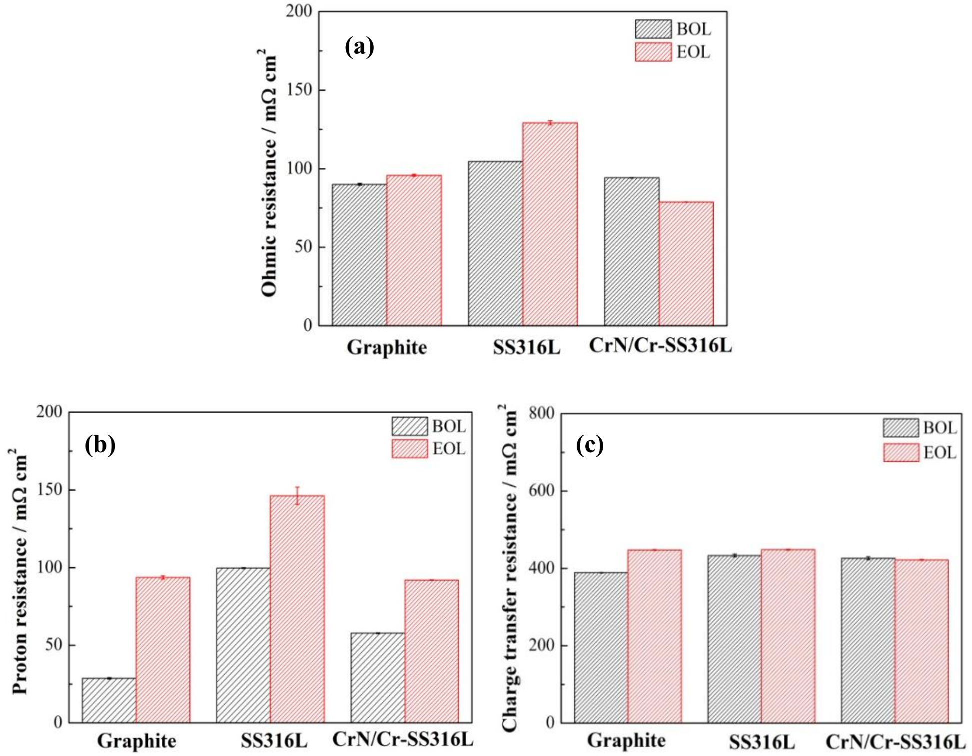

Figure 7.3. *The resistances (ohmic resistance, proton and charge transport resistances in CL) of HT-PEFCs with three different types of bipolar plates at BOL and EOL: (a) ohmic resistance; (b) proton resistance; (c) charge transfer resistance.*

The R_{ct} mainly represents the charge transfer process of the oxygen reduction reaction in the cathode CL, because it is mainly influenced by the kinetics of the oxygen reduction reaction process. The R_{ct} of the three single cells with different types of BPPs at BOL and EOL are shown in Figure 7.3(c). The R_{ct} of the single cells with graphite and bare SS316 BPPs increased after the 1000 h durability tests. In contrast, the R_{ct} of the single cell with the CrN/Cr coated SS316L BPPs decreased after the 1000 h durability test. The different behavior of the R_{ct} of the HT-PEFC indicates the diverse change in the electrochemical activity of the ORR during the durability tests. Under normal conditions, during the running of the fuel cell, the catalyst powders (Pt) agglomerate together and increase in size, leading to a decrease in the electrochemical active surface area (EASA). The decrease in EASA results in a decrease in the exchange current density and finally lead to an increase in R_{ct} [146]. This is the case for all three cells. Therefore, it is reasonable that the R_{ct} of the HT-PEFC with the graphite and bare SS316L BPPs increased following 1000 h of durability tests. In order to explain the decrease in the R_{ct} of HT-PEFC with the CrN/Cr coated SS316L BPPs after the 1000 h durability test, we need to combine the effects of Pt agglomeration and phosphoric acid leaching. As explained above, the compact and dense surface of the CrN/Cr coating could reduce the leaching of the phosphoric acid from the membrane to the BPPs. Therefore, the phosphoric acid content in the CL might increase due to the release of phosphoric acid from the aged membrane. The increase in the amount of phosphoric acid in the CL will increase the EASA of the entire MEA. As a result, the decrease in R_{ct} of the HT-PEFC with the CrN/Cr coated SS316L BPPs may have been caused by the increase in the phosphoric acid content of the CL.

7.4 Surface analyzation after 1000 h durability tests

After 1000 h of durability tests, the surfaces of the bare and coated metallic BPPs were analyzed again by SEM in order to investigate the corrosion products formed and the stability of the CrN/Cr coating during the tests. Figure 7.4 shows the morphologies of the corroded metallic BPPs after being run for 1000 h at a constant load of 200 mA cm^{-2}, while the corresponding compositions of the measured points are listed in
Table *7.2*. Figure 7.5 gives the morphologies of the CrN/Cr coated metallic BPPs following the durability tests, and the corresponding compositions of the measured points are shown in Table 7.3.

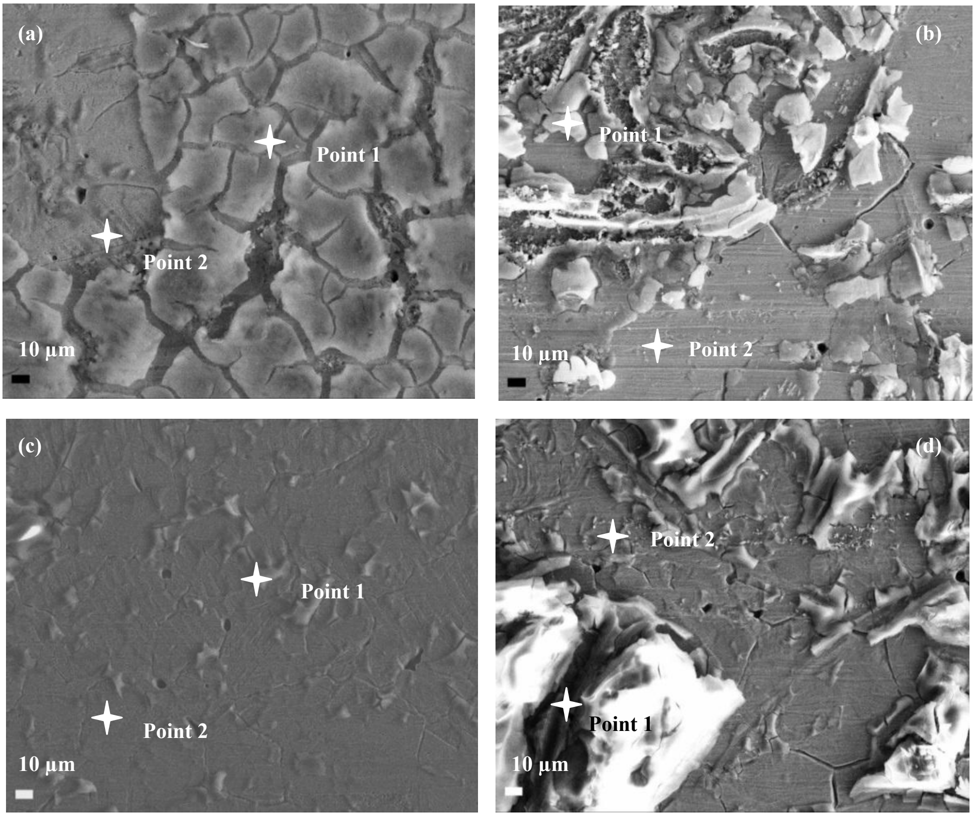

Figure 7.4. *SEM of the SS316L bipolar plates following the 1000 h durability test: (a) a channel of the anodic bipolar plate; (b) a land of the anodic bipolar plate; (c) a channel of the cathodic bipolar plate; (d) a land of the cathodic bipolar plate [141].*

From Figure 7.4, it can be noted that much corrosion products have formed on the surfaces of the bare SS316L metallic BPPs, with the corrosion products covering nearly the entire area of the surfaces. The compositions shown in

Table ***7.2*** reveal that the corrosion products are metal phosphates or oxides. One interesting phenomenon is that there were fewer corrosion products on the channel of the cathodic side of the HT-PEFC than at the other sites; i.e., on the land of the cathodic and anodic sides and on the channel of the anodic side. It is assumed that the moisture environment and higher amount of gas flow weakened the connection between the corrosion products and the substrate. Finally, some corrosion products were blown away by the high amount of gas flow or the cleaning operation before the SEM measurements. The overall extent of the corrosion was extremely high on the bare metallic BPPs after the 1000 h durability tests, and these less conductive corrosion products on the surfaces of the metallic BPPs will dramatically increase the interfacial contact resistance between the metallic BPPs and the GDL, resulting in an increase in the ohmic resistance of the cell, and finally resulting in a decrease in the cell's performance. Therefore, the coatings were obligatory for applying for the metallic BPPs within the HT-PEFC.

Table 7.2. *EDX data (in wt.%) of the bare SS316L following 1000 h durability test.*

Sample	measure point	O	Si	P	Cr	Mn	Fe	Ni	Mo
SS316L	Anode channel& point 1	30.8	\	9.7	10.2	0.3	41.8	5.9	1.4
SS316L	Anode channel& point 2	13.6	0.5	2.9	13.7	0.3	58.4	8.5	2.2
SS316L	Anode land& point 1	52.2	\	25.1	3.0	0.2	15.5	3.6	0.4
SS316L	Anode land& point 2	4.2	0.4	0.5	16.2	1.3	64.9	10.4	2.2
SS316L	Cathode channel& point 1	50.7	\	16.4	6.5	0.1	23.6	2.8	\
SS316L	Cathode channel& point 2	13.0	0.5	2.3	15.9	0.4	57.4	8.3	2.2
SS316L	Cathode land& point 1	51.1	\	22.8	3.2	0.2	21.1	1.6	\
SS316L	Cathode land& point 2	14.1	0.4	2.8	15.6	0.8	54.8	9.6	1.9

After coating with CrN/Cr coating, the extent of the corrosion decreased markedly on the metallic BPPs, as shown in Figure 7.5. Figure 7.5 shows that the overall surface of the CrN/Cr coated metallic BPPs was cleaner as compared with the bare one, with only several small corrosion products on the cathodic side. The CrN/Cr coating kept its integrity on the anodic side after the 1000 h durability test, while several corrosion products appeared on the cathodic side. This indicated that the corrosive environment of the anode side of a real HT-PEFC is much less than the cathodic side. The reason behind this phenomenon might be that, on the one hand, the environment of the anodic side of the HT-PEFC is a relatively dry, and the phosphoric acid is leached at a much lesser degree from the membrane to the anode; conversely, the water produced at the cathodic side causes more significant phosphoric acid leaching from the membrane into the cathode, and the more humid atmosphere at the cathode has further boosts the corrosive environment. The small corrosion products formed at the cathode are also metal phosphate or -oxide, as shown in Table 7.3.

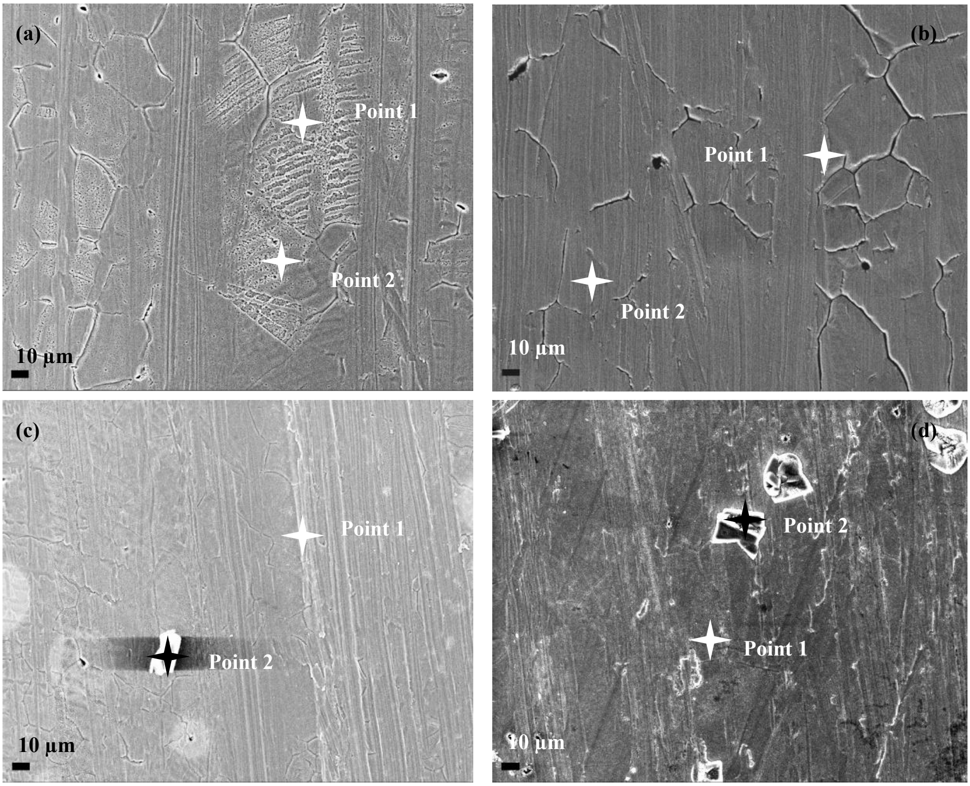

Figure 7.5. *SEM results of the CrN/Cr coated SS316L bipolar plates after the 1000 h durability test: (a) a channel of anodic bipolar plate; (b) a land of anodic bipolar plate; (c) a channel of cathodic bipolar plate; (d) a land of cathodic bipolar plate [141].*

Table 7.3. *EDX data (in wt.%) of the CrN/Cr coated SS316L after the 1000 h durability test.*

Sample	**measure point**	**N**	**O**	**P**	**Cr**	**Mn**	**Fe**	**Ni**
Coated SS316L	Anode channel& point 1	12.2	\	\	85.8	\	2.0	\
Coated SS316L	Anode channel& point 2	11.0	\	\	85.9	\	2.6	0.5
Coated SS316L	Anode land& point 1	12.0	\	\	87.4	\	0.5	\
Coated SS316L	Anode land& point 2	11.9	\	\	87.6	\	0.6	\
Coated SS316L	Cathode channel& point 1	11.7	5.0	\	81.5	\	1.8	\
Coated SS316L	Cathode channel& point 2	\	25.8	9.3	61.6	\	3.0	0.4
Coated SS316L	Cathode land& point 1	11.7	\	\	87.8	\	0.5	\
Coated SS316L	Cathode land& point 2	\	39.5	31.2	4.6	4.3	3.08	17.4

7.5 ICP-OES measurements

In order to clarify the protective effects of the CrN/Cr coating in a real HT-PEFC, the type and the number of metal ions within the MEA following the 1000 h durability tests were analyzed using ICP-OES, as shown in Figure 7.6. From Figure 7.6, it could be seen that, after coating the plates with CrN/Cr, the number of metal ions leaching from the metallic BPPs into the MEA had decreased. By calculating the ratio for the amounts of Fe in the two MEAs, which is the representative and largest amount of the element in 316L stainless steel, it could be found that the overall protective effect of the CrN/Cr coating was ca. 80 %. This means that the Fe element in the MEA had been reduced by 80 % by the CrN/Cr coating on the metallic BPPs following the 1000 h durability tests. One remarkable element was that the Cr content in the MEA of the single cell with coated metallic BPPs was higher than that of the bare one. This is reasonable, since the content of Cr in the CrN/Cr coating is higher than 80%, while the content of Cr in the SS316L is less than 20 %. But the interesting point is that even the amount of Cr in the MEA with the coated metallic BPPs is higher than that of the bare one, while all the varieties of resistances extracted from the impedance spectra for the coated one were much lower than those of the bare one, and the trend of the charge transfer and ohmic resistance of the coated one had even decreased. This phenomenon indicates that the Cr elements have negligible influence on the electrochemical performance of the HT-PEFC. This is also a positive factor for the application of Cr-rich coatings in the HT-PEFCs.

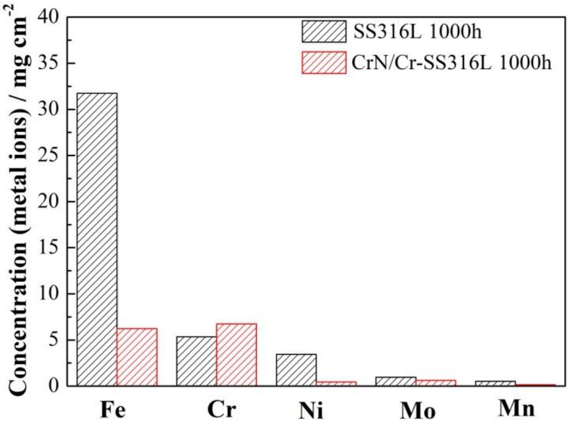

Figure 7.6. *The contents of various metal ions leaching from the bare and coated metallic bipolar plates into the membrane after the 1000 h durability tests, measured by ICP-OES.*

7.6 Interfacial contact resistance

The interfacial contact resistance (ICR) between the BPPs and the GDL is important for the output of a fuel cell. The formation of non-conductive corrosion products on the surface of the metallic BPPs will increase the ICR between the BPPs and the GDL. In order to qualitatively investigate the ICRs of bare and coated metallic BPPs before and after the 1000h durability tests, the changes in the ICR values under a compressive force of 140 N cm^{-2} before and after the tests along with those of the reference graphite BPP were determined, as showed in Figure 7.7. The surface area chosen for the calculation of the ICR is the area of the surface on the side containing the flow field.

From Figure 7.7(a), it could be seen that the ICR values of the graphite BPPs were lowest, and the ICR values of the bare SS316L BPPs were the highest. These results correspond with the EIS results mentioned in Figure 7.3. The apparent difference in the values of the ICR between the BPPs of the cathode and the anode is mainly due to the varied sizes of the BPPs in the corresponding side, as shown in Chapter 3. In a normal situation, with increases in size, the plane of the specimen would decrease, resulting in a more limited contact area. This smaller contact area would increase the interfacial contact resistance level. This is the reason for the ICR value of the cathodic side of the graphite BPPs being higher than the anodic one. In contrast, in the metallic BPPs, the ICR value of the anodic side is higher than that of the cathode. An explanation suggested is that the smaller but thicker plate would be subject to more serious deformation following the machinery operation due to its metal’s greater flexibility. Thus, the contact area of the anode was lesser than that of the cathode, with a resulting higher ICR value at the anode.

By comparing Figure 7.7(a) and (b), the changes in the ICRs before and after the 1000 h durability tests might reflect to some degree the degradation of the bare and coated metallic BPPs during the 1000 h durability tests. By comparison, it could be found that the ICR values for the bare metallic BPPs had dramatically increased after 1000 h of durability tests. These dramatically increased ICRs reflect the serious corrosion of the metallic BPPs during these durability tests. Also, the higher ICR value for the cathode relative to anode following the 1000 h durability tests also indicates the more serious corrosion of the metallic BPPs at the cathode due to the harsher corrosive environment of the cathodic side than the anodic.

For the CrN/Cr coated SS316L BPPs, the value of the ICR for the cathodic side is also higher than that of the anodic after 1000 h of durability tests, which indicates the more serious degradation of the coating at the cathode side. The ICR of the cathodic BPP increased to 176 mΩ cm^2 following 1000 h of durability tests, which is eight times greater than it was prior to the test, and the ICR of the anodic BPP was 40 mΩ cm^2 after the 1000 h durability tests, which are similar to the fresh one (34 mΩ cm^2). These results correspond to those in Section 7.3, in which the CrN/Cr coating at the anode side maintains integrity after the 1000 h durability test and the CrN/Cr in the cathode side exhibits a break-down area and the formation of corrosion products on its surface after 1000 h durability test. After considering the EIS results, it was found that the slight increase in ICR of the coated BPPs does not reflect the ohmic resistance of the single cell. This is because the ohmic resistance of the single cell system is mainly dominated by the membrane resistance.

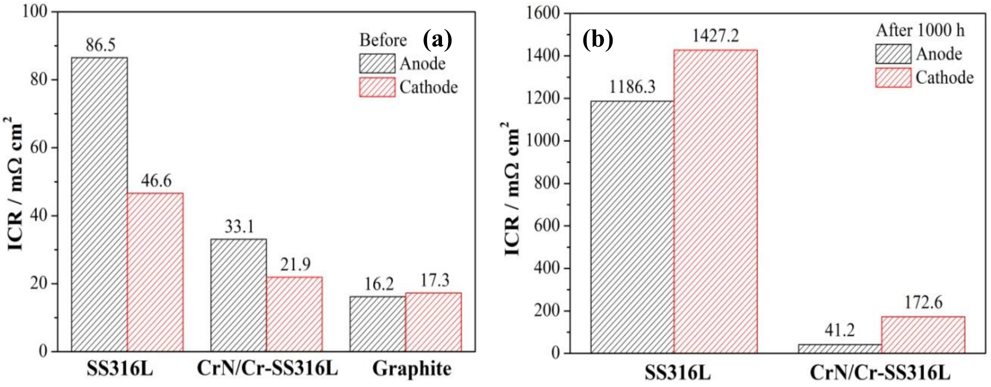

Figure 7.7. *The ICR values from the bare and CrN/Cr coated SS316L metallic bipolar plates before and after 1000 h durability tests under a compressive force of 140 N cm^{-2}, combined with the reference graphite bipolar plates; (a) before the 1000 h durability tests; (b) after the 1000 h durability tests.*

7.7 Summary

The present chapter investigates the performance and durability of the real HT-PEFC with three types of BPPs (graphite; SS316L and CrN/Cr coated SS316L BPPs). The single cell with graphite BPPs demonstrated the best performance at BOL, while the single cell with bare SS316L BPPs exhibited the worst. After a 1000h run in the galvanic mode on 200 mA cm^{-2}, the single cell with the CrN/Cr coated SS316L BPPs showed almost no degradation, while the other two revealed apparent deterioration. The results of this chapter validate the good performance of CrN/Cr coating in a real HT-PEFC and indicate that coated metallic BPP is superior to graphite ones due to the relationship of the uptake of phosphoric acid on the porosity of the plate's surface.

Chapter 8 Discussion

Metallic BPPs possess two main advantages as compared with graphite BPPs: (i) cost-effective and scalable manufacturing processes through punching or forming; (ii) the increased gravimetric and volumetric power density of their fuel cell stacks. For example, a double-faced metallic BPPs formed using 0.1 mm thick stainless steel can save ca. 80 % of the weight and more than 50 % of the volume of a fuel cell stack compared with graphite BPPs with a thickness over 2 mm[30]. The HT-PEFC operates in the range of 120 – 180 °C and currently employs phosphoric-acid-doped PBI membranes, resulting in a fairly aggressive environment for the HT-PFECs' components, especially for those of metallic BPPs. The task of this work was an investigation into the possibility of using metallic BPPs rather than graphite ones in the HT-PEFC.

The main topics of this thesis are the corrosion of bare metallic BPPs in a simulated HT-PEFC environment, coating selection and research into the application of HT-PEFCs.

- Concerning corrosion research on bare metallic BPPs in simulated HT-PEFC environments, 316L stainless steel was selected as the candidate from both the economic and technical viewpoints (SS316L is one of the cheapest types of stainless steel, while nonetheless maintaining reasonable corrosion resistance in hot phosphoric acid). For a real HT-PEFC, oxygen or air are introduced into the cathodic side, while hydrogen or reformate are purged into the anodic side. Aside from their different potentials, the BPPs at the cathode and anode of an HT-PEFC experience difference in their gases atmospheres. It is important to investigate the effects of these gases atmospheres and potentials on the corrosion of metallic BPPs in simulated HT-PEFC environments.
- Through the corrosion research on SS316L in simulated HT-PEFC environments, it has been found that the passive layer formed within the simulated cathodic HT-PEFC environment is able to resist the harsh conditions created by hot phosphoric acid when with an O_2 purged atmosphere. Based on this idea, the bilayer CrN/Cr coating was tested in the simulated HT-PEFC environment. This CrN/Cr coating composed of an inner Cr layer and an outmost CrN layer was successfully deposited on the surface of 0.1 mm thick SS316L BPPs by a reactive magnetron sputtering method and. It was predicted that such a coating would demonstrate excellent performance in the simulated HT-PEFC environment, an assumption which was proven correct.
- The coatings fabricated by PVD will inevitably display some defects, including pinholes,

on their surfaces. The application of fuel cells to mobility technology, such as in cars and planes, introduces a vibrational environment for their components. The intense vibration would also cause defects in the coatings. Therefore, the resistance of the coatings to defect development when in harsh environments is vital for mobile applications. In this regard, numerous artificial defects were fabricated on the surfaces of the CrN/Cr coatings and their corrosion behaviors investigated in the simulated HT-PEFC environment. From the previous results, it was recognized that an oxygen permeated atmosphere forms a protective Cr-rich layer with high stability in hot phosphoric acid on the SS316L substrate. In this way, the effects of oxygen on the corrosion behavior of the CrN/Cr coated SS316L specimens with artificially produced defects were investigated.

- The most promising candidate materials for BPPs (CrN/Cr-coated SS316L) were subsequently used in a long-term one-thousand-hour test under a real HT-PEFC and compared against the results of bare SS316L BPPs and reference graphite BPPs.

The bilayer CrN/Cr-coated SS316L BPPs demonstrate excellent performance under both simulated HT-PEFC environment and real HT-PEFC conditions. In the simulated HT-PEFC environment (85 wt. % H_3PO_4, at 130 °C), the free corrosion current density of the CrN/Cr coated SS316L specimen is only ca. 0.1 $\mu A\ cm^{-2}$, while the current densities are less than 0.01 $\mu A\ cm^{-2}$ in the simulated cathodic environment of the HT-PEFC and ca. - 1 $\mu A\ cm^{-2}$ in the simulated anodic environment of the HT-PEFC, respectively. The ICRs of CrN/Cr coated SS316L specimens are ca. 5 $m\Omega\ cm^2$ and 7 $m\Omega\ cm^2$, respectively, before and after corrosion tests. All these parameters are superior to the requirements of DOE. In 1000h long-term studies in a real HT-PEFC, an aging rate of nearly zero was observed on the single cell with CrN/Cr coated SS316L BPPs, while the aging rates of single cells with bare SS316L and graphite BPPs were ca. 20 %.

The following is a discussion on different aspects of the material combination of stainless steel 316L and bilayer CrN/Cr coating:

8.1 The economic advantages of metallic bipolar plates

The desired manufacturing costs of PEM fuel cell stacks are around 25-150 € kW^{-1}, depending on the produced quantities, where the bipolar costs are about 5-22 € kW^{-1} [55, 147, 148]. The most commonly used BPP material is graphite, due to its excellent corrosion resistance and interfacial conductivity. The material and machining costs of graphite BPPs are very high, which could account for as much as 60 % of the stack cost. It has been estimated that the cost of metallic BPPs would possibly be less than 20 % of the stack cost [149].

8.2 The technical advantages of metallic bipolar plates

The thickness of graphite-based BPPs is typically 1.5-3.5 mm, while metallic BPPs with a thickness of 0.1 mm can be manufactured by punching or hydro-forming. Table 8.1 provides a comparison of graphite and metallic materials as BPPs in PEFCs [30]. Through Table 8.1, it could be found that using an SS316L with a thickness of 0.1 mm to replace graphite materials, a weight saving of 80 % can be achieved and thus the gravimetric power density of the stack can be significantly increased. Moreover, with use of light metals, like Ti, a weight reduction of even 90 % can be reached. Still, the cost of Ti is ca. 5 times higher than that of SS316L stainless steel. After considering the economic argument, the choice of SS316L is more suitable for the mass production of BPPs where cost is the determining factor. For special applications with extreme requirement regarding gravimetric power density and in the absence of cost restrictions, such as in aerospace programs, Ti may be a good choice.

Table 8.1. *A comparison of graphite and metallic materials as bipolar plates in PEFCs [30].*

Material	**Density/ g cm^{-3}**	**Thickness/ mm**	**Mass per area/ g cm^{-2}**	**Mass per power/ kg kW^{-1}**
Graphite	2.3	2	0.46	1.84
Composite(Graphite)	1.9	2	0.38	1.52
SS316L	7.9	0.1	0.08	0.32
Titanium	4.5	0.1	0.05	0.18

For metallic BPPs, two half-shells are welded together to become a single BPP[68]. In a normal situation, the total thickness of the BPP unit is ca. 1.4 mm after comparison with the thicknesses of graphite-based BPPs formed from two half-plates (4mm) [68, 72, 150], and over 60 % of the space can be reduced using metallic BPPs.

8.3 The corrosion rates and interfacial conductivities of bare and CrN/Cr coated metallic bipolar plates

By employing potentiodynamic polarization tests transformed into Tafel plots, the corrosion current densities of specimens can be determined. The current densities of bare SS316L in 85 wt. % H_3PO_4 are ca. 20 μA cm^{-2} at RT and more than 150 μA cm^{-2} at 130 °C under OCV conditions in a simulated HT-PEFC environment. These results are consistent with those in the publications by our previous colleague, V. Weissbecker *et al*. [25]. The current densities of bare SS316L are ca. 6 μA cm^{-2} in 85 wt. % H_3PO_4, at 130 °C, with an applied potential of 0.65V (simulating the working condition of cathode side) and ca. 60 μA cm^{-2} in 85 wt. % H_3PO_4, at 130 °C, with an applied potential of 0.05V (simulating the working condition of anode side). L. Wang *et al*. reported the related corrosion current densities of bare SS304 in the simulated cathodic and anodic environments of the HT-PEFC, concluding that the corrosion current density of bare SS304 ranges from about 2 to 6 mA cm^{-2} in a simulated HT-PEFC cathodic environment and ca. 68 mA cm^{-2} in a simulated anodic HT-PEFC environment, respectively [33]. By comparison, the corrosion current densities of bare SS316L are around 1000 times lower than that of SS304 in both the cathodic and anodic environments of HT-PEFC, which indicates the good performance of SS316L as a substrate. However, the corrosion current densities of a bare SS316L specimen are still much higher than DOE requirements (less than 1.0 μA cm^{-2}) in the simulated HT-PEFC environment. When coated with a bilayer CrN/Cr coating, the current densities of CrN/Cr coated SS316L specimens are ca. 0.01 μA cm^{-2} at RT and 0.1 μA cm^{-2} at 130 °C, respectively, under OCV conditions. The calculated protective efficiency of a CrN/Cr coating on an SS316L substrate is nearly 100 % at both RT and 130 °C in 85 wt.% H_3PO_4. M. Kouril *et al*. have reported the good performance of Ta in hot phosphoric acid, concluding that the corrosion current density of Ta is about 0.5 μA cm^{-2} in concentrated phosphoric acid at 80 °C and even a minor cathodic polarization is unacceptable for Ta, which induces evolution of hydrogen, resulting in hydrogen embrittlement through formation of hydrides [32]. L. Wang *et al*. have reported that the corrosion current density of a multilayer TaN/Ta coating in 85 wt.% H_3PO_4 at 130 °C is ca. 1.6 μA cm^{-2}. V. Weissbecker *et al*. have mentioned boron-doped diamond coating (BDD) on niobium as BPPs in HT-PEFC, relating that the corrosion current density of BDD coated niobium is ca. 0.5 μA cm^{-2} in 85 wt.% H_3PO_4, at 130 °C [107]. By comparison, we could find that the bilayer CrN/Cr coating displays the lowest corrosion current density from among the related coatings investigated in the published literature. Also, all other coatings reported have used rare metals (such as Ta) or complex preparation processes (such as 2000 °C for BDD coating). Therefore, the bilayer CrN/Cr coating shows high competitivity from its performance in a simulated HT-PEFC environment, from both the technical (easier fabrication process) and economic (low cost) aspects. Under the working potential of the cathodic side of an HT-PEFC (0.65 V), the corrosion current density of CrN/Cr coated SS316L specimen is less than 0.01 μA cm^{-2} in 85 wt.% H_3PO_4 at 130 °C. Alternately, under the working potential of the anodic side of an HT-PEFC (0.05 V), the corrosion current density of the CrN/Cr coated SS316L specimen is ca. -1.0 μA cm^{-2}, with the negative value implying that the coated sample is under cathodic protection. The interfacial contact resistance of the bare SS316L specimen of 0.1 mm thickness is ca. 47 mΩ cm^2 under the compaction force of 140 N cm^{-2}, which is the normal assembly force for a fuel cell stack. The DOE requirements on the BPPs' interfacial contact resistance is less than 10 mΩ cm^2 under a compaction force of 140 N cm^{-2}. After coating with bilayer CrN/Cr coating, the interfacial contact resistance of the CrN/Cr coated SS316L specimen is ca. 5.5 mΩ cm^2 under the compaction force of 140 N cm^{-2}, and only shows a slightly increase (7 mΩ cm^2) following corrosion tests. The corrosion current densities and interfacial contact resistance of the CrN/Cr coated SS316L satisfy the DOE requirements.

8.4 The effect of oxygen on the corrosion behavior of the passive layer of the bare SS316L specimen and the CrN/Cr coated SS316L specimen with artificially induced defects

The existence of oxygen in the simulated cathodic environment of HT-PEFC (applied potential: 0.65 V, electrolyte: 85 wt. % H_3PO_4, temperature: 130 °C) would assist the SS316L substrate in forming a Cr-rich passive layer able to tolerate the harsh environment of hot phosphoric acid. Under the same conditions but with an N_2 purged atmosphere, the Cr-rich passive layer formed on the surface of the bare SS316L specimen was unable to retain its stability in hot phosphoric acid and slowly dissolved. It is evitable for coatings fabricated by PVD to have some defects, like pinholes, on their surfaces. The vibration transportation environment similarly causes cracks in coatings. Therefore, it is very essential that coatings have to have the ability to maintain good corrosion resistance even when cracks form on their surfaces. The CrN/Cr coating with numerous artificially created defects are unable to survive under hot phosphoric acid in an N_2 purged atmosphere. The current density of CrN/Cr coated SS316L with artificially induced defects following 4 h potentiostatic tests at 0.65 V is ca. 100 µA cm^{-2}, with the CrN/Cr coating severely shedding after the corrosion tests. The breakdown of the CrN/Cr coating is mainly caused by localized corrosion occurring under the coating when the electrolyte passes through the coating from the damaged sites and acquire direct contact with the substrate. However, under an O_2 purged atmosphere, the CrN/Cr coated SS316L with artificially induced defects still maintain good corrosion resistance in hot phosphoric acid, and the current densities of the CrN/Cr coated SS316L specimen are ca. 1.0 µA cm^{-2} both before and after 4 h potentiostatic tests, with the CrN/Cr coating maintaining integrity following the corrosion tests. This excellent corrosion resistance held by the CrN/Cr coating with artificially induced defects but with O_2 purged atmosphere when in hot phosphoric acid might due to the stable Cr-rich layer formed under the O_2 purged atmosphere which effectively blocks the electrolyte passing through the damage sites on the surface of the coating, highly restricting localized corrosion. Numerous publications concern the effects of defects on the corrosion behavior of coatings, while almost all studies investigated occurrences under nitrogen purged atmospheres [151-153]. The electrolytes used for these researches were salt solutions or diluted acidic solutions. Our current research represents the first investigation into the effect of oxygen on the corrosion behaviors of coatings in concentrated phosphoric acid.

8.5 Cell performance

In the 1000 h durability tests on single cells with diverse BPPs (graphite, bare SS316L and CrN/Cr coated SS316L BPPs) under a constant current density of 200 mA cm^{-2}, the single cell constructed with graphite BPPs demonstrated the best performance at BOL. The single cell constructed with CrN/Cr coated SS316L BPPs shows the minimum degradation of the cell's performance at either BOL or EOL. The degradation of the single cell with CrN/Cr coated SS316L BPPs is nearly zero, while the single cells with graphite and bare SS316L BPPs show degradation (at higher than 16 %). This not only indicates the excellent performance of the CrN/Cr coating in real HT-PEFC conditions, but also indicates the superiority of coated metallic BPPs compared with graphite BPPs due to the marked uptake of phosphoric acid by porous graphite BPPs, decreasing the performance of the cell. Hartnig *et al.* have also reported similar results[67], concluding that single cells with gold-coated metallic BPPs and surface sealed graphite BPPs show lower degradation rates than those of normal graphite BPPs, attributed to the lesser degree of phosphoric acid loss from the MEA. Alnegren *et al.* have successfully demonstrated the use of bare metallic BPPs in HT-PEFCs and observed a voltage drop of 17 mV at a current density of 200 mV cm^{-2} after 900 h of cell operation [24]. Janßen *et al.* have developed and demonstrated the feasibility of a long-term run (4700 h) of HT-PEFC stack with gold-coated metallic BPPs [68], observing that the cell voltages of the short HT-PEFC stack with gold-coated metallic BPPs firstly increased by approximately 30 mV and then linearly decreased in the following 2000 h, finishing with accelerated degradation rates. Alegre *et al.* have assessed the durability of low-cost Al BPPs for HT-PEFCs and found that Al-based plates provide better initial performance in comparison to the cell with graphite plates，but the single cell with Al-based plates showed severe deterioration in the subsequent 60 h [70]. By comparison, the bilayer CrN/Cr coated SS316L BPPs have shown high potential as low-cost metallic BPPs in HT-PEFC.

Chapter 9 Conclusion

The aim of the present work is to study metallic materials in the interest of replacing the graphite BPPs used in HT-PEFCs. Through systemic research, suitable substitution metallic BPP materials have been found which demonstrated low corrosion rates and interfacial conductive resistance which satisfies DOE requirements. The materials and equipment used in this research are considered for mass production purposes.

The key findings of this work are presented in the following:

- The corrosion current densities for the bare SS316L specimens are much higher than DOE requirements, indicating the impossibility of directly employing bare SS316L in HT-PEFCs. In the simulated anodic environment of the HT-PEFC, bare SS316L was located at the edge of the active corrosion region; it demonstrated a 10-fold higher corrosion current density as compared with that of the simulated cathodic environment of the HT-PEFC which is located in the passive regions of corrosion.
- The passive layer of the SS316L substrate formed in the simulated cathodic environment of the HT-PEFC displays higher stability under an O_2 purged atmosphere than that under an N_2 purged atmosphere, and it is a Cr-rich layer.
- Based on the previous finding, it was anticipated that a coating high in Cr content might demonstrate good performance in the HT-PEFC environment. The bilayer CrN/Cr coating with an inner Cr layer and an outmost CrN layer displays excellent corrosion resistance in hot phosphoric acid. The protective effects of the CrN/Cr coating on the SS316L substrate is nearly 100%. The corrosion current densities under the OCV and working conditions of an HT-PEFC can be much lower than the DOE requirements. Additionally, the interfacial contact resistance of CrN/Cr coated SS316L BPPs achieves about one-half of the requirements of DOE. Therefore, the CrN/Cr coating is promising for employment in HT-PEFC in the interest of using low-cost metallic BPPs.
- The CrN/Cr coating with artificially induced defects had broken down significantly in the simulated HT-PEFC environment with an N_2 purged atmosphere due to the localized corrosion in the area between the substrate and coating. Conversely, oxygen assists CrN/Cr coating with artificially created defects in retaining corrosion resistance in hot phosphoric acid, with the CrN/Cr coating retaining their integrity following corrosion tests in the simulated HT-PEFC environment with an O_2 purged atmosphere. The corrosion current densities of the CrN/Cr coated SS316L specimens with artificially induced defects in the

simulated HT-PEFC environment with an N_2, and O_2 purged atmosphere are ca. 100 and 1.0 μA cm^{-2}, respectively. The reason for the difference in the corrosion behavior of the CrN/Cr coating with artificially induced defects in the simulated HT-PEFC with an N_2 or O_2 purged atmosphere might be due to the formation of a passive layer within a Cr-rich environment only in the presence of an O_2 purged atmosphere. The passive layer formed could help to block the electrolyte from pass through the damaged sites of the coating and thus eliminate localized corrosion. In OCV conditions, but without the existence of O_2 (in an N_2 purged atmosphere), the passive layer is unable to form, making it possible for the electrolyte to pass through the damaged sites, directly contact the substrate, and allow for the occurrence of localized corrosion.

- Long-term single cell tests reveal the excellent performance of CrN/Cr coated SS316L as BPPs. Degradation of the single cell with CrN/Cr coated SS316L BPPs is nearly at zero level following the 1000 h durability tests when compared with the more than 16 % degradation of single cells with graphite and bare SS316L BPPs. The single cell tests also demonstrate the superiority of metallic BPPs as compared against graphite BPPs after considering the positive correlation of the uptake of phosphoric acid on the porosity of their surfaces.

References

1. Spiegel, Colleen. Designing and building fuel cells. Vol. 87. New York: Mcgraw-hill, 2007.
2. Crabtree, George W., Mildred S. Dresselhaus, and Michelle V. Buchanan. "The hydrogen economy." *Physics Today* 57.12 (2004): 39-44..
3. Marbán, Gregorio, and Teresa Valdés-Solís. "Towards the hydrogen economy?." *International Journal of Hydrogen Energy* 32.12 (2007): 1625-1637.
4. Muradov, N. Z., and T. N. Veziroğlu. "From hydrocarbon to hydrogen–carbon to hydrogen economy." *International Journal of Hydrogen Energy* 30.3 (2005): 225-237.
5. Penner, S. S. "Steps toward the hydrogen economy." *Energy* 31.1 (2006): 33-43.
6. Turner, John A. "Sustainable hydrogen production." *Science* 305.5686 (2004): 972-974.
7. Wilkinson, D. P., Zhang, J., Hui, R., Fergus, J., & Li, X. (Eds.). Proton exchange membrane fuel cells: materials properties and performance. CRC Press, 2009.
8. Li, R., Cai, Y., Wippermann, K. and Lehnert, W. "Corrosion and Electrical Properties of SS316L Materials in the Simulated HT-PEFC Environment." *Journal of The Electrochemical Society* 165.10 (2018): C681-C688.
9. Mori, D., and K. Hirose. "Recent challenges of hydrogen storage technologies for fuel cell vehicles." *International Journal of Hydrogen Energy* 34.10 (2009): 4569-4574.
10. Kramer, D., Zhang, J., Shimoi, R., Lehmann, E., Wokaun, A., Shinohara, K. and Scherer, G.G. "In situ diagnostic of two-phase flow phenomena in polymer electrolyte fuel cells by neutron imaging: Part A. Experimental, data treatment, and quantification." *Electrochimica Acta* 50.13 (2005): 2603-2614..
11. Zhang, J., Kramer, D., Shimoi, R., Ono, Y., Lehmann, E., Wokaun, A., Shinohara, K. and Scherer, G.G. "In situ diagnostic of two-phase flow phenomena in polymer electrolyte fuel cells by neutron imaging: Part B. Material variations." *Electrochimica Acta* 51.13 (2006): 2715-2727..
12. Basu, Suman, Jun Li, and Chao-Yang Wang. "Two-phase flow and maldistribution in gas channels of a polymer electrolyte fuel cell." *Journal of Power Sources* 187.2 (2009): 431-443.
13. Meng, Hua, and Chao-Yang Wang. "Model of two-phase flow and flooding dynamics in polymer electrolyte fuel cells." *Journal of the Electrochemical Society* 152.9 (2005): A1733-A1741.

14. Bose, S., Kuila, T., Nguyen, T.X.H., Kim, N.H., Lau, K.T. and Lee, J.H. "Polymer membranes for high temperature proton exchange membrane fuel cell: recent advances and challenges." *Progress in Polymer Science* 36.6 (2011): 813-843.

15. Rosli, R.E., Sulong, A.B., Daud, W.R.W., Zulkifley, M.A., Husaini, T., Rosli, M.I., Majlan, E.H. and Haque, M.A. "A review of high-temperature proton exchange membrane fuel cell (HT-PEMFC) system." *International Journal of Hydrogen Energy* 42.14 (2017): 9293-9314.

16. Wee, Jung-Ho. "Applications of proton exchange membrane fuel cell systems." *Renewable and Sustainable Energy Reviews* 11.8 (2007): 1720-1738..

17. Rostrup-Nielsen, Jens R., Jens Sehested, and Jens K. Nørskov. "Hydrogen and synthesis gas by steam-and CO_2 reforming." (2002): 65-139.

18. Ni, Meng, Dennis YC Leung, and Michael KH Leung. "A review on reforming bio-ethanol for hydrogen production." *International Journal of Hydrogen Energy* 32.15 (2007): 3238-3247.

19. Carmo, M., Fritz, D.L., Mergel, J. and Stolten, D. "A comprehensive review on PEM water electrolysis." *International Journal of Hydrogen Energy* 38.12 (2013): 4901-4934..

20. Cao, Qing. *Modelling of High Temperature Polymer Electrolyte Fuel Cells*. Diss. Universitätsbibliothek der RWTH Aachen, 2017.

21. Oh, Kyeongmin, and Hyunchul Ju. "Temperature dependence of CO poisoning in high-temperature proton exchange membrane fuel cells with phosphoric acid-doped polybenzimidazole membranes." *International Journal of Hydrogen Energy* 40.24 (2015): 7743-7753.

22. Moçotéguy, P., Ludwig, B., Scholta, J., Barrera, R. and Ginocchio, S. "Long Term Testing in Continuous Mode of HT-PEMFC Based H_3PO_4/PBI Celtec-P MEAs for µ-CHP Applications." *Fuel Cells* 9.4 (2009): 325-348..

23. Antunes, R.A., Oliveira, M.C.L., Ett, G. and Ett, V. "Corrosion of metal bipolar plates for PEM fuel cells: a review." *International Journal of Hydrogen Energy* 35.8 (2010): 3632-3647.

24. Alnegren, P., Grolig, J.G., Ekberg, J., Göransson, G. and Svensson, J.E. "Metallic bipolar plates for high temperature polymer electrolyte membrane fuel cells." *Fuel Cells* 16.1 (2016): 39-45..

25. Weissbecker, V., K. Wippermann, and W. Lehnert. "Electrochemical corrosion study of metallic materials in phosphoric acid as bipolar plates for HT-PEFCs." *Journal of The Electrochemical Society* 161.14 (2014): F1437-F1447.

26. Silva, R.F., Franchi, D., Leone, A., Pilloni, L., Masci, A. and Pozio, A. "Surface conductivity and stability of metallic bipolar plate materials for polymer electrolyte fuel cells." *Electrochimica Acta* 51.17 (2006): 3592-3598..

27. Wang, H., and J. A. Turner. "Reviewing metallic PEMFC bipolar plates." *Fuel Cells* 10.4 (2010): 510-519.

28. Weissbecker, V., Reimer, U., Wippermann, K. and Lehnert, W. "A comprehensive corrosion study on metallic materials for HT-PEFC application." *ECS Transactions* 58.1 (2013): 693-704.

29. Li, R., Cai, Y., Wippermann, K. and Lehnert, W. "Electrochemical Behavior of CrN/Cr Coating on 316L Stainless Steel in the Simulated Cathodic Environment of an HT-PEFC." *ECS Transactions* 85.13 (2018): 585-598..

30. Weißbecker, Vitali. Korrosion metallischer Bipolarplatten in Hochtemperatur-Polymerelektrolyt-Brennstoffzellen. No. RWTH-2017-02921. Lehr-und Forschungsgebiet Modellierung in der elektrochemischen Verfahrenstechnik (FZ Jülich), 2017.

31. Escrivà-Cerdán, C.L.A.R.A., Blasco-Tamarit, E., García-García, D.M., García-Antón, J. and Guenbour, A. "Effect of potential formation on the electrochemical behaviour of a highly alloyed austenitic stainless steel in contaminated phosphoric acid at different temperatures." *Electrochimica Acta* 80 (2012): 248-256.

32. Kouřil, M., Christensen, E., Eriksen, S. and Gillesberg, B. "Corrosion rate of construction materials in hot phosphoric acid with the contribution of anodic polarization." *Materials and Corrosion* 63.4 (2012): 310-316.

33. Wang, L., Li, L., Liu, H., Wang, S., Fang, H., Gao, H., Gao, K., Zhang, Y., Sun, J. and Yan, J. "Polylaminate TaN/Ta coating modified ferritic stainless steel bipolar plate for high temperature proton exchange membrane fuel cell." *Journal of Power Sources* 399 (2018): 343-349.

34. Liu, C., Bi, Q., Leyland, A. and Matthews, A. "An electrochemical impedance spectroscopy study of the corrosion behaviour of PVD coated steels in 0.5 N NaCl aqueous solution: Part II.: EIS interpretation of corrosion behaviour." *Corrosion Science* 45.6 (2003): 1257-1273.

35. Yasuda, M., Akao, N., Hara, N. and Sugimoto, K. "Self-healing Corrosion Protection Ability of Composition-Gradient Al2 O 3· Nb Nanocomposite Thin Films." *Journal of The Electrochemical Society* 150.10 (2003): B481-B487.

36. Vielstich, Wolf, Arnold Lamm, and Hubert A. Gasteiger, eds. Handbook of fuel cells: fundamentals technology and applications. Vol. 2. New York: Wiley, 2003.

37. Araya, S.S., Zhou, F., Liso, V., Sahlin, S.L., Vang, J.R., Thomas, S., Gao, X., Jeppesen, C. and Kær, S.K. "A comprehensive review of PBI-based high temperature PEM fuel cells." *International Journal of Hydrogen Energy* 41.46 (2016): 21310-21344.

38. Kumbharkar, Santosh C., Prasad B. Karadkar, and Ulhas K. Kharul. "Enhancement of gas permeation properties of polybenzimidazoles by systematic structure architecture." *Journal of Membrane Science* 286.1-2 (2006): 161-169.

39. Wang, Kai Yu, and Tai-Shung Chung. "Fabrication of polybenzimidazole (PBI) nanofiltration hollow fiber membranes for removal of chromate." *Journal of Membrane Science* 281.1-2 (2006): 307-315.

40. Yang, Tingxu, Youchang Xiao, and Tai-Shung Chung. "Poly-/metal-benzimidazole nano-composite membranes for hydrogen purification." *Energy & Environmental Science* 4.10 (2011): 4171-4180.

41. Han, Yi-Jen, et al. "Hydrophilic chitosan-modified polybenzoimidazole membranes for pervaporation dehydration of isopropanol aqueous solutions." *Journal of Membrane Science* 463 (2014): 17-23.

42. Afshar, A., Yari, M., Larijani, M.M. and Eshghabadi, M. "Effect of substrate temperature on structural properties and corrosion resistance of carbon thin films used as bipolar plates in polymer electrolyte membrane fuel cells." *Journal of Alloys and Compounds* 502.2 (2010): 451-455.

43. Vilčiauskas, L., Tuckerman, M.E., Bester, G., Paddison, S.J. and Kreuer, K.D. "The mechanism of proton conduction in phosphoric acid." *Nature chemistry* 4.6 (2012): 461.

44. Ma, Y.L., Wainright, J.S., Litt, M.H. and Savinell, R.F. "Conductivity of PBI membranes for high-temperature polymer electrolyte fuel cells." *Journal of The Electrochemical Society* 151.1 (2004): A8-A16.

45. He, R., Li, Q., Xiao, G. and Bjerrum, N.J. "Proton conductivity of phosphoric acid doped polybenzimidazole and its composites with inorganic proton conductors." *Journal of Membrane Science* 226.1-2 (2003): 169-184.

46. Yang, Jingshuai, and Ronghuan He. "Preparation and characterization of polybenzimidazole membranes prepared by gelation in phosphoric acid." *Polymers for Advanced Technologies* 21.12 (2010): 874-880.

47. He, R., Li, Q., Bach, A., Jensen, J.O. and Bjerrum, N.J. "Physicochemical properties of phosphoric acid doped polybenzimidazole membranes for fuel cells." *Journal of*

Membrane Science 277.1-2 (2006): 38-45.

48. Lobato, J., Canizares, P., Rodrigo, M.A., Linares, J.J. and Aguilar, J.A. "Improved polybenzimidazole films for H3PO4-doped PBI-based high temperature PEMFC." *Journal of Membrane Science* 306.1-2 (2007): 47-55.
49. Samms, S. R., S. Wasmus, and R. F. Savinell. "Thermal stability of proton conducting acid doped polybenzimidazole in simulated fuel cell environments." *Journal of the Electrochemical Society* 143.4 (1996): 1225-1232.
50. Pinar, F. Javier, Nadine Pilinski, and Peter Wagner. "Long-term testing of a high temperature polymer electrolyte membrane fuel cell: The effect of reactant gases." *AIChE Journal* 62.1 (2016): 217-227.
51. Li, Q., Aili, D., Hjuler, H.A. and Jensen, J.O. "High temperature polymer electrolyte membrane fuel cells." *Springer Switzerland* (2016): 387-425.
52. Dicks, Andrew, and David Anthony James Rand. Fuel cell systems explained. New York: Wiley, 2018.
53. Kakati, Biraj Kr, and Anil Verma. "Carbon polymer composite bipolar plate for PEM fuel cell." *Lap Lambert, Saarbrücken* (2011).
54. Frankel, G. S. "Fundamentals of corrosion kinetics." *Active Protective Coatings*. Springer, Dordrecht, 2016. 17-32.
55. U.S. DOE., DOE Technical Targets for Polymer Electrolyte Membrane Fuel Cell Components. 2017.
56. Dariva, Camila G., and Alexandre F. Galio. "Corrosion inhibitors–principles, mechanisms and applications." *Developments in corrosion protection*. IntechOpen, 2014.
57. Wu, J., Yuan, X.Z., Martin, J.J., Wang, H., Zhang, J., Shen, J., Wu, S. and Merida, W. "A review of PEM fuel cell durability: Degradation mechanisms and mitigation strategies." *Journal of Power Sources* 184.1 (2008): 104-119.
58. Wu, J., Yuan, X.Z., Martin, J.J., Wang, H., Zhang, J., Shen, J., Wu, S. and Merida, W. "A review of PEM fuel cell durability: Degradation mechanisms and mitigation strategies." *Journal of Power Sources* 184.1 (2008): 104-119.
59. Karimi, S., Fraser, N., Roberts, B. and Foulkes, F.R. "A review of metallic bipolar plates for proton exchange membrane fuel cells: materials and fabrication methods." *Advances in Materials Science and Engineering* 2012 (2012).
60. Wind, J., Späh, R., Kaiser, W. and Böhm, G. "Metallic bipolar plates for PEM fuel cells." *Journal of Power Sources* 105.2 (2002): 256-260.

61. Cho, E., Jeon, U.S., Hong, S.A., Oh, I.H. and Kang, S.G. "Performance of a 1 kW-class PEMFC stack using TiN-coated 316 stainless steel bipolar plates." *Journal of Power Sources* 142.1-2 (2005): 177-183.

62. Li, H., Tsay, K., Wang, H., Shen, J., Wu, S., Zhang, J., Jia, N., Wessel, S., Abouatallah, R., Joos, N. and Schrooten, J. "Durability of PEM fuel cell cathode in the presence of Fe3+ and Al3+." *Journal of Power Sources* 195.24 (2010): 8089-8093.

63. Li, H., Tsay, K., Wang, H., Wu, S., Zhang, J., Jia, N., Wessel, S., Abouatallah, R., Joos, N. and Schrooten, J. "Effect of Co2+ on oxygen reduction reaction catalyzed by Pt catalyst, and its implications for fuel cell contamination." *Electrochimica Acta* 55.8 (2010): 2622-2628.

64. Pozio, A., Silva, R.F., De Francesco, M. and Giorgi, L. "Nafion degradation in PEFCs from end plate iron contamination." *Electrochimica acta* 48.11 (2003): 1543-1549.

65. Sulek, M., Adams, J., Kaberline, S., Ricketts, M. and Waldecker, J.R. "In situ metal ion contamination and the effects on proton exchange membrane fuel cell performance." *Journal of Power Sources* 196.21 (2011): 8967-8972.

66. Wang, Heli, and John A. Turner. "The influence of metal ions on the conductivity of Nafion 112 in polymer electrolyte membrane fuel cell." *Journal of Power Sources* 183.2 (2008): 576-580.

67. Hartnig, Christoph, and Thomas J. Schmidt. "On a new degradation mode for high-temperature polymer electrolyte fuel cells: how bipolar plate degradation affects cell performance." *Electrochimica acta* 56.11 (2011): 4237-4242.

68. Janßen, H., Edelmann, A., Mildebrath, T., Müller, P., Lehnert, W. and Stolten, D. "Design and experimental validation of an HT-PEFC stack with metallic BPP." *International Journal of Hydrogen Energy* 43.39 (2018): 18488-18497.

69. Chen, Chen-Yu, and Sheng-Chun Su. "Development and performance evaluation of a high temperature proton exchange membrane fuel cell with stamped 304 stainless steel bipolar plates." *International Journal of Hydrogen Energy* 43.29 (2018): 13430-13439.

70. Alegre, C., Álvarez-Manuel, L., Mustata, R., Valiño, L., Lozano, A. and Barreras, F. "Assessment of the durability of low-cost Al bipolar plates for High Temperature PEM fuel cells." *International Journal of Hydrogen Energy* 44.25 (2019): 12748-12759.

71. Brett, Daniel JL, and Nigel P. Brandon. "Review of materials and characterization methods for polymer electrolyte fuel cell flow-field plates." *Journal of Fuel Cell Science and Technology* 4.1 (2007): 29-44.

72. Janßen, H., Lüke, L., Lehnert, W. and Stolten, D. "Setup and experimental validation of a

5 kW HT-PEFC stack." *International Journal of Hydrogen Energy* 42.16 (2017): 11596-11604.

73. Lee, D., Lim, J.W., Nam, S. and Choi, I. "Gasket-integrated carbon/silicone elastomer composite bipolar plate for high-temperature PEMFC." *Composite Structures* 128 (2015): 284-290.

74. Lee, Dongyoung. "Carbon composite bipolar plate for high-temperature proton exchange membrane fuel cells (HT-PEMFCs)." *Journal of Power Sources* 327 (2016): 119-126.

75. Kuan, H.C., Ma, C.C.M., Chen, K.H. and Chen, S.M. "Preparation, electrical, mechanical and thermal properties of composite bipolar plate for a fuel cell." *Journal of Power Sources* 134.1 (2004): 7-17.

76. Huang, Jianhua, Donald G. Baird, and James E. McGrath. "Development of fuel cell bipolar plates from graphite filled wet-lay thermoplastic composite materials." *Journal of Power Sources* 150 (2005): 110-119.

77. Dhakate, S.R., Sharma, S., Borah, M., Mathur, R.B. and Dhami, T.L. "Expanded graphite-based electrically conductive composites as bipolar plate for PEM fuel cell." *International Journal of Hydrogen Energy* 33.23 (2008): 7146-7152.

78. Cho, E., Jeon, U.S., Ha, H.Y., Hong, S.A. and Oh, I.H. "Characteristics of composite bipolar plates for polymer electrolyte membrane fuel cells." *Journal of Power Sources* 125.2 (2004): 178-182.

79. Scholta, J., Rohland, B., Trapp, V. and Focken, U. "Investigations on novel low-cost graphite composite bipolar plates." *Journal of Power Sources* 84.2 (1999): 231-234.

80. Dhakate, S.R., Mathur, R.B., Kakati, B.K. and Dhami, T.L. "Properties of graphite-composite bipolar plate prepared by compression molding technique for PEM fuel cell." *International Journal of Hydrogen Energy* 32.17 (2007): 4537-4543.

81. Wind, J., Späh, R., Kaiser, W. and Böhm, G. "Metallic bipolar plates for PEM fuel cells." *Journal of Power Sources* 105.2 (2002): 256-260.

82. Tawfik, H., Y. Hung, and D. Mahajan. "Metal bipolar plates for PEM fuel cell—a review." *Journal of Power Sources* 163.2 (2007): 755-767.

83. Pozio, A., R. F. Silva, and A. Masci. "Corrosion study of SS430/Nb as bipolar plate materials for PEMFCs." *International Journal of Hydrogen Energy* 33.20 (2008): 5697-5702.

84. Choe, C., Choi, H., Hong, W. and Lee, J.J. "Tantalum nitride coated AISI 316L as bipolar plate for polymer electrolyte membrane fuel cell." *International Journal of Hydrogen*

Energy 37.1 (2012): 405-411.

85. Hentall, P.L., Lakeman, J.B., Mepsted, G.O., Adcock, P.L. and Moore, J.M. "New materials for polymer electrolyte membrane fuel cell current collectors." *Journal of Power Sources* 80.1-2 (1999): 235-241.

86. Jin, Chul Kyu, and Chung Gil Kang. "Fabrication process analysis and experimental verification for aluminum bipolar plates in fuel cells by vacuum die-casting." *Journal of Power Sources* 196.20 (2011): 8241-8249.

87. Hodgson, D.R., May, B., Adcock, P.L. and Davies, D.P. "New lightweight bipolar plate system for polymer electrolyte membrane fuel cells." *Journal of Power Sources* 96.1 (2001): 233-235.

88. Jin, Chul Kyu, and Chung Gil Kang. "Fabrication by vacuum die casting and simulation of aluminum bipolar plates with micro-channels on both sides for proton exchange membrane (PEM) fuel cells." *International Journal of Hydrogen Energy* 37.2 (2012): 1661-1676.

89. Wang, Szu-Hua, Jinchyau Peng, and Wai-Bun Lui. "Surface modification and development of titanium bipolar plates for PEM fuel cells." *Journal of Power Sources* 160.1 (2006): 485-489.

90. Wang, Heli, Mary Ann Sweikart, and John A. Turner. "Stainless steel as bipolar plate material for polymer electrolyte membrane fuel cells." *Journal of Power Sources* 115.2 (2003): 243-251.

91. Davies, D.P., Adcock, P.L., Turpin, M. and Rowen, S.J. "Stainless steel as a bipolar plate material for solid polymer fuel cells." *Journal of Power Sources* 86.1-2 (2000): 237-242.

92. Feng, K., Li, Z., Sun, H., Yu, L., Cai, X., Wu, Y. and Chu, P.K. "C/CrN multilayer coating for polymer electrolyte membrane fuel cell metallic bipolar plates." *Journal of Power Sources* 222 (2013): 351-358.

93. Zhang, M., Lin, G., Wu, B. and Shao, Z. "Composition optimization of arc ion plated CrNx films on 316L stainless steel as bipolar plates for polymer electrolyte membrane fuel cells." *Journal of Power Sources* 205 (2012): 318-323.

94. Zhang, H., Lin, G., Hou, M., Hu, L., Han, Z., Fu, Y., Shao, Z. and Yi, B. "CrN/Cr multilayer coating on 316L stainless steel as bipolar plates for proton exchange membrane fuel cells." *Journal of Power Sources* 198 (2012): 176-181.

95. Nam, Nguyen Dang, and Jung-Gu Kim. "Electrochemical behavior of CrN coated on 316L stainless steel in simulated cathodic environment of proton exchange membrane fuel cell." *Japanese Journal of Applied Physics* 47.8S2 (2008): 6887.

96. Zhang, D., Duan, L., Guo, L. and Tuan, W.H. "Corrosion behavior of TiN-coated stainless steel as bipolar plate for proton exchange membrane fuel cell." *International Journal of Hydrogen Energy* 35.8 (2010): 3721-3726.

97. Mori, Y., Ueda, M., Hashimoto, M., Aoi, Y., Tanase, S. and Sakai, T. "Amorphous carbon coated stainless separator for PEFCs." *Surface and Coatings Technology* 202.17 (2008): 4094-4101.

98. Lee, Y.H., Noh, S., Lee, J.H., Chun, S.H., Cha, S.W. and Chang, I. "Durable graphene-coated bipolar plates for polymer electrolyte fuel cells." *International Journal of Hydrogen Energy* 42.44 (2017): 27350-27353.

99. Fu, Y., Lin, G., Hou, M., Wu, B., Shao, Z. and Yi, B. "Carbon-based films coated 316L stainless steel as bipolar plate for proton exchange membrane fuel cells." *International Journal of Hydrogen Energy* 34.1 (2009): 405-409.

100. Garcia, MA Lucio, and Mascha A. Smit. "Study of electrodeposited polypyrrole coatings for the corrosion protection of stainless steel bipolar plates for the PEM fuel cell." *Journal of Power Sources* 158.1 (2006): 397-402.

101. Show, Yoshiyuki, Toshimitsu Nakashima, and Yuta Fukami. "Anticorrosion coating of carbon nanotube/polytetrafluoroethylene composite film on the stainless steel bipolar plate for proton exchange membrane fuel cells." *Journal of Nanomaterials* 2013.2514103 (2013): 2.

102. Jung, Ho-Young, Sheng-Yang Huang, and Branko N. Popov. "High-durability titanium bipolar plate modified by electrochemical deposition of platinum for unitized regenerative fuel cell (URFC)." *Journal of Power Sources* 195.7 (2010): 1950-1956.

103. Huang, N.B., Yu, H., Xu, L.S., Zhan, S., Sun, M. and Kirk, D.W. "Corrosion kinetics of 316L stainless steel bipolar plate with chromiumcarbide coating in simulated PEMFC cathodic environment." *Results in Physics* 6 (2016): 730-736.

104. Sun, Z. M. "Progress in research and development on MAX phases: a family of layered ternary compounds." *International Materials Reviews* 56.3 (2011): 143-166.

105. Radovic, Miladin, and Michel W. Barsoum. "MAX phases: bridging the gap between metals and ceramics." *American Ceramics Society Bulletin* 92.3 (2013): 20-27.

106. Barsoum, Michel W., and Tamer El-Raghy. "The MAX phases: Unique new carbide and nitride materials: Ternary ceramics turn out to be surprisingly soft and machinable, yet also heat-tolerant, strong and lightweight." *American Scientist* 89.4 (2001): 334-343.

107. Weissbecker, Vitali, et al. "Boron doped diamond coating on niobium as bipolar plate

material for HT-PEFCs." 20th World Hydrogen Energy Conference, Gwangju Metropolian City, Korea. Vol. 143. No. 3. 2014.

108. Kaserer, S., Rakousky, C., Melke, J. and Roth, C. "Design of a reference electrode for high-temperature PEM fuel cells." *Journal of Applied Electrochemistry* 43.11 (2013): 1069-1078.

109. Ekberg, Johanna "Characterization of corrosion at bipolar plates in HTPEM fuel cells." *Chalmers University of Technology, Sweden* (2013).

110. McCafferty, Edward. Introduction to corrosion science. Springer Science & Business Media, 2010.

111. Enos, D.G. and Scribner, L.L. The Potentiodynamic Polarization Scan, in Technical Report. 1997, Solartron Instruments.

112. Metrohm Matlab, Electrochemical impedance spectroscopy (EIS), in *Autolab Application Note*.

113. Liu, F., Mohajeri, S., Di, Y., Wippermann, K. and Lehnert, W. "Influence of the Interaction Between Phosphoric Acid and Catalyst Layers on the Properties of HT-PEFCs." *Fuel Cells* 14.5 (2014): 750-757.

114. Liu, F., Kvesić, M., Wippermann, K., Reimer, U. and Lehnert, W. "Effect of spiral flow field design on performance and durability of HT-PEFCs." *Journal of The Electrochemical Society* 160.8 (2013): F892-F897.

115. Rahim, Yasser, Holger Janßen, and Werner Lehnert. "Characterizing membrane electrode assemblies for high temperature polymer electrolyte membrane fuel cells using design of experiments." *International Journal of Hydrogen Energy* 42.2 (2017): 1189-1202.

116. balticFuelCells, user manual quick *CONNECTfixture qCf FC25/100.2009*.

117. balticFuelCells. Baltic Module. Available from: http://www.balticfuelcells.de/qcf.html.

118. Jespersen, Jesper Lebæk, Erik Schaltz, and Søren Knudsen Kær. "Electrochemical characterization of a polybenzimidazole-based high temperature proton exchange membrane unit cell." *Journal of Power Sources* 191.2 (2009): 289-296.

119. Wang, Heli, Mary Ann Sweikart, and John A. Turner. "Stainless steel as bipolar plate material for polymer electrolyte membrane fuel cells." *Journal of Power Sources* 115.2 (2003): 243-251.

120. Gan, F., and D-T. Chin. "Determination of diffusivity and solubility of oxygen in phosphoric acid using a transit time on a rotating ring-disc electrode." *Journal of Applied Electrochemistry* 23.5 (1993): 452-455.

121. Gubbins, Keith E., and Robert D. Walker. "The solubility and diffusivity of oxygen in

electrolytic solutions." *Journal of The Electrochemical Society* 112.5 (1965): 469-471.

122. Clayton, C. R., and Y. C. Lu. "A bipolar model of the passivity of stainless steel: the role of Mo addition." *Journal of the Electrochemical Society* 133.12 (1986): 2465-2473.

123. Macdonald, Digby D. "Passivity–the key to our metals-based civilization." *Pure and Applied Chemistry* 71.6 (1999): 951-978.

124. Lee, Shuo-Jen, and Jian-Jang Lai. "The effects of electropolishing (EP) process parameters on corrosion resistance of 316L stainless steel." *Journal of Materials Processing Technology* 140.1-3 (2003): 206-210.

125. Yang, Ying, Lie-jin Guo, and Hongtan Liu. "Corrosion characteristics of SS316L as bipolar plate material in PEMFC cathode environments with different acidities." *International Journal of Hydrogen Energy* 36.2 (2011): 1654-1663.

126. Lee, S.H., Yang, T.H., Hyun, S.H. and Yoon, Y.S. "Corrosion behavior of pre-oxidized and thermally nitrided stainless steel for polymer electrolyte membrane fuel cell bipolar plates." *Corrosion Science* 58 (2012): 79-85.

127. Pu, N.W., Shi, G.N., Liu, Y.M., Sun, X., Chang, J.K., Sun, C.L., Ger, M.D., Chen, C.Y., Wang, P.C., Peng, Y.Y. and Wu, C.H. "Graphene grown on stainless steel as a high-performance and ecofriendly anti-corrosion coating for polymer electrolyte membrane fuel cell bipolar plates." *Journal of Power Sources* 282 (2015): 248-256.

128. Zhang, M., Lin, G., Wu, B. and Shao, Z. "Composition optimization of arc ion plated CrNx films on 316L stainless steel as bipolar plates for polymer electrolyte membrane fuel cells." *Journal of Power Sources* 205 (2012): 318-323.

129. Wang, Heli, and John A. Turner. "Ferritic stainless steels as bipolar plate material for polymer electrolyte membrane fuel cells." *Journal of Power Sources* 128.2 (2004): 193-200.

130. Wang, Heli, and John A. Turner. "Austenitic stainless steels in high temperature phosphoric acid." *Journal of Power Sources* 180.2 (2008): 803-807.

131. Wang, Heli, Glen Teeter, and John Turner. "Investigation of a duplex stainless steel as polymer electrolyte membrane fuel cell bipolar plate material." *Journal of the Electrochemical Society* 152.3 (2005): B99-B104.

132. Li, R., Cai, Y., Wippermann, K. and Lehnert, W. "Bilayer CrN/Cr coating-modified 316L stainless steel bipolar plates for high temperature polymer electrolyte fuel cells." *Journal of Power Sources* 434 (2019): 226718.

133. Feng, K., Cai, X., Sun, H., Li, Z. and Chu, P.K. "Carbon coated stainless steel bipolar

plates in polymer electrolyte membrane fuel cells." *Diamond and Related Materials* 19.11 (2010): 1354-1361.

134. Li, R., Cai, Y., Wippermann, K. and Lehnert, W. "Corrosion and Electrical Properties of SS316L Materials in the Simulated HT-PEFC Environment." *Journal of The Electrochemical Society* 165.10 (2018): C681-C688.

135. Liu, C., Q. Bi, and A. Matthews. "Tribological and electrochemical performance of PVD TiN coatings on the femoral head of Ti–6Al–4V artificial hip joints." *Surface and coatings Technology* 163 (2003): 597-604.

136. Mani, S. Pugal, A. Srinivasan, and N. Rajendran. "Effect of nitrides on the corrosion behaviour of 316L SS bipolar plates for Proton Exchange Membrane Fuel Cell (PEMFC)." *International Journal of Hydrogen Energy* 40.8 (2015): 3359-3369.

137. Lee, S.H., Kakati, N., Maiti, J., Jee, S.H., Kalita, D.J. and Yoon, Y.S. "Corrosion and electrical properties of CrN-and TiN-coated 316L stainless steel used as bipolar plates for polymer electrolyte membrane fuel cells." *Thin Solid Films* 529 (2013): 374-379.

138. Meng, W. J., and T. J. Curtis. "Inductively coupled plasma assisted physical vapor deposition of titanium nitride coatings." *Journal of Electronic Materials* 26.11 (1997): 1297-1302.

139. Li, R., Cai, Y., Wippermann, K. and Lehnert, W. "The Electrochemical Behavior of CrN/Cr Coatings with Defects on 316L Stainless Steel in the Simulated Cathodic Environment of an HT-PEFC." *Journal of The Electrochemical Society* 166.13 (2019): C394-C400.

140. Wang, L., Kang, B., Gao, N., Du, X., Jia, L. and Sun, J. "Corrosion behaviour of austenitic stainless steel as a function of methanol concentration for direct methanol fuel cell bipolar plate." *Journal of Power Sources* 253 (2014): 332-341.

141. Li, R., Cai, Y., Reimer, U., Wippermann, K. and Lehnert, W. "CrN/Cr-coated Steel Plates for High-Temperature Polymer Electrolyte Fuel Cells – Performance and Durability." (2019): has been submitted for publication.

142. Lin, Yu. *Characterization of Phosphoric Acid Doped Polybenzimidazole Membranes*. Diss. Universitätsbibliothek der RWTH Aachen, 2018.

143. Lin, R., Li, B., Hou, Y.P. and Ma, J.M. "Investigation of dynamic driving cycle effect on performance degradation and micro-structure change of PEM fuel cell." *International Journal of Hydrogen Energy* 34.5 (2009): 2369-2376.

144. Zhang, S., Yuan, X.Z., Hin, J.N.C., Wang, H., Wu, J., Friedrich, K.A. and Schulze, M. "Effects of open-circuit operation on membrane and catalyst layer degradation in proton

exchange membrane fuel cells." *Journal of Power Sources* 195.4 (2010): 1142-1148.

145. Liu, S., Rasinski, M., Lin, Y., Wippermann, K., Everwand, A. and Lehnert, W. "Effects of constant load operations on platinum bands formation and cathode degradation in high-temperature polymer electrolyte fuel cells." *Electrochimica Acta* 289 (2018): 354-362.
146. Winther-Jensen, Bjorn, and Douglas R. MacFarlane. "New generation, metal-free electrocatalysts for fuel cells, solar cells and water splitting." *Energy & Environmental Science* 4.8 (2011): 2790-2798.
147. Marcinkoski, J., James, B.D., Kalinoski, J.A., Podolski, W., Benjamin, T. and Kopasz, J. "Manufacturing process assumptions used in fuel cell system cost analyses." *Journal of Power Sources* 196.12 (2011): 5282-5292.
148. Langemann, M., Fritz, D.L., Müller, M. and Stolten, D. "Validation and characterization of suitable materials for bipolar plates in PEM water electrolysis." *International Journal of Hydrogen Energy* 40.35 (2015): 11385-11391.
149. Bar-On, Isa, Randy Kirchain, and Richard Roth. "Technical cost analysis for PEM fuel cells." *Journal of Power Sources* 109.1 (2002): 71-75.
150. Janßen, H., Supra, J., Lüke, L., Lehnert, W. and Stolten, D. "Development of HT-PEFC stacks in the kW range." *International Journal of Hydrogen Energy* 38.11 (2013): 4705-4713.
151. Daure, J.L., Voisey, K.T., Shipway, P.H. and Stewart, D.A. "The effect of coating architecture and defects on the corrosion behaviour of a PVD multilayer Inconel 625/Cr coating." *Surface and Coatings Technology* 324 (2017): 403-412.
152. Zhong, C., X. Tang, and Y. F. Cheng. "Corrosion of steel under the defected coating studied by localized electrochemical impedance spectroscopy." *Electrochimica Acta* 53.14 (2008): 4740-4747.
153. Wang, H.W., Stack, M.M., Lyon, S.B., Hovsepian, P. and Münz, W.D. "The corrosion behaviour of macroparticle defects in arc bond-sputtered CrN/NbN superlattice coatings." *Surface and Coatings Technology* 126.2-3 (2000): 279-287.

List of Figures

List of Tables

Acknowledgements

After four years of study in Germany, my Ph.D. student time is about to come to a close. When I look back, I can think of many people to whom I would like to express my gratitude for their help, support and assistance in the preparation of my dissertation.

First and foremost, I would like to thank my supervisor, Prof. Werner Lehnert, for extending to me the opportunity to study and work in Forschungszentrum Juelich and RWTH-Aachen. He has given me much guidance on my Ph.D. research subject. Without his constant encouragement and guidance over these years, this thesis could never have reached its present stage. Also, I would like to express my heartfelt gratitude to Dr. Michael Rohwerder at MPIE, for accepting me into his group as a visiting Ph.D. student in the last year of my Ph.D. period. His guidance and help give me a deeper understanding of the corrosion process. Additionally, I am grateful to the China Scholarship Council (CSC) for their financial support for my Ph.D. study in Germany. My sincere thanks also to Prof. Lorenz Singheiser and Prof. Michael Lauster for evaluating my Ph.D. work.

I wish also to say thanks to my colleagues at IEK-3 and MPIE. Special thanks to Dr. Klaus Wippermann, for all your help, guidance and patience. Without your help and guidance, everything would have been much more challenging. Thanks to Dr. Uwe Reimer for our productive discussions. In addition, this work was experimentally helped by Andreas Everwand, Dr. Volker Nischwitz, Dr. Heinrich Hartmann.

Finally, I appreciate my wife, Yun Cai, for her help, encouragement and cooperation in both my work and life. Without her support, I would not have completed this dissertation in such a timely manner. Also, my deepest appreciation to my family: all my thanks for your consistent support, help and encouragement. This work is dedicated to you.

Band / Volume 458
Synthesis and Analysis of Spinel Cathode Materials for High Voltage Solid-State Lithium Batteries
A. Windmüller (2019), iv, 142 pp
ISBN: 978-3-95806-396-9

Band / Volume 459
Monazite-type ceramics as nuclear waste form: Crystal structure, microstructure and properties
Y. Arinicheva (2019), 194 pp
ISBN: 978-3-95806-397-6

Band / Volume 460
Coupling a Solid Oxide Fuel Cell with a Biomass Gasifier: Degradation Mechanisms and Alternative Anode Materials
H. Jeong (2019), II, 112 pp
ISBN: 978-3-95806-398-3

Band / Volume 461
Model-based Source Partitioning of Eddy Covariance Flux Measurements
A. Klosterhalfen (2019), XVI, 132 pp
ISBN: 978-3-95806-401-0

Band / Volume 462
Entwicklung von großflächigen PECVD-Prozessen zur kontrollierten, homogenen Abscheidung dünner Siliziumschichten für die Photovoltaik
B. O. Grootoonk (2019), 154 pp
ISBN: 978-3-95806-402-7

Band / Volume 463
Simulation of Transport Processes through an Asymmetric Gas Separation Membrane
U. V. Unije (2019), xiv, 101 pp
ISBN: 978-3-95806-403-4

Band / Volume 464
Development, calibration and deployment of an airborne chemical ionization mass spectrometer for trace gas measurements
T. Khattatov (2019), 14, 125 pp
ISBN: 978-3-95806-404-1

Band / Volume 465
IEK-3 Report 2019
Maßgeschneiderte Energieumwandlung für nachhaltige Kraftstoffe
D. Stolten, B. Emonts (Eds.) (2019), 171 pp
ISBN: 978-3-95806-410-2

Schriften des Forschungszentrums Jülich
Reihe Energie & Umwelt / Energy & Environment

Band / Volume 466
Initialinfrastruktur für Wasserstoffmobilität auf Basis von Flotten
F. Grüger (2019), V, 209 pp
ISBN: 978-3-95806-413-3

Band / Volume 467
Techno-ökonomische Analyse alternativer Wasserstoffinfrastruktur
M. E. Reuß (2019), 205 pp
ISBN: 978-3-95806-414-0

Band / Volume 468
Study on a miniaturized satellite payload for atmospheric temperature measurements
J. Liu (2019), 153 pp
ISBN: 978-3-95806-415-7

Band / Volume 469
Partitioning Water Vapor Fluxes by the Use of Their Water Stable Isotopologues: From the Lab to the Field
M. E. Quade (2019), XVI, 113 pp
ISBN: 978-3-95806-417-1

Band / Volume 470
Entwicklung von Reparaturmethoden für Nickel-Superlegierungen mittels thermischer Spritzverfahren
T. Kalfhaus (2019), VI, 126, XXX pp
ISBN: 978-3-95806-418-8

Band / Volume 471
Entwicklung von korrosionsstabilen Schutzschichten für oxidische Faserverbundwerkstoffe
C. S. Gatzen (2019), II, 143 pp
ISBN: 978-3-95806-422-5

Band / Volume 472
Coatings for Metallic Bipolar Plates in High-Temperature Polymer Electrolyte Fuel Cells
R. Li (2019), II, 119 pp
ISBN: 978-3-95806-425-6

Weitere ***Schriften des Verlags im Forschungszentrum Jülich*** unter
http://wwwzb1.fz-juelich.de/verlagextern1/index.asp

Energie & Umwelt / Energy & Environment
Band / Volume 472
ISBN 978-3-95806-425-6

Mitglied der Helmholtz-Gemeinschaft

JÜLICH
Forschungszentrum